Title
MOLECULAR BEAM PHOTOIONIZATION AND GAS-SURFACE SCATTERING

Author
Ceyer, S.T.

Publication Date
1979-09-01

LBL-9838

Lawrence Berkeley Laboratory
UNIVERSITY OF CALIFORNIA

Materials & Molecular
Research Division

MOLECULAR BEAM PHOTOIONIZATION AND GAS-SURFACE SCATTERING

Sylvia Teresse Ceyer
(Ph. D. thesis)

September 1979

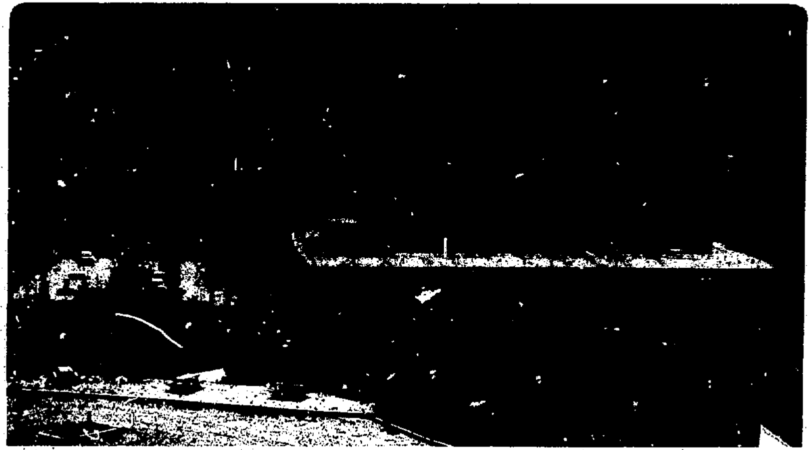

Prepared for the U.S. Department of Energy under Contract W-7405-ENG-48

LBL-9838

MOLECULAR BEAM PHOTOIONIZATION AND GAS-SURFACE SCATTERING

Sylvia Teresse Ceyer

Materials and Molecular Research Division
Lawrence Berkeley Laboratory

and

Department of Chemistry
University of California
Berkeley, California 94720

September, 1979

ABSTRACT

The energetics of the ethylene ion-molecule reactions have been investigated in more detail than previously possible in two body collision experiments by photoionization of the neutral van der Waals ethylene dimer, as described in Chapter I. The stability of the $(C_2H_4)^+C_2H_4$ ion-molecule collision complex has been determined to be 18.2 ± 0.5 kcal. The highest potential barriers along the reaction coordinate for decomposition of this collision complex into $C_4H_7^+ + H$ and $C_3H_5^+ + CH_3$ have been determined to be 0 ± 1.5 and 8.7 ± 1.5 kcal. In a similar manner, the energetics of the solvated ethylene dimer ion has been investigated by the photoionization of the ethylene trimer.

The absolute proton affinity of NH_3 (203.6 ± 1.3 kcal/mole) and the proton solvation energies by more than one NH_3 have been determined by molecular beam photoionization, as described in Chapter II. In addition, the NH_3^+-NH_3 interaction energy (0.79 ± 0.05 eV) has

been measured by photoionization of the neutral van der Waals dimer. These experiments have shown that photoionization of van der Waals clusters is a very powerful method of determining the energetics of gas phase proton solvation.

Chapter III explores the scattering of helium atomic beams from a high Miller index platinum surface that exhibits ordered, periodic steps on the atomic scale to probe the effect of atomic steps on the scattering distribution. Rainbow scattering is observed when the step edges are perpendicular to the incident helium atoms. Rainbow peaks result from an accumulation of trajectories at two angles that correspond to the maximum and minimum scattering angles introduced by the periodic surface potential. A rainbow scattering distribution can yield information about the repulsive shape of the surface potential.

Chapter IV describes the design, construction and operation of a beam-surface scattering apparatus. The purpose of the apparatus is to study the dynamics of a gas-surface reaction by observing the product angular and velocity distribution. Chapter V presents the first data obtained in this apparatus and discusses the interesting dynamical aspects of the oxidation of D, D_2 and CO.

MOLECULAR BEAM PHOTOIONIZATION AND GAS-SURFACE SCATTERING

Table of Contents

ACKNOWLEDGEMENTS

It is a very stimulating and fruitful experience to be associated wtih two enthusiastic research groups. For this opportunity, I sincerely thank Professor G. A. Somorjai and Professor Y. T. Lee.

Professor G. A. Somorjai unfailingly presented me with the challenges of the material in Chapters III-V. It is from this challenge that I learned and because I learned, I am grateful. He allowed me the chance last year, to help the apparatus described in Chapter IV mature. For this chance, I am also deeply grateful.

The apparatus described in Chapter IV required much valuable assistance from the support staff of Materials and Molecular Research Division. Bob McAllister and Emery Kozak deserve recognition for their efforts in machining numerous parts. My special thanks go to Weyland Wong for very excellent machining and design advice that was always delivered kindly and objectively. I thank Glenn Baum for his cheerful patience with my overbearing use of his leak detector. I appreciate the fine efforts of Del Peterson in electronics installation during the early stages of the apparatus development. Jim Severns would always come through in an emergency.

My sincere gratitude goes to Ms. Ann Weightman for cheerfully typing this manuscript.

I would like to thank all the members of both groups over the past five years for their enthusiastic discussions, valuable advice, moral support and sincere friendship but especially Rick Buss,

John and Carol Smith Hemminger, Peter Schulz, Bull Guthrie, Fred Wagner, Randy Sparks, Dr. Dave Hagen, Dr. Jean Paul Biberian, Bill Gillespie, Dr. Dan Dwyer, Yip Wah Chung, Matt Vernon, Dr. Mike Coggiola, Dr. Salvador Ferrer, Mark Davis and Dr. Miguel Salmeron.

Steven Bernasek and Becky Gale were very efficient in introducing me to the experimental nuts and bolts of surface science in the work presented in Chapter III. The fine initial coaching by Dr. Cheuk Ng in the work presented in Chapters I and II and the very enjoyable and productive collaboration with Dr. Peter Tiedemann is gratefully acknowledged. I wish to thank Jon Sokol and Don Danielson for their assistance on the development of the apparatus described in Chapter IV.

The factual and analytical knowledge that I gained from working with Dr. Wigbert Siekhaus is invaluable. He enthusiastically discussed the machine design with me, looking carefully at my first crude drawings, slashing across my lines, making suggestions and asking questions. Much of this he did on his own time because he believed that man has a strong desire to succeed in understanding the world around him.

I wish to sincerely thank Professor Yuan Lee not only for his sound scientific suggestions but more importantly for his continuous confidence in me which, I think at least on one occasion, was the singular ingredient to the successful conclusion of this work. He always managed to point out why I should smile when I was convinced I had no reason to smile.

Finally, I wish to thank my parents and sister and brother who always listen and always support my endeavors.

This work was supported by the Division of Chemical Sciences, Office of Basic Energy Sciences, U. S. Department of Energy under contract No. W-7405-Eng-48 and the Office of Naval Research.

PART I. THERMOCHEMICAL QUANTITIES BY MOLECULAR BEAM PHOTOIONIZATION

I. PHOTOIONIZATION OF ETHYLENE CLUSTERS

A. Introduction

The ethylene ion-molecule reaction has been the subject of many investigations. Previous experiments have generally concentrated on measuring the relative rate constants of the ethylene ion-molecule reactions and of the secondary reactions as a function of gas pressure in radiolysis,[1,2] photolysis[3] and high pressure mass spectrometric investigations[4-9] and as a function of translational and internal energy in ion cyclotron resonance[10-14] and gas cell photoionization experiments.[15] The reactions most commonly studied are shown in (1) - (8):

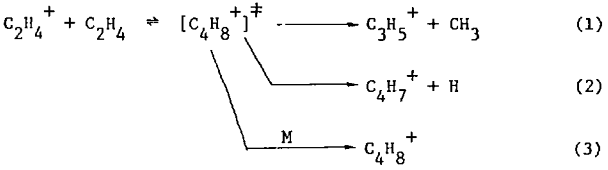

$$C_2H_4^+ + C_2H_4 \rightleftharpoons [C_4H_8^+]^\ddagger \longrightarrow C_3H_5^+ + CH_3 \quad (1)$$

$$\longrightarrow C_4H_7^+ + H \quad (2)$$

$$\xrightarrow{M} C_4H_8^+ \quad (3)$$

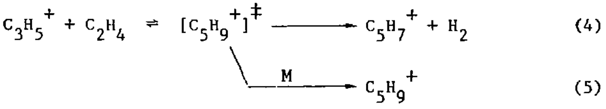

$$C_3H_5^+ + C_2H_4 \rightleftharpoons [C_5H_9^+]^\ddagger \longrightarrow C_5H_7^+ + H_2 \quad (4)$$

$$\xrightarrow{M} C_5H_9^+ \quad (5)$$

$$\begin{aligned} C_4H_8^+ + C_2H_4 \rightleftharpoons [C_6H_{12}^+]^{\ddagger} &\longrightarrow C_5H_9^+ + CH_3 && (6)\\ &\longrightarrow C_6H_{11}^+ + H && (7)\\ &\xrightarrow{M} C_6H_{12}^+ && (8) \end{aligned}$$

The common conclusion from these studies is that the primary reaction proceeds through some long-lived intermediate which can be collisionally stabilized to yield a butene structure.[2] If stabilization does not occur, the intermediate may decompose to form the initial reactants or the products shown in (1) and (2). Further experiments performed on reactions between ethylene ion and deuterated ethylene yield a statistical isotope distribution of the products consistent with the concept of the formation of a long-lived complex.[7] This conclusion is also supported by a crossed beam experiment whose angular distribution indicates that an intermediate is formed which is long-lived compared to the rotational period of the complex.[16]

However, these experiments yield no information regarding the details of the energetics along the reaction coordinate. For instance, it is possible that a loosely bound collision complex $C_2H_4^+ \cdot C_2H_4$ is a precursor to the intermediate provided that there is a potential barrier to the formation of the $(C_4H_8^+)^{\ddagger}$ species. The stability of this collision complex cannot be determined in the two body exothermic reaction due to the large total energy of the system compared to the stability of the precursor. In addition, the large total energy prevents the determination of the potential barriers along the reaction coordinate. Knowledge of these barriers is essential to the understanding of the energy distribution of the long-lived complex as determined in the crossed beam experiment.

In this investigation, the stabilized collision complex has been formed as the initial reactant by photoionization of the ethylene dimer and trimer species produced by adiabatic expansion in a beam. The stability of the ion cluster formed is determined from the threshold energy of formation, since the photoionization of the van der Waals polymer is viewed as ionization of only one of the species. Further excitation of the ion cluster allows the vibrational energy-induced ion-molecule reaction at zero kinetic energy to proceed. With the fine control of the ionizing energy attainable by photoionization techniques, the vibrational degrees of freedom of the complex are excited successively so that the highest potential energy barrier to decomposition along the reaction coordinate is determined.

B. Experimental

Since the experimental apparatus employed in this study has been described previously,[17,18] only the details essential to this investigation will be related here. Schematic diagrams of the apparatus are shown in Figures 1 and 2.

The hydrogen many-line pseudocontinuum was used as a source of ionizing radiation. The DC discharge was powered by a 5 kV, 4 amp supply (LBL - 17 x 4544 - W1). The current was stabilized by a parallel

Fig. 1. Schematic diagram of the apparatus. (1) McPherson 225 Vacuum UV Monochromator. (2) Differential Pumping System. (3) Entrance Slit. (4) Light Source. (5) Exit Slit. (6) Sodium Salicylate Coated Quartz Window. (7) Photomultiplier. (8) Nozzle. (9) Tuning Fork Chopper.

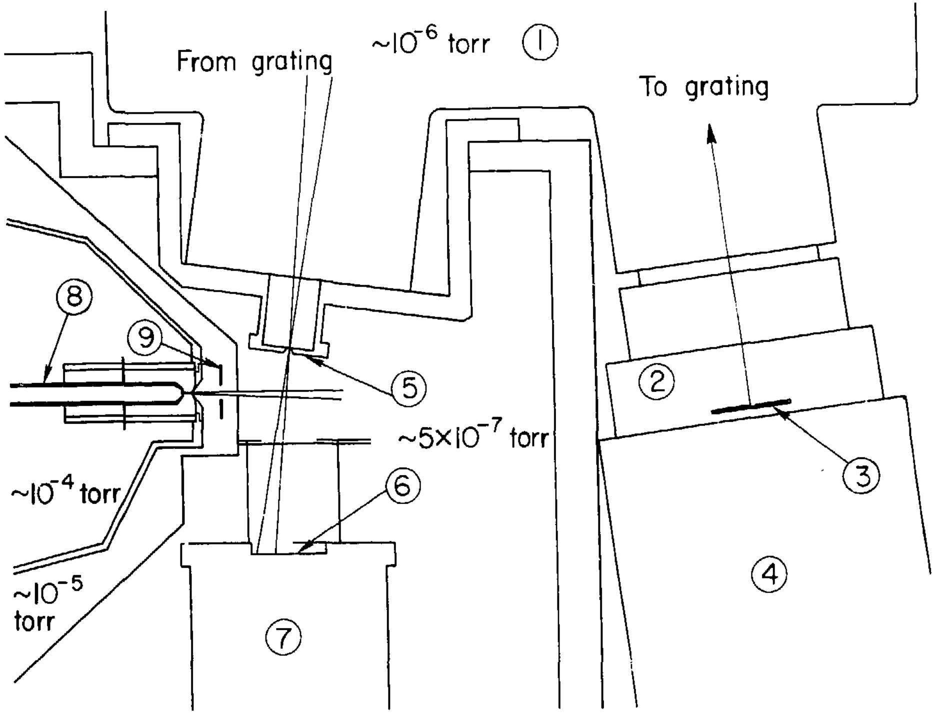

Fig. 1

XBL 764-2667

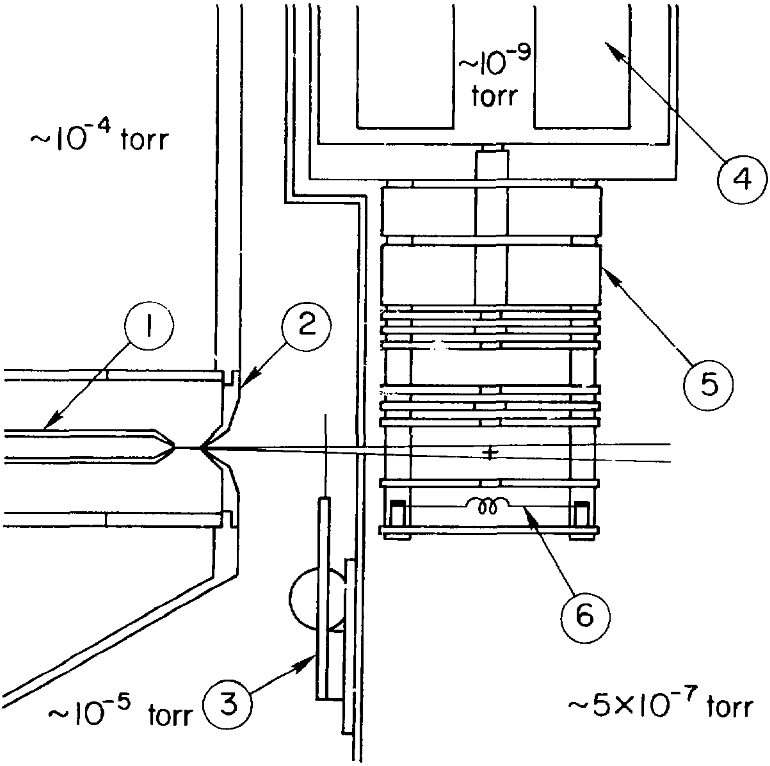

XBL 764-2666

Fig. 2. Schematic diagram of the apparatus - cross section through beam line of Figure 1. (1) Nozzle. (2) Skimmer. (3) Tuning Fork Chopper. (4) Quadrupole Mass Spectrometer. (5) Ion Focusing Lenses. (6) Electron Gun.

arrangement of seven, 10 kΩ, 200 watt resistors connected in series with the lamp. For a 11 inch long quartz capillary with a 3-5 torr steady flow of H_2,[17] the typical operating conditions were 1500 V at 0.75 amps. With these values the resistance of the lamp is calculated as 572Ω. The amount of power that can be delivered to the lamp by the supply and the current stability of the supply are presently limited by the characteristics of the resistors in series with the supply output. Thus, with this arrangement, attempts to stabilize a discharge produced in a 22 inch long capillary were not successful.

The light was dispersed by an MgF_2 coated grating of 1200 lines/mm with an 0.83 nm/mm reciprocal dispersion. With 300 μm entrance and exit slits a 0.25 nm photon bandwidth is achieved. The light intensity from a freshly coated grating at Lyman α (1215.7 Å) was typically 2.5×10^{-5} amps or $5 \times 10^{8}\ \frac{\text{photons}}{\text{sec Å}}$. This value assumes a freshly coated sodium salicylate scintillator with an absolute quantum efficiency of 0.65[19] and an EMI photomultiplier 9436 GR at ~750 V with a gain of 2×10^{5}.

The ethylene polymers were produced by supersonic expansion of a mixture of ethylene and argon through a 0.003" diameter nozzle. A 13% mixture of C_2H_4 in Ar was determined to yield the largest ratio of dimer to monomer representing a 30% increase in the dimer to monomer ratio over the maximum ratio of a neat C_2H_4 beam. Below 13%, the dimer concentration decreased rapidly. The mixture was not optimized for trimer concentration. A typical product distribution of the beam after photoionization with the monochromator adjusted to zero order is shown in Fig. 3.

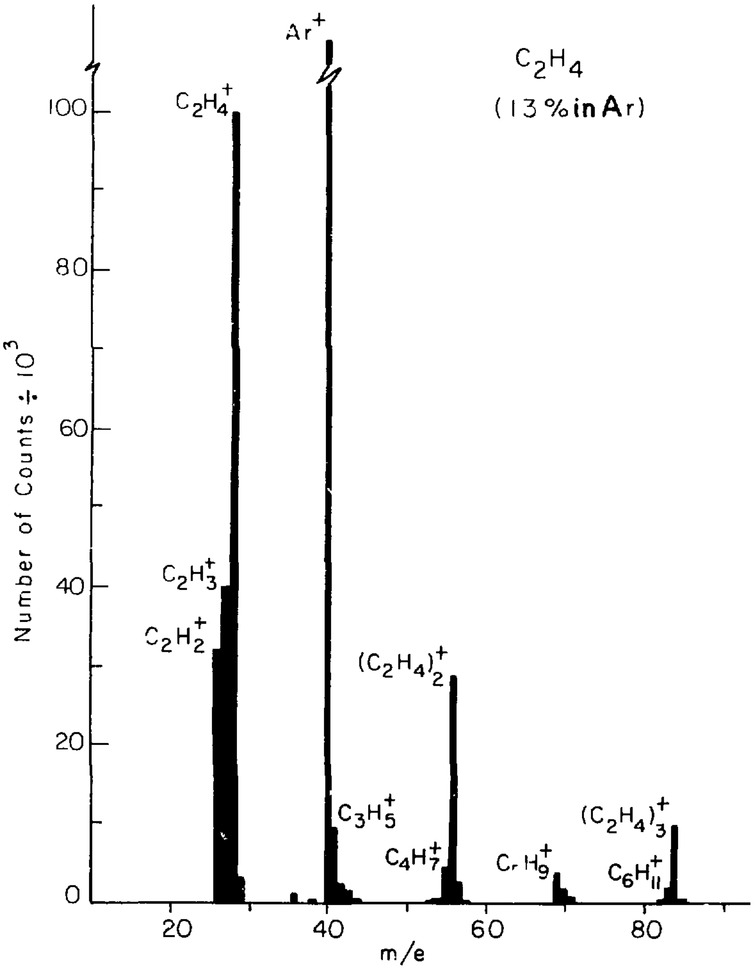

XBL 786-5237

Fig. 3. Production distribution of the beam after photoionization with the monochromator adjusted to zero order. The stagnation pressure is 800 torr.

The ratio of polymers and fragments to Ar was also investigated as a function of stagnation pressure with a 13% C_2H_4 in Ar mixture at zero order. The results are shown in Fig. 4. The pressure dependence study serves to discover the condition of maximum intensity of the particular ion of interest and to clarify the nature of the parent clusters $(C_2H_4)_n$.

The number of mass selected ions produced and the number of photons intersecting the beam was monitored at 0.1 nm intervals. The amount of background scattered light was measured at 85.0 nm where there is no emission from the H_2 discharge.[19] This value was assumed to be constant over the wavelength region employed and subtracted from the light intensity before the photoionization efficiencies were calculated. For a few of the scans, the background scattered light was as much as 25% of the incident radiation reaching the scintillator depending on the wavelength and the condition of the grating. For a freshly coated grating the amount of scattered light could easily be below 0.1% of the incident radiation. Also, the photoionization efficiency at about 116.0 nm was arbitrarily chosen (there is a peak in intensity at approximately this wavelength) as a reference point with which to monitor the fluctuation in the beam and in the light intensity. The reference point was recorded approximately every 90 minutes. Thus, the photoionization efficiency curves are time normalized. This procedure is extremely important since the light intensity has been sometimes observed to decrease linearly by 50% in four hours due to degradation of the grating.

Fig. 4. Intensity of dimers, trimers and fragments after photoionization with the monochromator adjusted to zero order versus pressure of 13% C_2H_4 in Ar behind the nozzle.

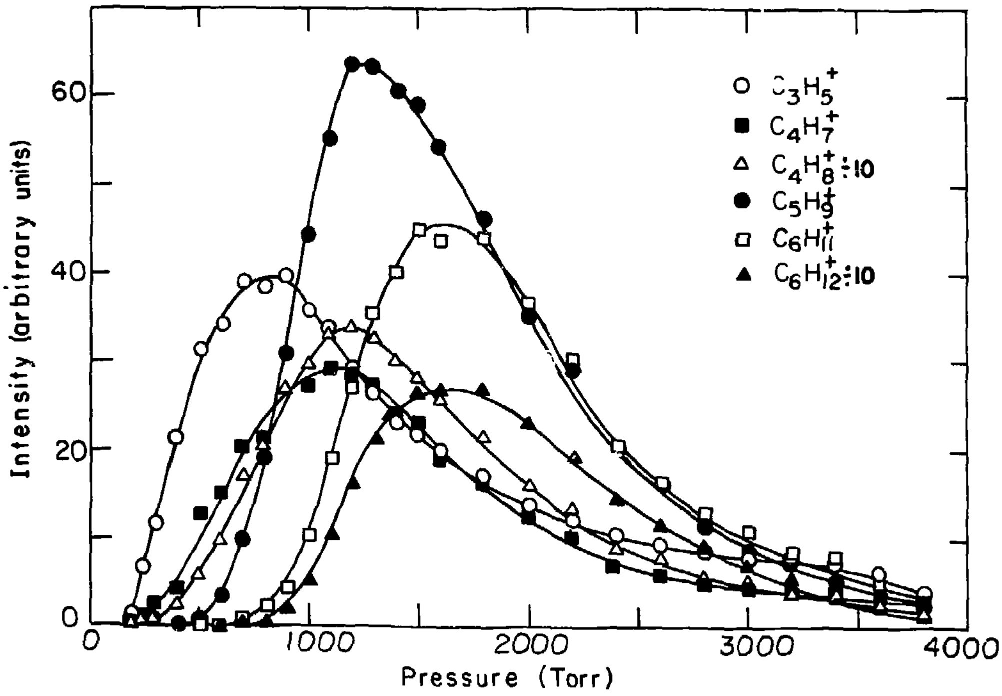
Intensity (arbitrary units)
0
20
40
60
Pressure (Torr)
0
1000
2000
3000
4000
○ $C_3H_5^+$
■ $C_4H_7^+$
△ $C_4H_8^+ \div 10$
● $C_5H_9^+$
□ $C_6H_{11}^+$
▲ $C_6H_{12}^+ \div 10$
XBL 7712-10925

Fig. 4

C. Results

The photoionization efficiency curves for the $(C_2H_4)_2^+$, $C_4H_7^+$ and $C_3H_5^+$ ions are shown in Fig. 5. The standard deviations are on the order of 10% at the thresholds of the curves and about 2% at 2.0 nm beyond the threshold values. The photoionization efficiencies for the corresponding trimer system are shown in Fig. 6. The standard deviations of the trimer fragment intensities are about 15% at the thresholds. All curves are an average of 2-3 scans. Points were measured at much lower energies than the threshold values so that an average background ion intensity was obtained. The threshold values are labeled as such when the photoionization efficiency values increase monotonically. The threshold uncertainties were taken to encompass the thresholds obtained in two or three separate scans.

D. Discussion

The photoionization of the ethylene dimer at the threshold can be considered as removal of an electron from the $1b_{3u}$ orbital which is associated with the π bond between two carbon atoms of one of the ethylene molecules. This is evidenced by the vibrational structure present near the dimer ion threshold. The observed vibrational structure is similar to the fine structure of the Rydberg series converging to the ground state of the ion seen in vacuum ultraviolet absorption experiments.[20,21] The totally symmetric C-C valence stretching vibration ν_2 and a twisting vibration ν_4 of C_2H_4 have been observed

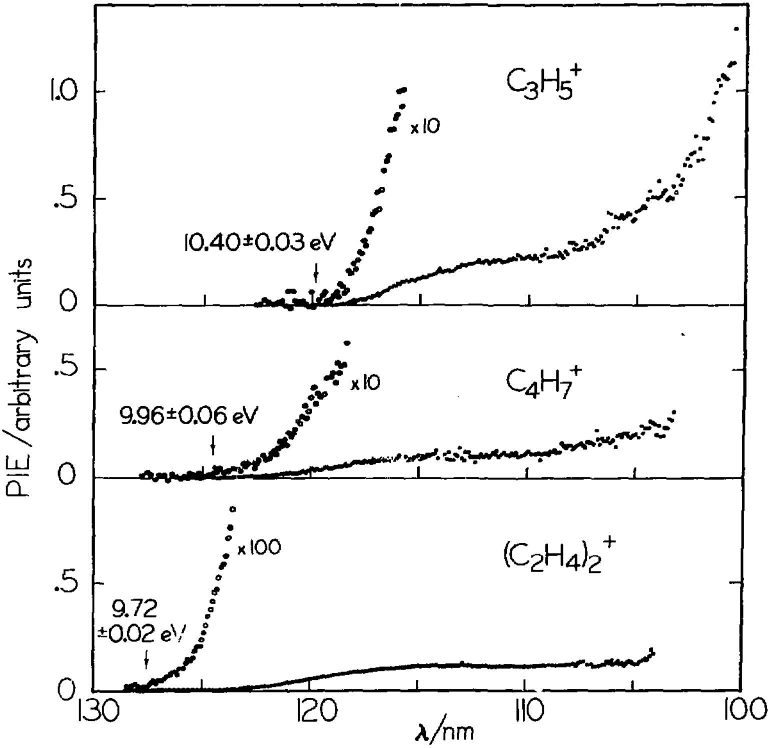

XBL 779-4878

Fig. 5. Photionization efficiency of $(C_2H_4)_2^+$, $C_3H_5^+$, and $C_4H_7^+$ normalized at 116.0 nm.

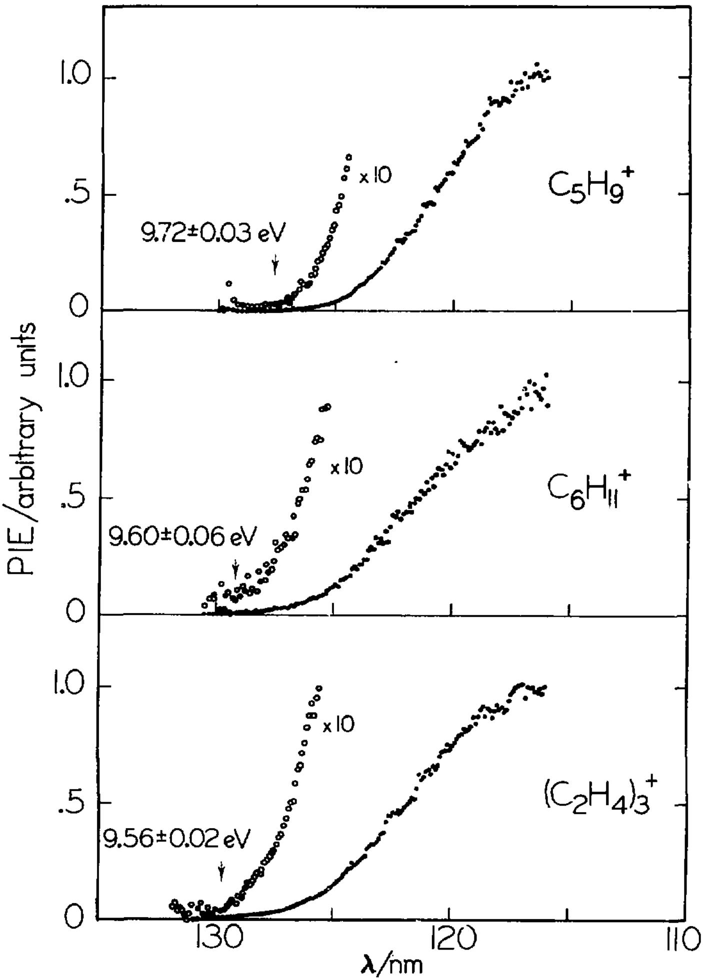

XBL 779-4879

Fig. 6. Photoionization efficiency of $(C_2H_4)_3^+$, $C_5H_9^+$ and $C_6H_{11}^+$ normalized at 116.0 nm.

previously in photoelectron (ν_2 = 1230 cm^{-1}, 2ν_4 = 430 cm^{-1})[22] and photoionization experiments (ν_2 = 1400 cm^{-1}, 2ν_4 = 440 cm^{-1})[23] (ν_2 = 1250 ± 40 cm^{-1}, 2ν_4 = 400 cm^{-1}).[24] The most obvious structure in the dimer ion curve in Fig. 7 is the excitation of one quantum of the ν_2 mode. It is more clearly seen in a log-log plot of the threshold region (Fig. 8) where a change in the initial slope occurs at 125.6 ± 0.3 nm when the available amount of phase space suddenly increases. The uncertainty is due primarily to the scatter in the data near the threshold. This breakpoint yields a vibrational frequency of 0.15 ± 0.02 eV or 1186 ± 200 cm^{-1} for ν_2. Further excitation of this mode and excitation of the ν_4 mode are less discernible.

Similar log-log plots of the threshold region for $C_4H_7^+$ and $C_3H_5^+$ fragments are shown in Figs. 9 and 10. The break in the log-log plot of $C_4H_7^+$ suggests a value of 0.21 ± 0.03 eV or 1725 ± 242 cm^{-1} for the corresponding ν_2 mode as observed in photoelectron data of C_2H_4. There is no evidence of this mode in the $C_3H_5^+$ threshold region as expected. It is apparent from the difference between the dimer ion and $C_3H_5^+$ threshold that four or five quanta of the ν_2 C-C stretching vibration are required to eliminate a CH_3 group from the dimer ion.

The photoionization efficiency curves for both the dimer and trimer system are relatively featureless above the threshold region. No autoionization of the Rydberg states that are coverging to the first excited state of the ethylene ion at 12.38 eV is apparent.[21] The first excited state of the $C_3H_5^+$ ion occurs at 11.6 ± 0.08 eV (106.5 nm) as is seen from these data.

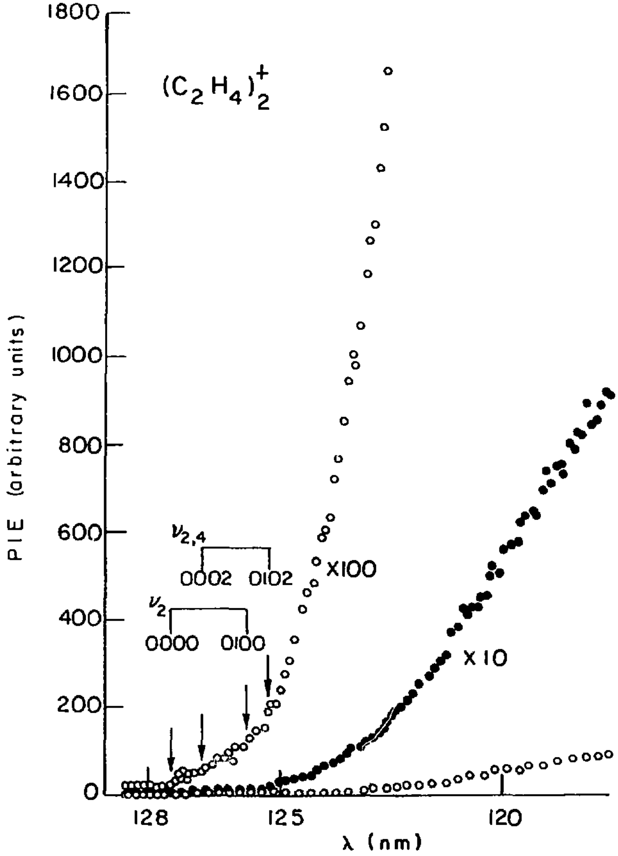

XBL786-5238

Fig. 7. Threshold region of photoionization efficency cruve of $(C_2H_4)_2^+$.

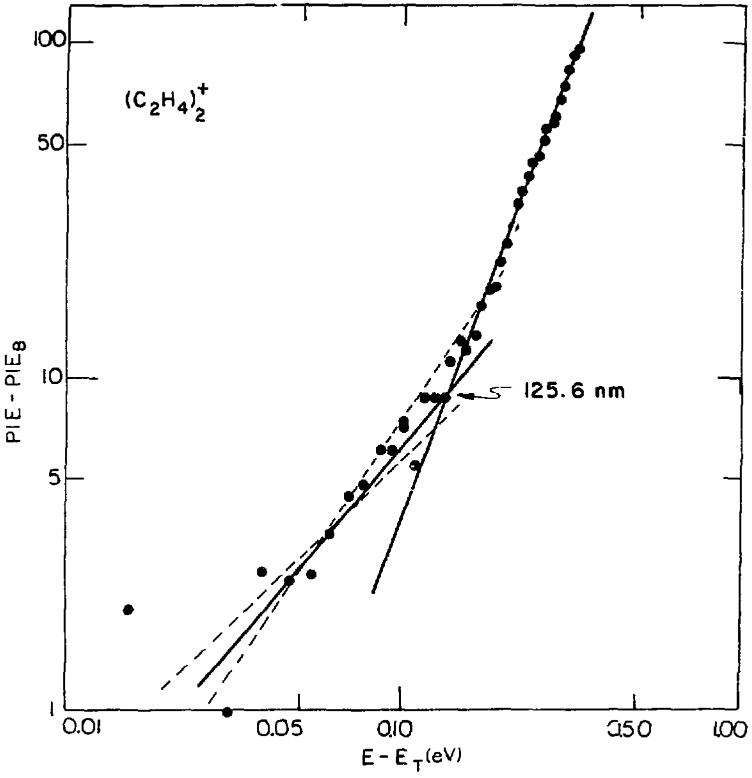

XBL 786-5241

Fig. 8. Log - log plot of the photoionization efficiency curves in the threshold region. Least squares fit for $(C_2H_4)_2^+$ points yield two lines which intersect at E - E_T = 0.15 eV or 125.6 nm, where E_T is threshold energy and PIE_B is average background ion intensity.

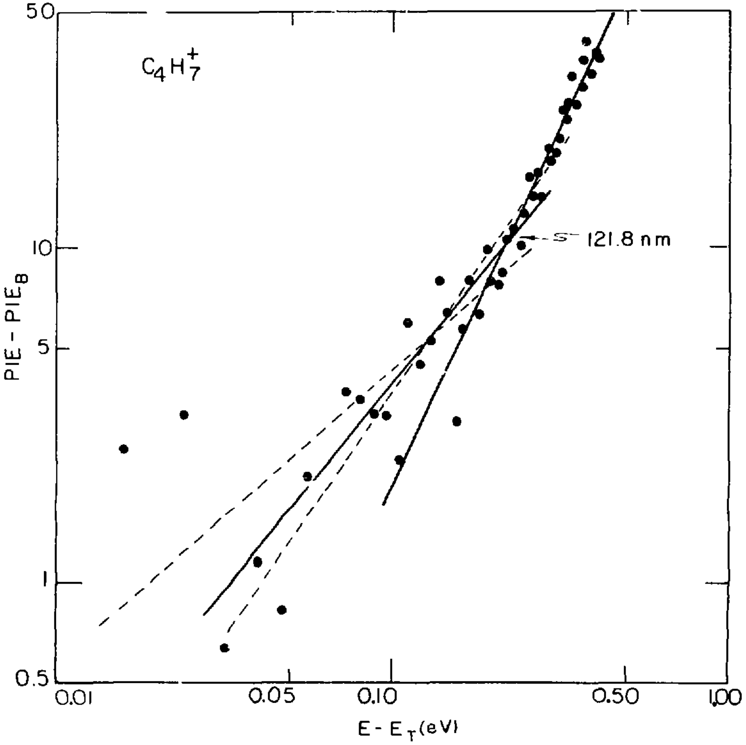

XBL 786-5239

Fig. 9. Log - log plot of threshold region of $C_4H_7^+$. Change in slope occurs at 121.8 nm.

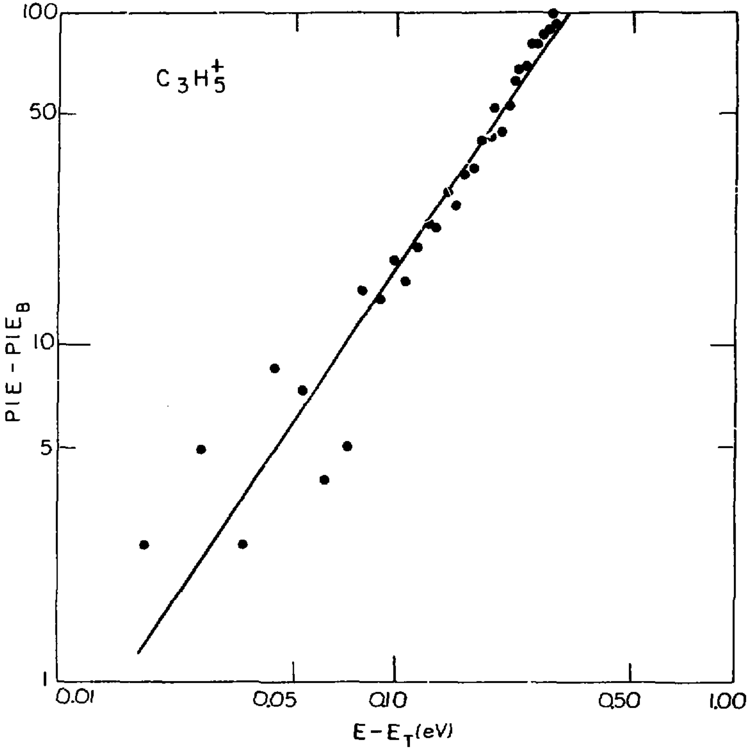

XBL 786-5240

Fig. 10. Log - log plot of threshold region of $C_3H_5^+$.

Since the photoionization of these clusters involves ionization of one of the C_2H_4 molecules, the stable ion-cluster, a precursor to the intermediate in ion-molecule reactions, is produced. The stability of the ion cluster is determined from its threshold energy of formation. The appearance potentials for $(C_2H_4)_2^+$ and $(C_2H_4)_3^+$ along with the ionization potential[25] of C_2H_4 and the neutral interaction energy of 0.42 ± 0.03 kcal[26] (assuming the clusters to be formed from ground state molecules) yield the $(C_2H_4)^+C_2H_4$ well depth as 18.2 ± 0.5 kcal and the $(C_2H_4)_2^+C_2H_4$ well depth as 4.2 ± 0.7 kcal:

$$\begin{array}{lcl|lrcl}
2C_2H_4 & \longrightarrow & (C_2H_4)_2 & \Delta E = & -0.42 & \pm & 0.03\text{ kcal} \\
(C_2H_4)_2 & \longrightarrow & (C_2H_4)_2^+ + e & & 224.3 & \pm & 0.5 \\
C_2H_4^+ + e & \longrightarrow & C_2H_4 & & -242.1 & \pm & 0.2 \\
\hline
C_2H_4 + C_2H_4^+ & \longrightarrow & (C_2H_4)_2^+ & \Delta E = & -18.2 & \pm & 0.5\text{ kcal}
\end{array}$$

$$\begin{array}{lcl|lrcl}
(C_2H_4)_2 + C_2H_4 & \longrightarrow & (C_2H_4)_3 & \Delta E = & -0.42 & \pm & 0.03\text{ kcal} \\
(C_2H_4)_3 & \longrightarrow & (C_2H_4)_3^+ + e & & 220.5 & \pm & 0.5 \\
(C_2H_4)_2^+ + e & \longrightarrow & (C_2H_4)_2 & & -224.3 & \pm & 0.5 \\
\hline
(C_2H_4)_2^+ + C_2H_4 & \longrightarrow & (C_2H_4)_3^+ & \Delta E = & -4.2 & \pm & 0.7\text{ kcal}
\end{array}$$

With increased internal excitation both the dimer and the trimer exhibit hydrogen atom and methyl radical elimination. The threshold energy of formation then corresponds to the highest barrier along the reaction coordinate for decomposition. The experimental appearance potential of $C_4H_7^+$ yields 206 ± 1.5 kcal as the heat of formation for that fragment, in good agreement with the tabulated heats of formation for several structures indicated in Tables I and II. Thus, there exists no activation energy barrier for H atom elimination. The experimental appearance potential for $C_3H_5^+$ together with the heats of formation in Tables I and II indicates that there is a barrier of 8.4 ± 1.5 kcal for methyl radical elimination. These values are in rough agreement with previously measured exit channel barriers for hydrogen atom and methyl radical elimination from propylene and the butenes.[27-30]

The photoionization fragments from the trimer appear to be $C_3H_5^+$ and $C_4H_7^+$ fragments solvated by another ethylene. That is, if the $C_6H_{11}^+$ or $C_5H_9^+$ fragments formed from the trimer are considered to be of a straight chain or a cyclic structure, then the exit channel barriers for hydrogen atom and methyl radical elimination as calculated from the thresholds and tabulated heats for formation are unrealistically large. Thus, it appears that the trimer upon ionization does not rearrange but remains as a solvated complex.

Assuming that there is no barrier to hydrogen atom elimination as in the dimer case, the binding energy of the $(C_4H_7^+)C_2H_4$ complex is calculated to be 8.7 ± 1.5 kcal:

Table I. Experimental Thresholds

	nm	kcal mol^{-1}
$C_2H_4^+$	118.2 ± 0.2	242.0
$(C_2H_4)_2^+$	127.5 ± 0.3	224.3
$C_4H_7^+$	124.5 ± 0.8	229.7
$C_3H_5^+$	119.2 ± 0.4	239.9
$(C_2H_4)_3^+$	129.7 ± 0.3	220.5
$C_6H_{11}^+$	129.2 ± 0.8	221.4
$C_5H_9^+$	127.6 ± 0.4	224.1

Table II. Literature Values of ΔH°_{f}.

		ΔH°_{f}[a] kcal mol^{-1}
$C_2H_4^+$		257
$C_4H_3^+$	1 - $C_4H_8^+$	221[b]
	2 - $C_4H_8^+$	208
	c - $C_4H_8^+$	238
$C_4H_7^+$		206[b]
$C_3H_5^+$		226[b]
$C_6H_{12}^+$	1 - $C_6H_{12}^+$	208[b]
	c - $C_6H_{12}^+$	198
C_2H_4		14.52
CH_3		34.8
H		51.63

---

[a] Reference 25.

[b] ΔH°_{f} (298 K).

$$\begin{array}{lll}
(C_4H_7^+)C_2H_4 + H + e \longrightarrow (C_2H_4)_3 & \Delta E = & -221.4 \pm 1.4 \text{ kcal} \\
(C_2H_4)_3 \longrightarrow C_2H_4 + (C_2H_4)_2 & & 0.4 \pm 0.03 \\
(C_2H_4)_2 \longrightarrow C_4H_7^+ + H + e & & 229.7 \pm 0.5 \\
\hline
(C_4H_7^+)C_2H_4 \longrightarrow C_2H_4 + C_4H_7^+ & \Delta E = & 8.7 \pm 1.5 \text{ kcal}
\end{array}$$

Since the barrier to methyl radical addition is mainly due to steric hindrance and since the trimer ion is considered as a dimer ion solvated by another ethylene molecule, the exit channel barrier heights of the dimer and trimer systems are expected to be nearly equal. Thus, the $(C_3H_5^+)C_2H_4$ binding energy is calculated to be 16.22 ± 1.1 kcal:

$$\begin{array}{lll}
(C_3H_5)^+C_2H_4 + CH_3 + e \longrightarrow (C_2H_4)_3 & \Delta E = & -224.1 \pm 0.7 \text{ kcal} \\
(C_2H_4)_3 \longrightarrow C_2H_4 + (C_2H_4)_2 & & 0.42 \pm 0.03 \\
(C_2H_4)_2 \longrightarrow C_3H_5^+ + CH_3 + e & & 239.9 \pm 0.8 \\
\hline
(C_3H_5)^+C_2H_4 \longrightarrow C_3H_5^+ + C_2H_4 & \Delta E = & 16.22 \pm 1.1 \text{ kcal}
\end{array}$$

Shown in Fig.11 and 12 are proposed reaction coordinates for the dimer and trimer systems. The dots on the reaction coordinate indicate energies that were measured in this investigation. Recently, the nature of the intermediates of the ethylene ion-molecule reaction[2,14,15,31] or of the decomposition of the cyclobutane ion[32] has undergone considerable speculation. The energies and structures of the two $C_4H_8^+$

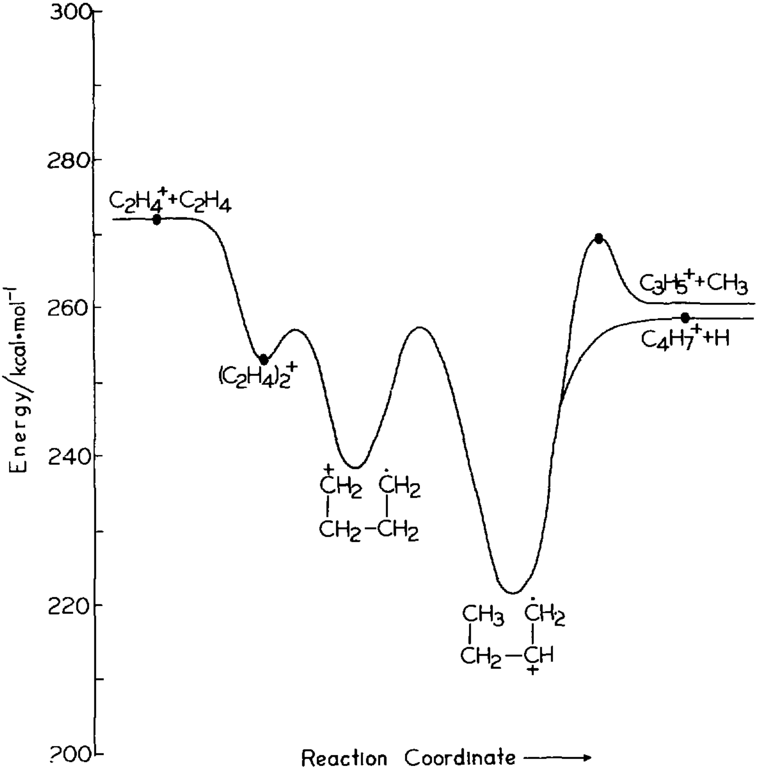

XBL 7710-6833

Fig. 11. Reaction coordinate for ethylene ion-molecule reaction. Solid dots indicate experimental values. Ordinate is heat of formation.

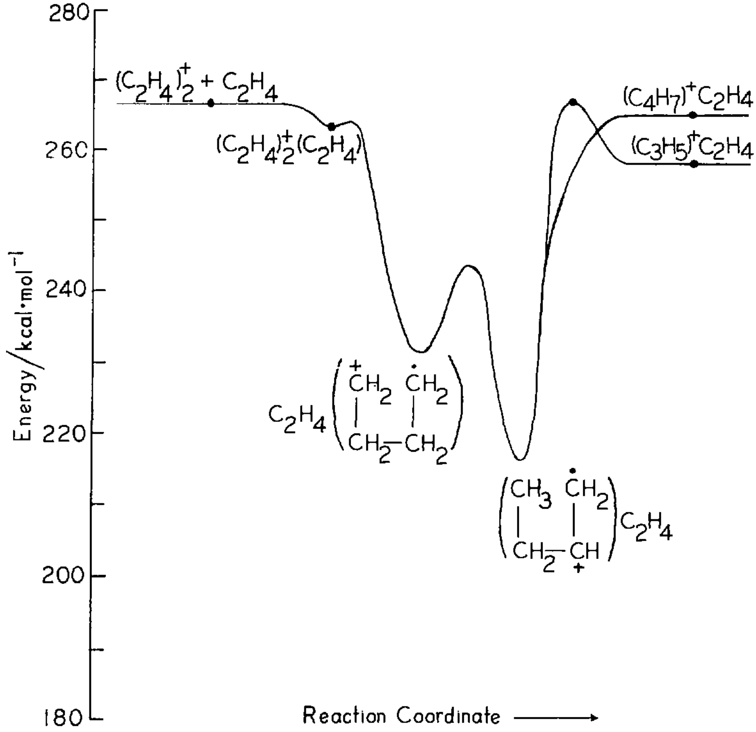

XBL 7712-10947

Fig. 12. Reaction coordinate for ethylene dimer ion-molecule reaction. Solid dots indicate experimental values. Ordinate is heat of formation.

intermediates depicted in Fig.11 and 12 have been proposed by Le Breton et al.[15] The ion cluster initially formed first rearranges into a "loose" tetramethylene radical ion[33] and then isomerizes into a more stable butane structure.[14] Since the experimental thresholds correspond to the lowest energy at which the ion cluster can decompose only the highest energy barrier in the reaction coordinate can be measured. Thus, since the thresholds for methyl radical and hydrogen atom elimination are not equal, the experimental barrier is placed in the exit channel assuming that both products originate from the same initial dimer structure.

This raises an interesting point. The fact that the $C_3H_5^+$ and $C_5H_9^+$ fragments peak at a lower stagnation pressure than their corresponding parent ions as shown in Fig. 4 may indicate the presence of two discrete van der Waals structures of the neutral dimer and trimer formed in the expansion. That is, a T-shaped dimer fragmenting exclusively to $C_3H_5^+$ would have a larger cross section for collision and thus attenuation in the nozzle-skimmer region of the source chamber would occur at lower stagnation pressures. The $C_4H_7^+$ and $C_4H_8^+$ ions may be formed from an ethylene dimer structure which would have a smaller collision cross section. The question of two distinct van der Waals structures could be resolved by attenuation experiments. That is, the $C_3H_5^+$ and $C_4H_8^+$ photoion intensities at a stagnation pressure where there is no substantial contribution from the trimer could be monitored as a function of the intensity of a secondary beam of ethylene. A similar decay of the intensities of the two ions due to their like cross sections would rule out two structures of the van der Waals dimer.

However, contamination of $(C_2H_4)_2^+$ and $C_4H_7^+$ from fragmenting ethylene trimer should occur more readily than fragmentation of the trimer to $C_3H_5^+$ thus shifting these peak intensities to higher stagnation pressures. If one assumes that the $C_3H_5^+$ and $C_5H_9^+$ fragments originate only from the dimer and trimer ions respectively and then adds together the $C_3H_5^+$ and $C_5H_9^+$ pressure dependence curves each multiplied by an appropriate factor and the result then scaled to the $C_4H_8^+$ curve, the resulting curve fits the $C_4H_8^+$ curve very well between 700-1800 torr. At low stagnation pressures (300 torr) the resultant curve is a factor of four too large indicating that there are species which fragment exclusively to $C_3H_5^+$. At higher stagnation pressures the resultant curve is about 25% too large. Thus fragmentation from higher polymers at higher pressures cannot be ruled out. This may cause some of the smearing of vibrational structure seen near the $(C_2H_4)_2^+$ threshold. Attempts to uncover the power dependence of the intensity on pressure for the different species were frustrated due to the inability to control the very low stagnation pressures where attenuation of the beam does not occur.

The ethylene ion-molecule reaction has been studied in a crossed-beam mode where it was determined that the reaction to form $C_3H_5^+$ proceeded through a persistent complex intermediate at relative collision energies less than 3.25 eV.[16] Several statistical calculations of the unimolecular decay of this complex have been carried out to test the assumption of complete energy equilibration prior to decay. No energy barrier to decomposition other than the centrifugal one was employed in these calculations. The center of mass $C_3H_5^+$ translational energy distributions as a function of incident energy was fit well by decreasing the number of active modes in a "loose complex" model for the critical configuration.[34] It is well known that the broadening of the product translational distribution can be achieved by decreasing the number of active vibrations but that it can also be effected by including an exit potential barrier.[35] More recent phase space calculations[36,37] allow all the vibrational degrees of freedom of the critical configuration to be active but the resulting product translational energy distributions of both treatments are still slightly more narrow than experiment. It is known that the potential energy barrier contributes mainly to the translational and rotational degrees of freedom of the product. Inclusion of the nonrandomized energy available from descending the barrier certainly broadens the calculated distribution since the barrier height is approximately equal to the average translational energy of the $C_3H_5^+$ fragment. Thus, no conclusion about the extent of energy randomization in the ethylene ion-molecule reaction at low energy can be drawn until the details of the reaction coordinate as measured here are included in the calculations.

In summary, van der Waals clusters are excellent parent molecules for determination of ion-molecule binding energies and the highest barrier along the reaction coordinate for the decomposition in an ion-molecule reaction. The appearance potential of the ethylene dimer ion and trimer ion yields the $(C_2H_4^+)C_2H_4$ binding energy to be 18.2 ±

0.5 kcal relative to $C_2H_4^+$ and C_2H_4 and the $(C_2H_4)_2^+C_2H_4$ binding energy to be 4.2 ± 0.7 kcal relative to $(C_2H_4)_2^+$ and C_2H_4. In addition the exit channel potential barrier heights for hydrogen atom and methyl radical elimination in the exothermic ethylene ion-molecule reactions have been determined.

E. References

1. G. G. Meisels, J. Chem. Phys. 42, 2328 (1965).
2. G. G. Meisels, J. Chem. Phys. 42, 3237 (1965).
3. P. S. Gill, Y. Inel and G. G. Meisels, J. Chem. Phys. 54, 2811 (1971).
4. P. Kebarle and R. M. Haynes, J. Chem. Phys. 47, 1676 (1967).
5. A. A. Herod and A. G. Harrison, Int. J. Mass Spectrom. Ion Phys. 4, 415 (1970).
6. P. Warneck, Ber. Bunsenges. Phys. Chem. 76, 421 (1972).
7. L. W. Sieck and P. Ausloos, J. Res. Natl. Bur. Stand. A 76, 253 (1972).
8. I. H. Suzuki and K. Maeda, Int. J. Mass. Spectrom. Ion Phys. 17, 249 (1975).
9. P. G. Miasek and A. G. Harrison, J. Am. Chem. Soc. 97, 714 (1975).
10. M. T. Bowers, D. D. Elleman and J. L. Beauchamp, J. Phys. Chem. 72, 3599 (1968).
11. S. E. Buttrill, Jr., J. Chem. Phys. 52, 6174 (1970).
12. M. L. Gross and J. Norbeck, J. Chem. Phys. 54, 3651 (1971).
13. W. T. Huntress, J. Chem. Phys. 56, 5111 (1972).
14. A. J. Ferrer-Correia and K. R. Jennings, Int. J. Mass Spectrom. Ion Phys. 11, 111 (1973).
15. P. R. LeBreton, A. D. Williamson, J. L. Beauchamp and W. T. Huntress, J. Chem. Phys. 62, 1623 (1975).
16. Z. Herman, A. Lee and R. Wolfgang, J. Chem. Phys. 51, 452 (1969).
17. C. Y. Ng, Ph.D. Thesis, University of California, Berkeley, 1976.
18. C. Y. Ng, B. H. Mahan and Y. T. Lee, J. Chem. Phys. 65, 1956 (1976).

19. J. A. R. Samson, Tech. of Vacuum Ultraviolet Spectroscopy, New York, J. Wiley and Sons, Inc. 1967, pp. 139, 216.

20. P. G. Wilkinson, Can. J. Phys. 34, 643 (1956).

21. G. Herzberg, Molecular Spectra and Molecular Structure, part III, Van Nostrand, New York, 1966, p. 533.

22. A. D. Baker, C. Baker, C. R. Brundle and D. W. Turner, Int. J. Mass Spectrom. Ion Phys. 1, 285 (1968).

23. R. Botter, V. H. Dibeler, J. A. Walker and H. M. Rosenstock, J. Chem. Phys. 45, 1298 (1966).

24. B. Brehm, Z. Naturforsch. 21A, 196 (1966).

25. H. M. Rosenstock, K. Draxl, B. W. Steiner, J. T. Heron, J. Phys. and Chem. Ref. Data 6, Suppl. 1 (1977).

26. J. O. Hirschfelder, C. F. Curtiss and R. B. Bird, Molecular Theory of Gases and Liquids, Wiley, New York, 1954, pp. 1112, 1213.

27. J. M. Parson, K. Shobatake, Y. T. Lee and S. A. Rice, J. Chem. Phys. 59, 1402 (1973).

28. K. Shobatake, J. M. Parson, Y. T. Lee, and S. A. Rice, J. Chem. Phys. 59, 1416 (1973).

29. K. Shobatake, J. M. Parson, Y. T. Lee and S. A. Rice, J. Chem. Phys. 59, 1427 (1973).

30. K. Shobatake, Y. T. Lee and S. A. Rice, J. Chem. Phys. 59, 1435 (1973).

31. J. Weiner, A. Lee and R. Wolfgang, Chem. Phys. Lett. 13, 613 (1972).

32. C. Lifshitz and T. O. Tiernan, J. Chem. Phys. 55, 3555 (1971).

33. R. Huisgen, Acc. Chem. Res. 10, 199 (1977).

34. A. Lee, R. L. LeRoy, Z. Herman, R. Wolfgang and J. C. Tully, Chem. Phys. Lett. 12, 569 (1972).

35. D. R. Herschbach, Dis. Faraday Soc. 55, 233 (1973).

36. C. E. Klots, J. Chem. Phys. 64, 4269 (1976).

37. W. J. Chesnavich and M. T. Bowers, J. Am. Chem. Soc. 98, 8301 (1976).

II. ENERGETICS OF GAS PHASE PROTON SOLVATION BY NH_3

A. Introduction

Proton transfer represents a very important class of reactions in both chemistry and biology. Understanding these reactions requires knowledge of the heats of formation of the protonated species as well as the effects of solvent interactions. Both the high pressure ion source mass spectrometric technique [1-4] and ion cyclotron resonance[5] have been employed to determine relative proton affinities and the energy released upon solvation of an ionic species. The relative proton affinity is readily obtained by measurements of the equilibrium constant of the reaction $M_1H^+ + M_2 \rightleftarrows M_2H^+ + M_1$. The equilibrium constant and hence ΔG^o is measured as a function of temperature to determine the ion solvation energies of a reaction $(M_1H^+)M_2 \rightleftarrows M_1H^+ + M_2$. Absolute values of the proton affinity are usually obtained from appearance potential measurements of a protonated species produced by electron impact.[6,7] The drawback of this method is that the protonated species of many interesting molecules do not occur as fragment ions. It has recently been shown[8] in a molecular beam photoionization mass spectrometry experiment that dimer molecules produced in a supersonic expansion are excellent parent molecules for the investigation of the ion-molecule interaction potential and the photoionization production of MH^+. The finer control of ionizing radiation possible in a photoionization measurement of appearance potentials affords a more accurate means of determining thermochemical quantities such as absolute proton affinities directly from a measurement of a microscopic quantity such as a threshold energy. For instance, the stability of the ion-molecule cluster $H_2O^+ \cdot H_2O$ has been determined from the threshold energy of formation since the photoionization of the van der Waals polymer is viewed as ionization of one of the species in the parent cluster. Further excitation of the ion cluster allows the vibrational energy induced ion-molecule reaction at zero kinetic energy to proceed yielding the threshold energy of formation of H_3O^+. In this study, this technique is used to determine the proton affinity of NH_3. It is further extended to investigate the protonated species formed by decomposition of higher polymers to yield solvation energies of an ammonium ion by ammonia solvent molecules.

B. Experimental

The apparatus and procedures have been described previously (References 9,10 and previous chapter). The ammonia polymer beam was produced by expansion of the neat gas through a 0.003" dia. Monel nozzle. Seeding of the NH_3 in Ar at various mixing ratios, maintaining the same total pressure, did not improve the dimer production. Using the monochromator grating at zero order the intensity of the fragments was monitored as a function of stagnation pressure and is shown in Fig. 1. The behaviors of the protonated ammonia signal compared to the dimer ion signal and of the protonated dimer ion compared to the trimer ion signal are very similar, indicating the dominant parent species.

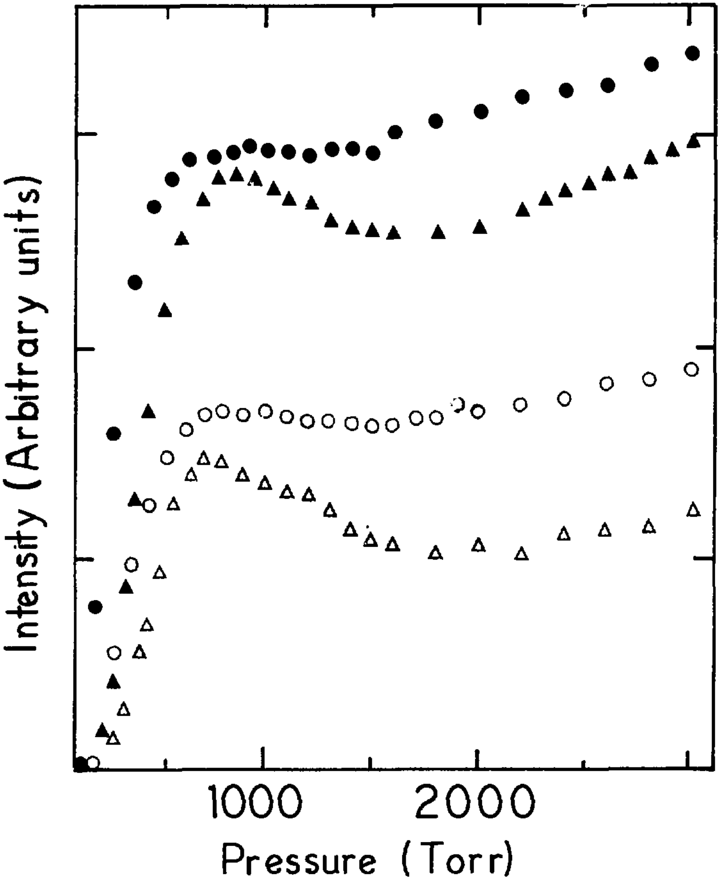

XBL 7712-10926

Fig. 1. Intensity of ions measured with the monochromator adjusted at zero order versus stagnation pressure: △$(NH_3)_3^+$, ▲$(NH_3)_2H^+$, ○$(NH_3)_2^+$, ●NH_4^+.

C. Results

The photoionization efficiency curves of the ammonia dimer ion and of the protonated ammonia species are shown in Figs. 2 and 3. The standard deviation of the signal intensity at the threshold is about 10% for $(NH_3)_2^+$ and about 5% for the protonated ammonia species. Points are measured at much lower energies than the threshold values so that an average background ion intensity can be measured. The threshold values are labeled as such when the photoionization efficiency values increase uniformly above this background ion intensity. The threshold uncertainties are taken as the difference in values obtained in two separate scans.

D. Discussion

In high pressure mass spectrometry experiments, the $NH_3^+ + NH_3 \longrightarrow NH_4^+ + NH_2$ reaction, exothermic by 0.74 eV, occurs too rapidly for the $(NH_3^+)NH_3$ intermediate to be observed by stabilization from the gas bath molecules. In our investigation, the $(NH_3^+)NH_3$ intermediate is produced directly from photoionization of the neutral dimer. In addition, its stability can be determined from the threshold energy of formation. Figure 4 shows the energetics of this system. The well depth of the neutral ammonia-ammonia interaction is taken to be 0.35 kcal/mol from fitting the temperature dependence of second virial coefficient data.[11] Combination of the neutral well depth, the ionization potential of NH_3[12] and the threshold of $(NH_3)^+_2$ formation yields the $(NH_3^+)NH_3$ binding energy as 0.79 ± 0.05 eV or 18.1 ± 1.1 kcal/mole.

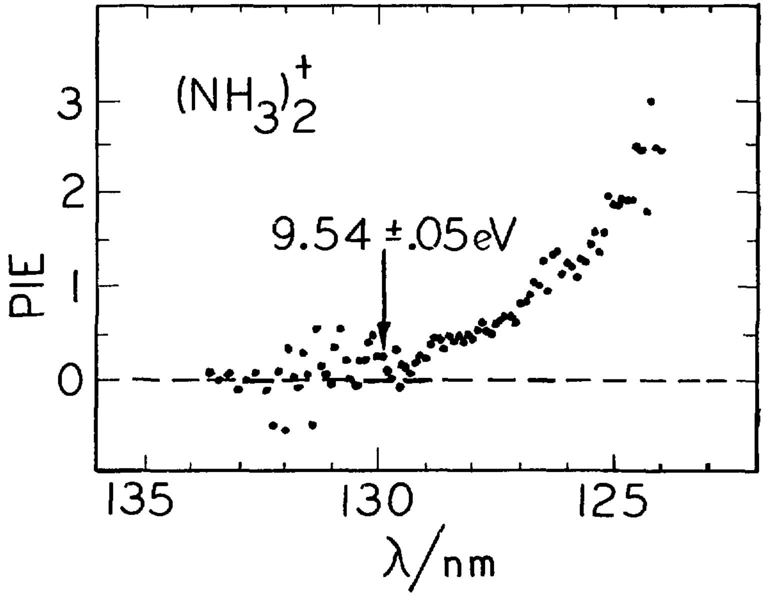

XBL 7712-10928

Fig. 2. Photoionization efficiency of $(NH_3)_2^+$ normalized to 116.0 nm.

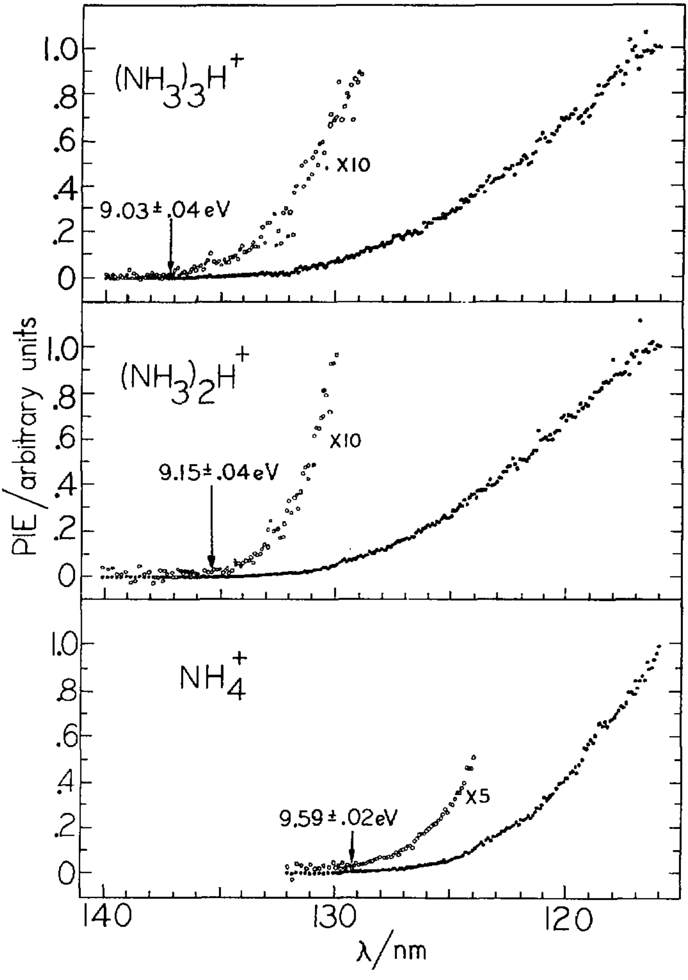

XBL 7712-10939

Fig. 3. Photoionization efficiency of NH_4^+, $(NH_3)_2H^+$ and $(NH_3)_3H^+$ normalized at 116.0 nm.

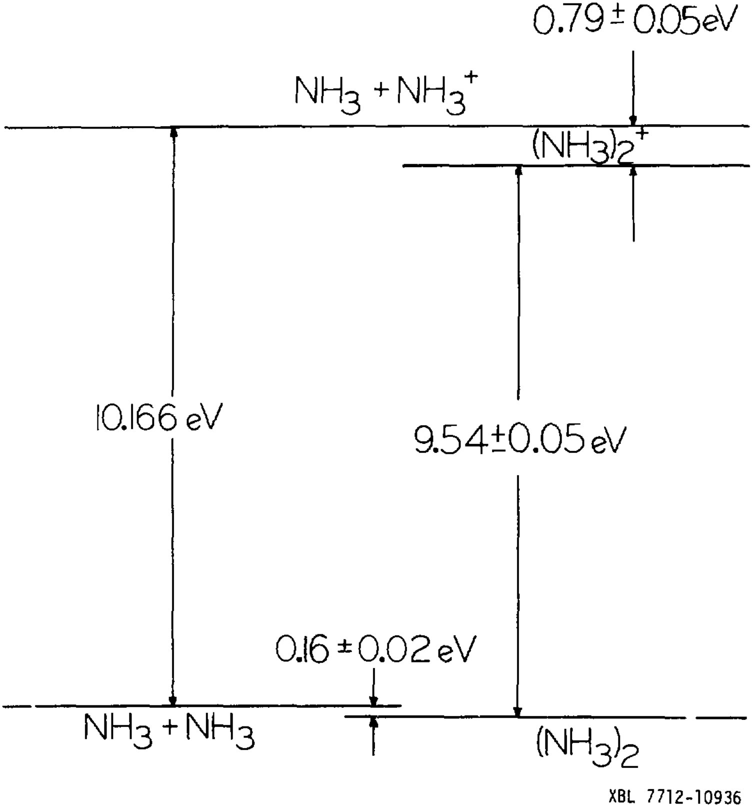

Fig. 4. Energetics of the $(NH_3)_2^+$ system.

When the internal energy of the ammonia dimer ion is increased to 0.052 eV, the onset of the NH_4^+ fragment is observed. The appearance potential of NH_4^+, the ionization potential[12] of H, the H_2N-H bond energy[13] and the neutral well depth are employed to calculate the proton affinity of NH_3 as 8.76 ± 0.06 eV or 202.1 ± 1.3 kcal/mol at 0 K as shown in Fig. 5. Assuming that all rotational degrees of freedom are excited and that no vibrational degrees of freedom are excited at 298 K, the proton affinity becomes 203.6 ± 1.3 kcal/mol at 298 K. This value is in good agreement with a recent proton affinity measurement of 202.3 kcal/mol obtained in ion cyclotron resonance thermal equilibrium experiments at 298 K.[5] The previously accepted value for the proton affinity of ammonia was 207 ± 3 kcal/mole.[6,7] Recent theoretically calculated values for the proton affinity of NH_3 are 205.3[14] and 208[15] kcal/mole.

The appearance potentials of the higher protonated polymers, $(NH_4^+)NH_3$, a fragment from excited $(NH_3)_3^+$, and $(NH_4^+)(NH_3)_2$, a fragment from excited $(NH_3)_4^+$, allow the solvation energy of an ammonium ion by one or two ammonia molecules to be calculated via the cycles shown in Fig. 5. These values are listed in Table I along with literature values for the solvation energies.

It is clear from Table I that the agreement between the solvation energies measured in this study and the literature values is not good. The theoretical values from ab initio SCF calculations are too large probably due to the limited basis set employed. The experimental values are obtained by high pressure ion source mass spectrometry. One very common criticism of the photoionization technique for measuring appearance potentials is that the threshold may not correspond to the ground vibrational state of the ion but rather to some upper vibrational

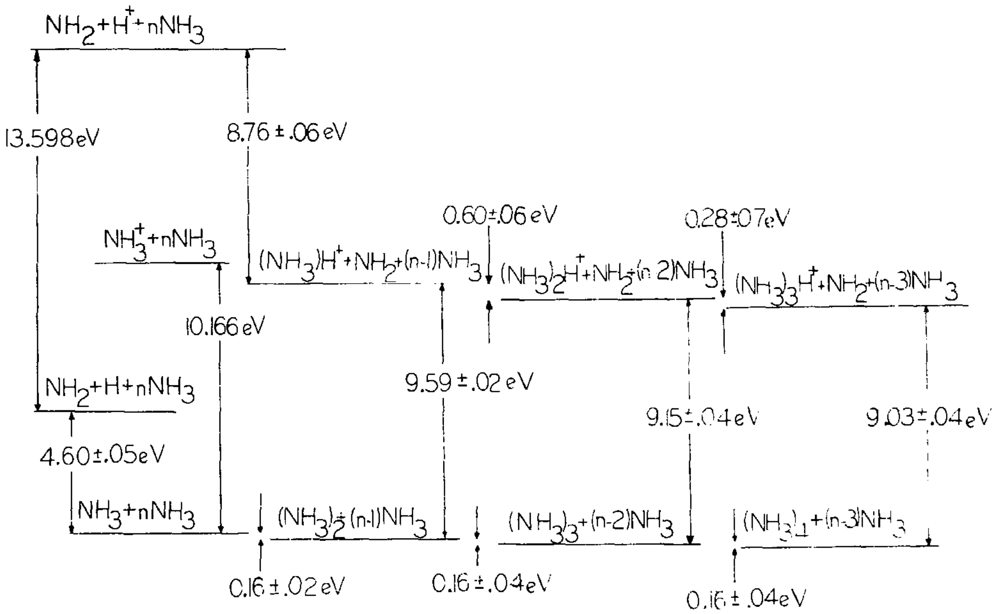

XBL 7712-10940

Fig. 5. Energetics of the protonated ammonia system.

TABLE I Energetics of proton solvation by NH_3

$$NH_4^+(NH_3)_n \rightleftarrows NH_4^+(NH_3)_{n-1} + NH_3$$

	THIS WORK	LITERATURE		THEORETICAL
n, n-1	ΔH°_0 kcal mol^{-1}	ΔH°_{298}	ΔG°_{298}	ΔH°_0
1,0	13.8 ± 1.4	18.4[a]	6.3[a]	28.1[e]
		21.5[b]	15.5[b]	36.0[f]
		24.[illegible]	17.1[c]	27.6[g]
		27.0[d]	17.5[d]	
			10.8[h]	
2,1	6.4 ± 1.6		5.5[a]	
		16.2[b]	9.4[b]	
		17.5[c]	8.9[c]	
		17.0[d]	9.0[d]	
			9.7[h]	

---

a) Ref. 17

b) Ref. 4

c) Ref. 2

d) Ref. 20

e) Ref. 18

f) Ref. 19

g) Ref. 16

h) Ref. 3

ionic state.[21] This is true when large changes in geometry of the molecule occur upon ionization. Vibrationally excited ions would lead to higher thresholds and thus lower absolute values of the solvation energies. In our case, however, the process that is essentially occurring is the unimolecular decomposition of the vibrationally excited parent clusters $(NH_3)_2^+$, $(NH_3)_3^+$ and $(NH_3)_4^+$. Franck-Condon factors will not play an important role in this case. If there is no barrier for proton transfer the threshold should correspond to the threshold of decomposition. Nevertheless, let us assume that the difference in energies between the two most recent high pressure mass spectrometry values[2,4] and the photoionization value is due to vibrational excitation of the resulting ion in the photoionization experiments and that the kinetic energy of the electron is zero. Thus, the $(NH_4^+)(NH_3)_2$ produced will have (42.3-20.2) = 22.1 kcal/mol[2] or (37.7-20.2) = 17.5 kcal/mol[4] of excitation energy. Both these values are larger than the corresponding dissociation energies of 17.5[2] or 16.2 kcal/mol[4] for $(NH_4^+)(NH_3)_2$. Clearly, the notion that the ions $(NH_4^+)(NH_3)_2$ formed by photoionization of clusters are vibrationally excited is inconsistent with the equilibrium solvation energies.

The onset of the decomposition of the higher polymers to yield NH_4^+ serves as a check on the threshold measurements. The energy required to produce NH_4^+ from $(NH_3)_3$ can be calculated from the data in Fig. 5; one obtains that the threshold for the reaction $(NH_3)_3 \rightarrow NH_4^+ + NH_3 + NH_2 + e$ should occur at 9.75 eV or 127.2 nm. A plot of the log of the photoionization efficiency minus the background ion count versus log $(E-E_T)$ where E_T is the threshold of NH_4^+ is shown in Fig. 6. The least squares line fit to the two slopes intersects

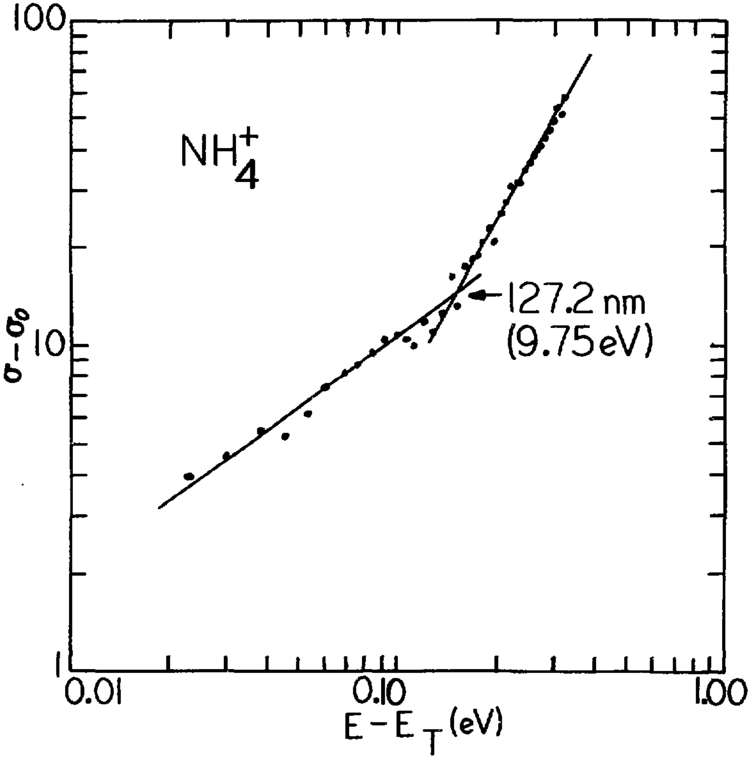

XBL 7712-10924

Fig. 6. Log $(\sigma-\sigma_o)$ where σ = photoionization efficiency, σ_o = background ion count versus log $(E-E_T)$ where E_T = threshold energy of NH_4^+.

at exactly 127.2 nm, corresponding to a new channel for NH_4^+ formation. The decomposition of the tetramer to NH_4^+ should occur at 125.0 nm. In the photoionization efficiency curve of NH_4^+ in Fig. 3, a change of slope is distinct at 125.0 nm. Similarly, there are distinct changes in slope of the photoionization efficiency curves of $(NH_4^+)NH_3$ and $(NH_4^+)(NH_3)_2$ shown in Figs. 7 and 8. The fact that fragmentation of higher polymers into smaller ions (involving loss of NH_2 and one or more NH_3 molecules) is predicted correctly by the appearance potentials of NH_4^+ and $(NH_3)_2H^+$ indicates that the observed thresholds are self consistent and suggest that they do not correspond to vibrationally excited ions.

In summary, the proton affinity of NH_3 has been determined by measuring the appearance potential of NH_4^+ formed to be 202.1 ± 1.3 kcal/mol at 0 K from decomposition of the ammonia dimer ion. The proton solvation energies by more than one ammonia have been determined by measuring the appearance potential of fragments from larger cluster ions. The appearance potential of the dimer ions formed from the neutral van der Waals dimer yields the binding energy of NH_3^+-NH_3 to be 18.1 ± 1.1 kcal/mole.

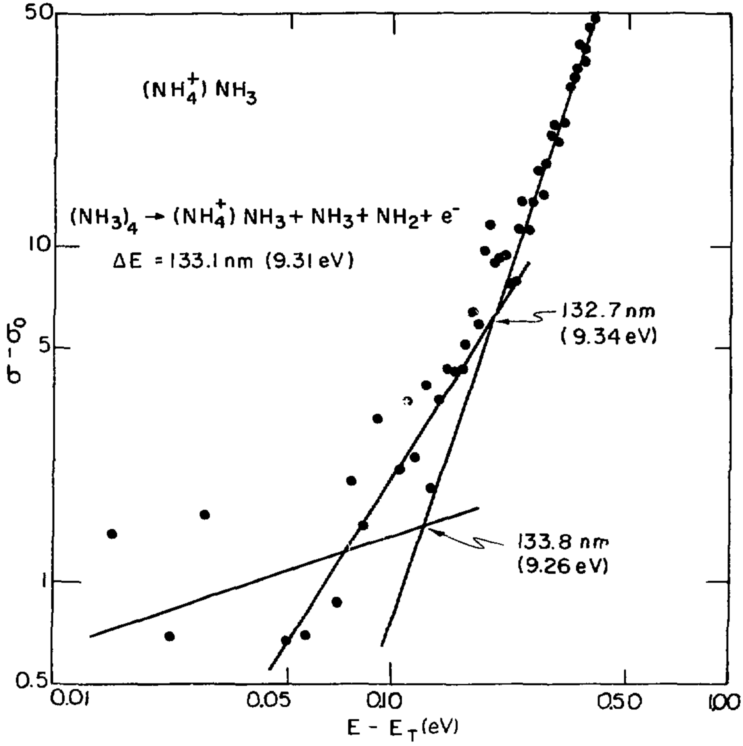

XBL 786-5242

Fig. 7. Log-log plot of the photoionization efficiency of $(NH_4)^+NH_3$ in the threshold region. E_T is the threshold energy of $(NH_4^+)NH_3$. Two limiting lines are drawn through the low energy points, establishing maximum errors for the $(NH_3)_n$ dissociation energy.

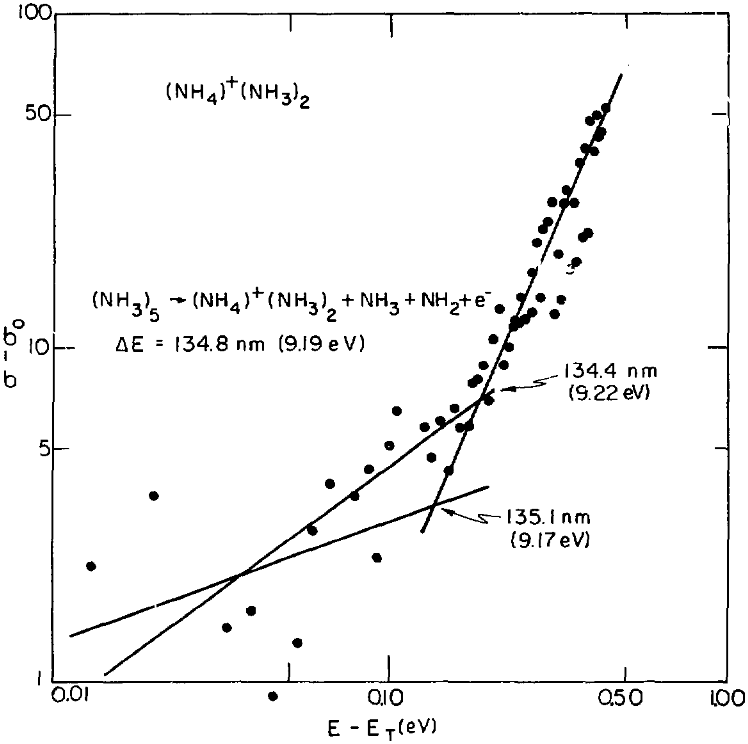

XBL786-5243

Fig. 8. Log-log plot of the photoionization efficiency of $(NH_4^+)(NH_3)_2$ in the threshold region. E_T is the threshold energy of $(NH_4^+)(NH_3)_2$. Two limiting lines are drawn through the low energy points, establishing maximum errors for the $(NH_3)_n$ dissociation energy.

E. References

1. A.J. Cunningham, J.D. Payzant and P. Kebarle, J. Am. Chem. Soc. 94, 7627 (1972).

2. J.D. Payzant, A.J. Cunningham and P. Kebarle, Can. J. Chem. 51, 3242 (1973).

3. F.C. Fehsenfeld and E.E. Ferguson, J. Chem. Phys. 59, 6272 (1973).

4. M.R. Arshadi and J.H. Futrell, J. Phys. Chem. 78, 1482 (1974).

5. J.F. Wolf, R.H. Staley, I. Koppel, M. Taagepera, R.T. McIver, Jr., J.L. Beauchamp, R.W. Taft, J. Am. Chem. Soc. 99, 5417 (1977).

6. M.A. Haney and J.L. Franklin, J. Chem. Phys. 50, 2028 (1969).

7. M.A. Haney and J.L. Franklin, J. Phys. Chem. 73, 4328 (1969).

8. C.Y. Ng, D.J. Trevor, P.W. Tiedemann, S.T. Ceyer, P.L. Kronebusch, B.H. Mahan and Y.T. Lee, J. Chem. Phys. 67, 4235 (1977).

9. C.Y. Ng. Ph.D. Thesis, University of California, Berkeley, 1976.

10. C.Y. Ng. B.H. Mahan, and Y.T. Lee, J. Chem. Phys. 65, 1956 (1976).

11. The value of 3.5 kcal was chosen since i [illegible] a ΔH_0^o value obtained from fitting the temperature dependence of second virial coefficient data by J.S. Rowlinson, Dis. Far. Soc. Trans. 45, 974 (1949). Other experimental values for ΔH^o_{298} in the literature are 4.4 kcal by J.D. Lambert and E.D.T. Strong, Proc. Roy. Soc. 200, 566 (1950), 4.5 kcal by J.E. Lowder, J. Quant. Spec. Radiat. Transfer, 10, 1085

(1970) and 2.8 kcal by G. Duquette, T.H. Ellis, G. Scoles, R.O. Watts, M.L. Klein, J. Chem. Phys. 68, 2544 (1978).

12. H.M. Rosenstock, K. Draxl, B.W. Steiner and J.T. Herron, J. Phys. and Chem. Ref. Data, 6, Suppl. 1, 1977.

13. D.K. Bohme, R.S. Hemsworth and H.W. Rundle, J. Chem. Phys. 59, 77 (1973).

14. A. L. Goodliffe, H.D.B. Jenkins, S.V. Martin, and T.C. Waddington, Mol. Phys. 21, 761 (1971).

15. L.P. Tan and J.W. Linnett, J. Chem. Soc. Chem. Comm. 10, 364 (1976).

16. J.J. Delpuech, G. Serratrice, A. Strich and A. Veillard, J. Chem. Soc. Chem. Comm. 14, 817 (1972).

17. H. Wincel, Int. J. Mass Spectrom. and Ion Phys. 9, 267 (1972).

18. J.J. Delpuech, G. Serratrice, A. Strich and A. Veillard, Mol. Phys. 29, 849 (1975).

19. P. Merlet, S.D. Peyerimhoff and R.J. Buenker, J. Am. Chem. Soc. 94, 8301 (1972).

20. S.K. Searles and P. Kebarle, J. Phys. Chem. 72, 742 (1968).

21. W.A. Chupka, Chem. Spect. and Photochemistry in the Vacuum Ultraviolet (Ed. C. Sandorfy, P.J. Ausloos and M.B. Robin) D. Reidel Publishing Co., Boston.

PART II. MOLECULAR BEAM GAS-SURFACE SCATTERING

III. SCATTERING OF THERMAL HELIUM BEAMS FROM A HIGH-MILLER INDEX PLATINUM SINGLE CRYSTAL SURFACE

A. Introduction

There is much interest in the use of elastic scattering of light atoms from surfaces for the extraction of the gas-surface interaction potential by means of the observed structure in the angular distribution measurements. The use of light atom diffractive scattering to deduce surface structure and surface Debye temperature has received less attention, mainly due to the inability of most metal surfaces to exhibit light atom diffraction spectra and to the comparatively easy technique of LEED to obtain similar information.

Helium, Ne, H, and D scattering from the alkali halide single crystals of LiF and NaF have been the only systems intensively studied[1-7] and have shown well-defined diffraction peaks. These experiments are generally of a finer quality than earlier ones, due to the clean, well-characterized surfaces employed,[1-4] the use of low surface temperatures, which reduce the inelastic background,[1,4,5] and the use of well-collimated supersonic[1-5] or velocity selected incident beams.[6]

Two reports of diffraction from metal surfaces have not been very convincing.[8,9] Very recently however, He and H_2 diffraction has been observed from a Ag(111) surface in high resolution apparatuses.[10,11] In both reports, the surface was cooled to below or near the surface Debye temperature in order to minimize inelastic transitions. The first order diffraction peaks are of the order of 1000 times less intense than the specular peak. Interestingly, the intensity of H_2 diffraction is significantly greater than that for He diffraction. Hopefully, the observation of diffraction from metal surfaces will yield information about the interaction potential of some chemically important systems.

This study[12] explores the scattering of helium atomic beams from high Miller index platinum surfaces that exhibit ordered, periodic steps on the atomic scale to probe the effect of atomic steps on the helium atom scattering distribution. These studies examine how the periodic surface structure, i.e., monatomic steps, ~2.3 Å in height, separated by ordered atomic terraces of five atoms wide (~11 Å) on the average, is seen by an atomic beam incident on such a surface from various directions.

Rainbow scattering is observed when the step edges are perpendicular to the incident helium atoms. Rainbow peaks result from an accumulation of trajectories at two angles that correspond to the maximum and minimum scattering angles introduced by the periodic surface potential.[13] A rainbow scattering distribution then can yield information about the repulsive shape of the surface potential. The rainbow scattering distributions observed here are in agreement with the ordered periodic step structure of the surface indicated by LEED. Diffraction is not observed in these experiments for reasons well understood and described below.

B. Experimental

The ultra-high vacuum molecular beam surface scattering apparatus in which these experiments were carried out as well as the surface preparation and characterization has been described previously in detail.[14] The procedure for these experiments has also been described.[14,15]

A diagram of the experimental arrangement is shown in Fig. 1. Briefly, the room temperature helium beam is formed by effusion from a multichannel capillary array. The beam is modulated at 160 Hz by a mechanical chopper. The pressure of the beam at the surface is about 10^{-7} torr. AC detection of the scattered beam by a quadrupole mass spectrometer in the plane defined by the incident beam and the surface normal is employed. The surface temperature in these experiments is ~1100 K.

The platinum single crystal surface used in this study is designated by its Miller indices as Pt(553). A more descriptive nomenclature for the stepped surface designates the Pt(553) as Pt(S)-[5(111)x(111)]. The (111) surface is the hexagonal close-packed plane in which each atom has six nearest neighbors. The (553) surface is cut 12.27° from the (111) plane in the <111> direction resulting in a surface characterized by ordered monatomic steps of (111) orientation. These steps are separated by terraces of (111) orientation which are on the average five atoms wide. It is shown schematically in Fig. 2.

The crystal is mounted on a manipulator which extends from the top of the main scattering chamber and provides several degrees of

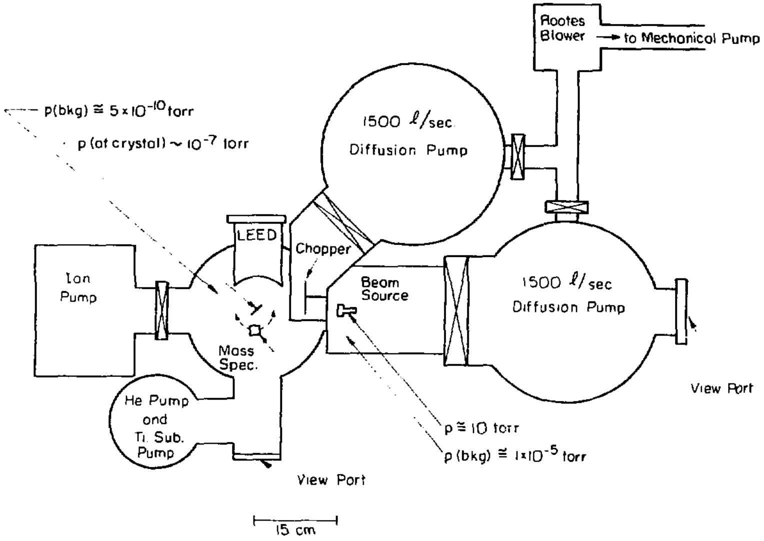

MOLECULAR BEAM SURFACE SCATTERING APPARATUS

XBL 732-5744A

Fig. 1. Schematic diagram of ultra-high vacuum molecular beam scattering apparatus.

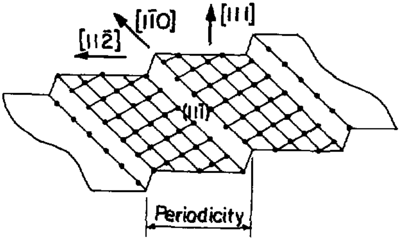

Fig. 2. Schematic diagram of the platinum surface studied in this work: Pt(553) or Pt(S)-[5(111)x(111)].

freedom of motion for the crystal. To measure the incident beam intensity and thus normalize all the measurements, the crystal can be translated upward out of the beam line. The angle of incidence, θ_i, can be varied by rotating the crystal around its diameter perpendicular to the plane defined by the incident beam and the macroscopic surface normal as seen in Fig. 3. Further, it is possible to vary the azimuthal angle ϕ (the orientation of the step edges with respect to the plane defined by the incident atomic beam and the macroscopic surface normal), by rotating the crystal around its center in its own plane as shown in Fig. 3. The azimuthal orientation is determined by LEED patterns to an accuracy of ±5°.

Before each run, the platinum single crystal is heated in an ambient pressure of oxygen of 5×10^{-6} torr for one and one-half hours to provide an uncontaminated surface as established by Auger Electron Spectroscopy. Low-Energy Electron Diffraction shows the presence of well-ordered atomic domains of the stepped platinum surface.

It should be noted that while the macroscopic surface is always 45° (or some other constant angle of incidence) from the incident beam at any azimuthal angle of rotation, the microscopic stepped surface is not. Since the helium atom "sees" the surface on the atomic scale, a variable fraction of the helium beam scatters outside the plane of the detector which is lined up with respect to the macroscopic surface normal. In these experiments the scattering distribution

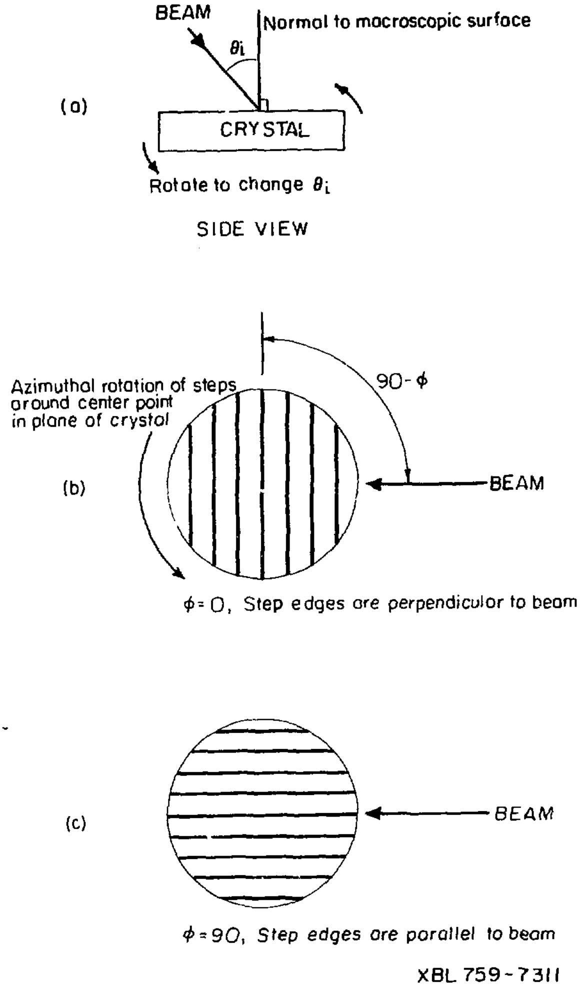

Fig. 3. Diagram defining: (a) θ_i, angle of incidence and (b) ϕ, azimuthal angle.

is measured only in the plane defined by the incident beam and the macroscopic surface normal.

C. Results

Figures 4a-e show the scattering distributions from the platinum (553) surface for various azimuthal orientations. Each distribution except for azimuthal angle $\phi = 24°$ (where $\phi = 0°$ when the step edges are perpendicular to the incident beam and $\phi = 90°$ when the beam impinges on the crystal along the step edges) is an average of at least two different runs with error bars indicative of the scatter in the points at each angle sampled. Each point is an average of at least twelve values. The intensity scattered into the solid angle subtended by the detector at a given scattering angle is normalized to the incident beam. The angle of incidence in each case is indicated by the arrow on the horizontal axis of the distribution as 45°.

The effect of varying the azimuthal orientation of the crystal step edges to the incident molecular beam, while the angle of incidence is held constant, is dramatic. Note that as the incident beam comes in along the step edges, the total scattering distribution becomes less intense due to out-of-plane scattering. Since the detector is mounted in the plane of incidence defined by the macroscopic surface normal and the incident beam, it does not sample molecules scattered out-of-plane. The peak intensity of the cone-shaped distribution also shifts in space as the azimuthal orientation of the crystal is changed. Only

Fig. 4a. Normalized scattered intensity vs. angle from surface normal for the azimuthal angle $\phi = 79°$ with a fixed angle of incidence of 45° for a Pt(553) surface.

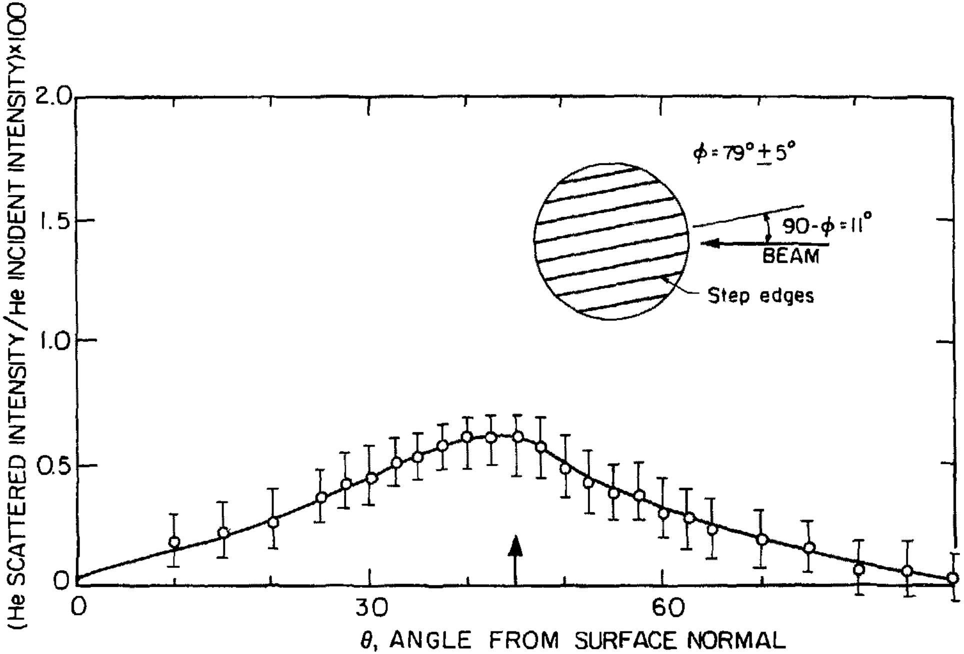

Fig. 4a

XBL 759-7312

Fig. 4b. Normalized scattered intensity vs. angle from surface normal for the azimuthal angle $\phi = 51°$, with a fixed angle of incidence of 45° for a Pt(553) surface.

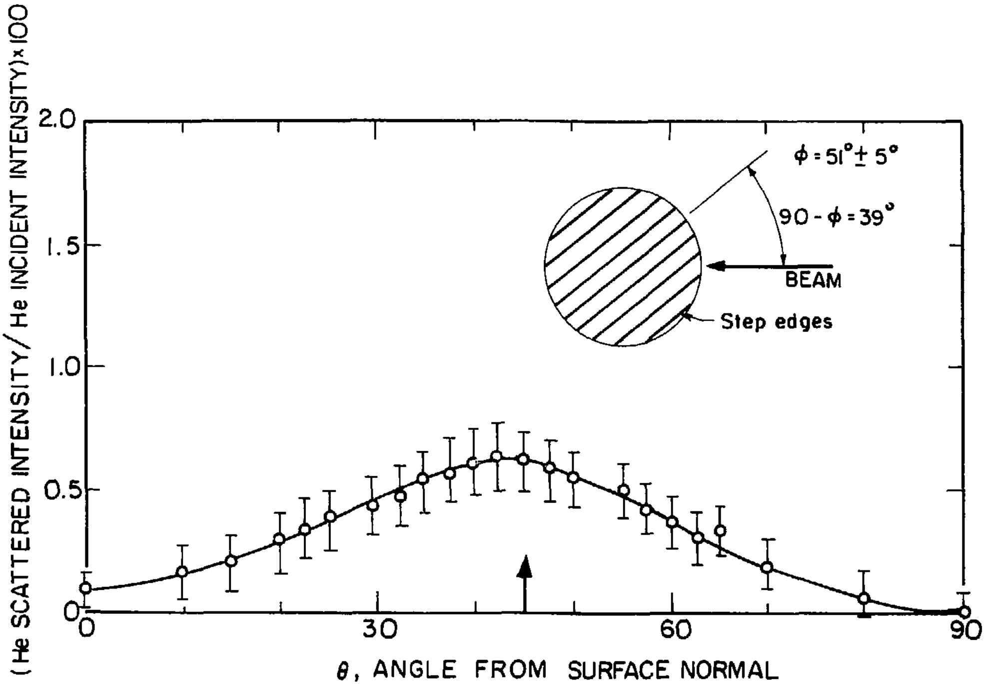

Fig. 4b

XBL 759-7313

Fig. 4c. Normalized scattered intensity vs. angle from surface normal for the azimuthal angle $\phi = 39°$, with a fixed angle of incidence of 45° for a Pt(553) surface.

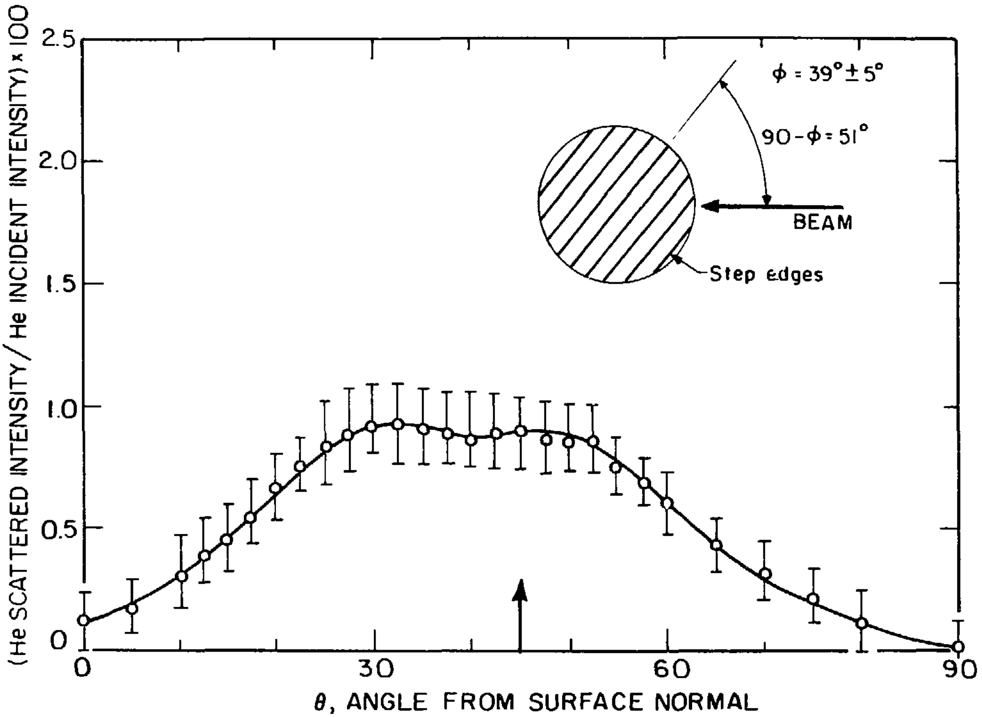

Fig. 4c

XBL 759-7314

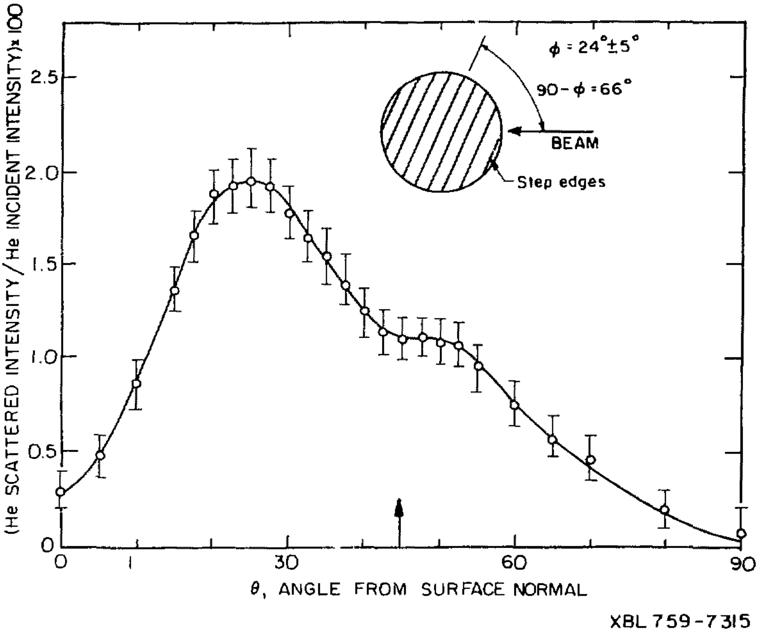

Fig. 4d. Normalized scattered intensity vs. angle from surface normal for the azimuthal angle φ = 24°, with a fixed angle of incidence of 45° for a Pt(553) surface.

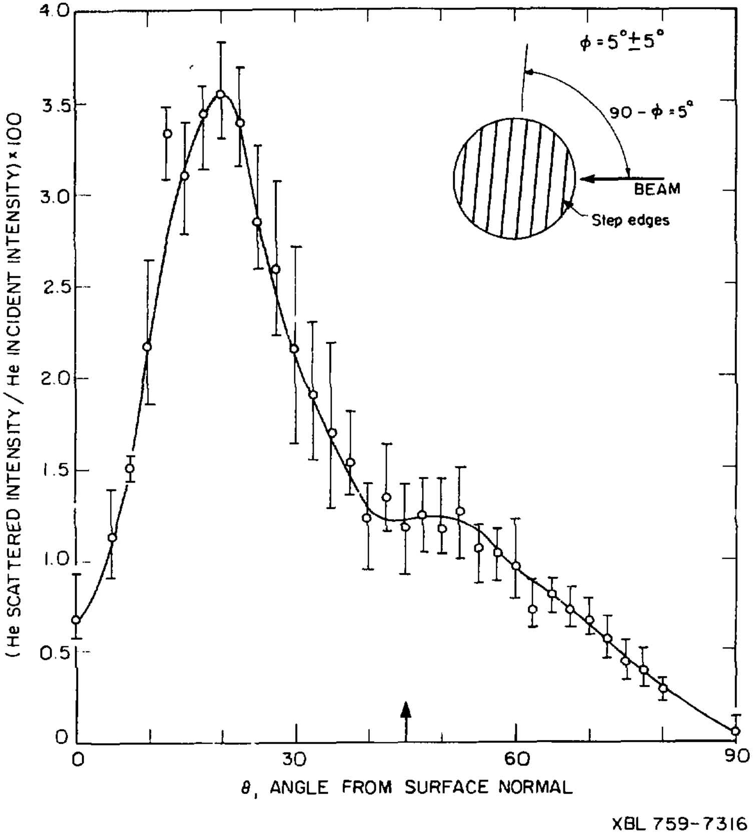

Fig. 4e. Normalized scattered intensity vs. angle from surface normal for the azimuthal angle $\phi = 5°$, with a fixed angle of incidence of 45° for a Pt(553) surface.

when the step edges are perpendicular to the incident beam does the detector sample directly along the axis of the cone as indicated in Fig. 5. At any other azimuthal orientation, the detector "sees" only slices of the scattering distribution, since the axis of the scattered cone lies out of the plane defined by the macroscopic surface normal and the detector.

Two further observations can be made. There is a definite shift toward the surface normal of the more intense peak and the appearance of a second peak or shoulder near the specular as the steps are oriented in a more perpendicular direction to the incoming beam.

This shift toward the macroscopic surface normal reaches a maximum of 25° from the specular when the step edges are perpendicular to the incident beam. Whether this shift is observed toward the macroscopic surface normal or away from it depends on whether the open edge of the step is away from the incident beam or into it. In this investigation, the molecular beam was oriented away from the open step edge.

Figures 6a-d show the effect of varying the angle of incidence on the double-peaked scattering distribution for a fixed azimuthal angle of $\phi = 5°$. Each of these distributions is an average of at least two runs. Again, the arrow on the abscissa indicates the angle of incidence. The two peaks in the scattering distribution coalesce as the angle of incidence is increased. The intensity of these two peaks also increases as the angle of incidence is increased.

Fig. 5. Schematic diagram defining the macroscopic surface normal and the terrace normal:

(a) *The steps are oriented so that they are perpendicular* to the incident beam. Note that the incident beam, the normal to the terrace N_t, the macroscopic normal N_m, the scattered distribution and the detector are all situated in one plane, the plane of the paper. In this case, the incident beam is oriented away from the open edge of the step.

(b) The incident beam (not shown) impinges on the filled circle at a 45° angle of incidence to the paper, but in the plane of the macroscopic normal or along the step edges. The normal to the terrace and to the macroscopic surface are now normal to a plane which is perpendicular to the plane of the paper. Note that the incident beam, the macroscopic normal and the detector are in one plane while the scattering distribution is out of the plane sampled by the detector.

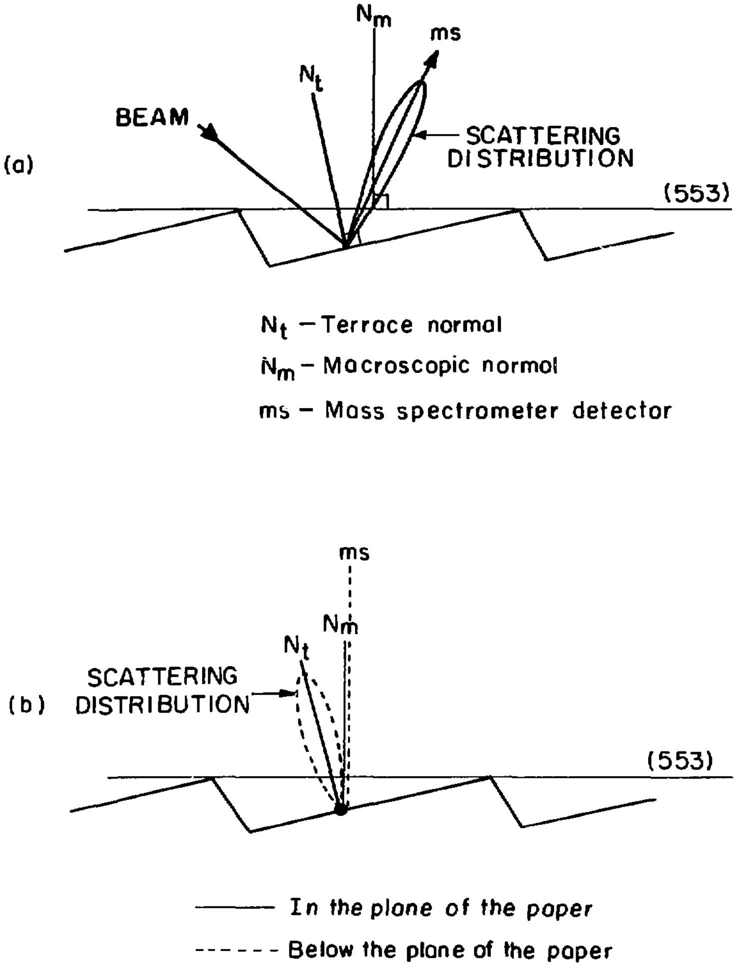

XBL 759-7317

Fig. 5

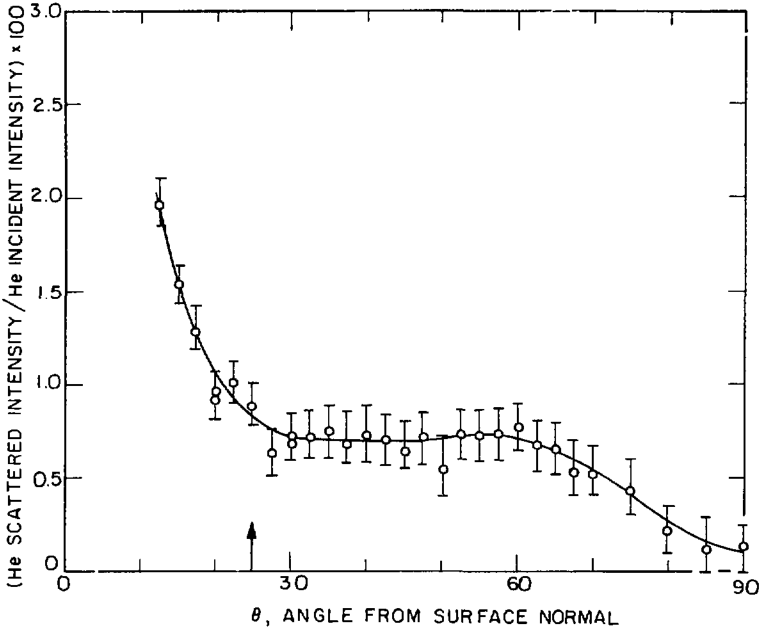

XBL 759-7318

Fig. 6a. Normalized scattered intensity vs. angle from surface normal for a fixed azimuthal angle $\phi = 5°$ with the angle of incidence from a Pt(553) surface at $\theta_i = 25°$.

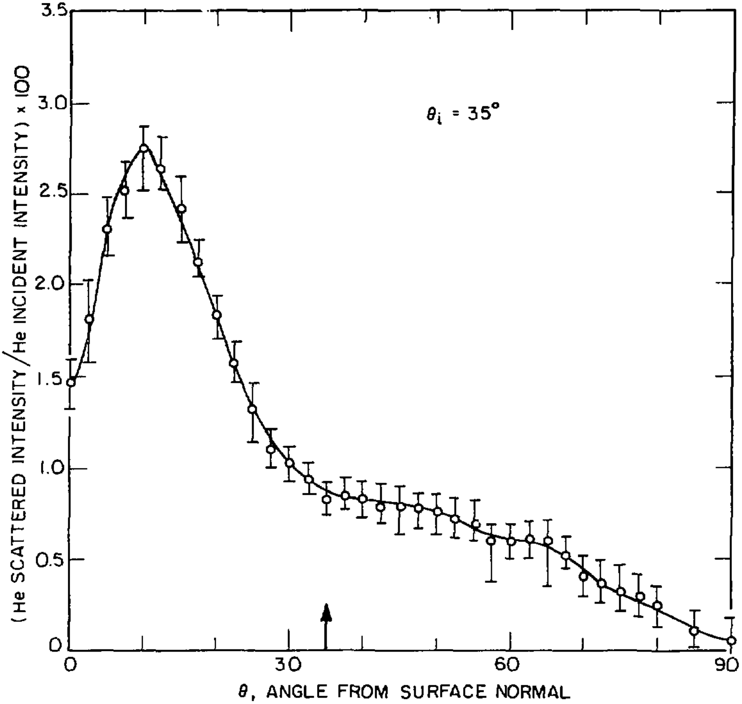

XBL 759-7319

Fig. 6b. Normalized scattered intensity vs. angle from surface normal for a fixed azimuthal angle $\phi = 5°$ with the angle of incidence from a Pt(553) surface at $\theta_i = 35°$.

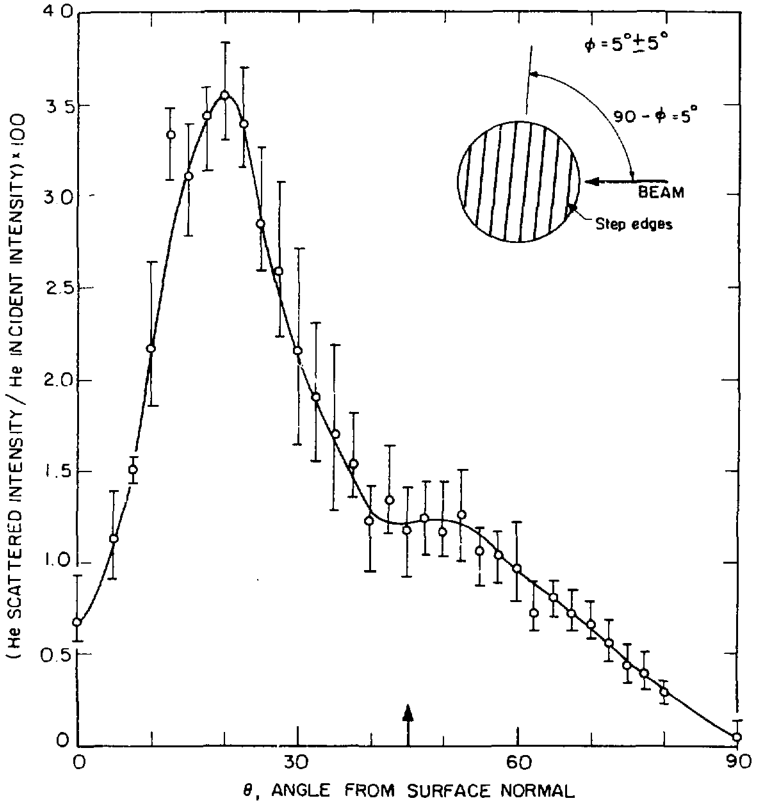

XBL 759-7316

Fig. 6c. Normalized scattered intensity vs. angle from surface normal for a fixed azimuthal angle $\phi = 5°$ with the angle of incidence from a Pt(553) surface at $\theta_i = 45°$.

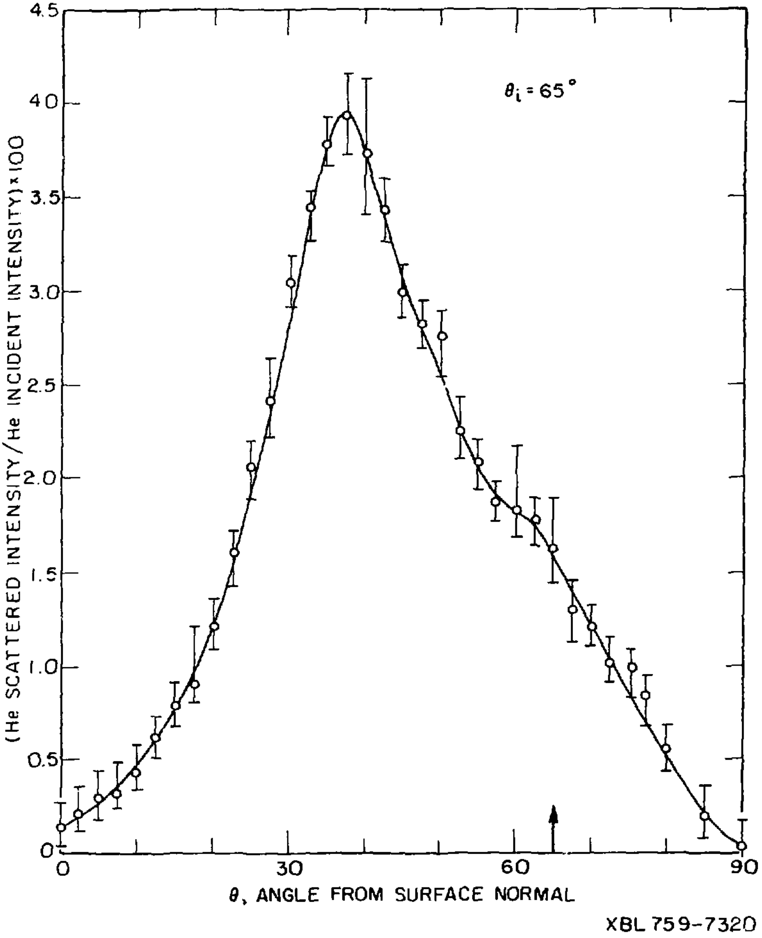

Fig. 6d. Normalized scattered intensity vs. angle from surface normal for a fixed azimuthal angle ϕ = 5° with the angle of incidence from a Pt(553) surface at θ_i = 65°.

D. Discussion

Particles that scatter from the overall macroscopic surface appear at the specular angle in the scattering distribution. However, the helium atoms scatter with reference to the microscopic surface normal, rather than the macroscopic surface normal. A diagram of this effect is shown in Fig. 7, indicating the microscopic specularity when the step edges are perpendicular to the beam. The helium atom intensity scattered from the terrace normal should be shifted twice the angle of cut from the (111) plane or 25° away from the specular angle when the step edges of the Pt(553) crystal are perpendicular to the beam. This is precisely what is observed indicating that the helium atoms do indeed probe the atomic surface structure. When the azimuthal angle ϕ is equal to 90°, the angle that the incident beam makes with the normal to the terrace and the macroscopic normal is the same and no shift is observed.

The two maxima which are apparent in the scattering distribution from the platinum(553) surface when the step edges are perpendicular to the incoming beam are indicative of rainbow scattering. The distance between the two rainbow peaks and the relative intensities are greatly dependent upon the dynamical interaction between the gas and the solid and the nature of the periodic potential. In our case, rainbow scattering is only observed when the step edges are oriented almost perpendicularly to the incident beam. The periodicity as seen by the incoming atom is very much reduced when the beam comes in along the

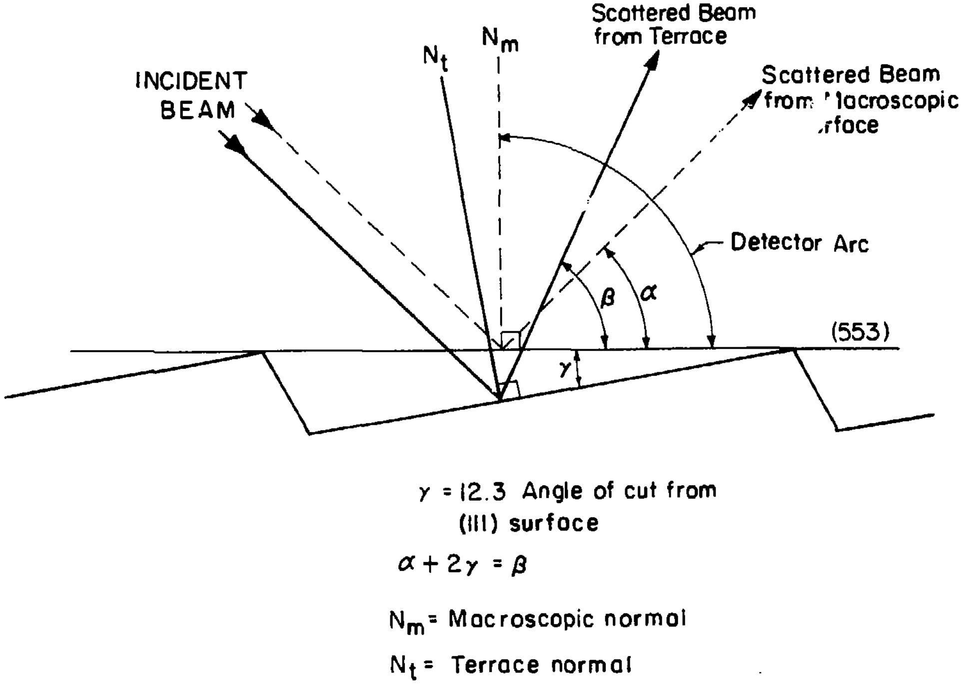

XBL 759-7323 A

Fig. 7. Diagram indicating microscopic specularity for step edges perpendicular to the incident beam.

step edge, i.e., the surface appears smooth to the incoming helium atom. These results are in agreement with the diffractive studies of helium scattering from W(112).[16] In that case, diffraction is only observed as the rows of troughs and ridges are oriented in a perpendicular *direction to the incoming beam.*

The maximum peak intensity near the macroscopic specular angle is much less than the intensity of the peak in the scattering distribution that is shifted toward the surface normal. This is partially due to a shadowing effect of the step edge on the step inflection point of the potential. The maximum shifted toward the surface normal is of course due to the scattering from the inflection point of the potential on the terrace. Figure 8 illustrates the maximum and minimum scattering angles from the step and terrace inflection points, *respectively. The large ratio of intensity scattered from the terrace* to the intensity scattered from the step is also due to the greater length (5 atoms) of the terrace relative to the length of the step (1 atom). That is, the flatter portion of the terrace potential is larger than that of the step which leads to more trajectories that scatter approximately at the rainbow angle.

The variation of the angle incidence, θ_i, for a fixed orientation of the steps of the (553) surface to the incoming beam, i.e., fixed azimuthal angle ϕ, also indicates the double peaked scattering distribution *as the result of rainbow scattering. For greater angles of incidence as* measured from the surface normal, the surface appears smoother and

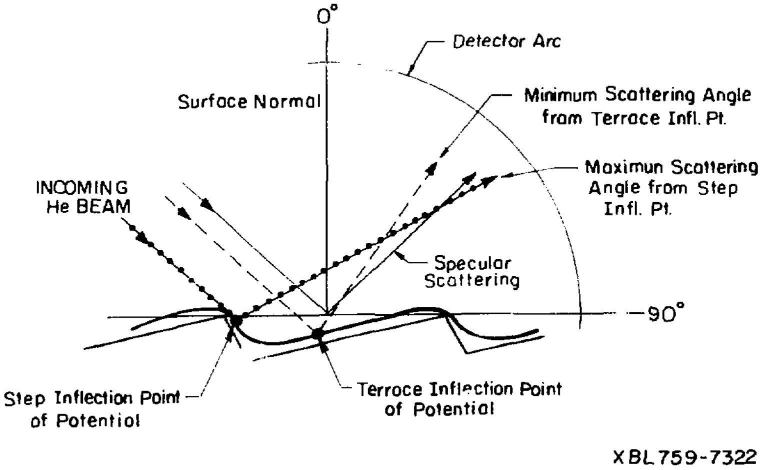

Fig. 8. Diagram qualitatively showing the origin of the two rainbow peaks. Scattering from the step inflection point leads to a scattered intensity at a maximum angle from macroscopic surface normal. Scattering from terrace inflection point leads to a scattered intensity at a minimum angle from the macroscopic surface normal.

However, [illegible] smaller angle [illegible] than incidence [illegible] surface normal, the helium atom sees the full strength of the surface periodicity and the two rainbow peaks separate. If scattering were from a purely repulsive hard wall, the two rainbow peaks should not move with respect to each other. The fact that they do move indicates the importance of the attractive part of the potential.

The increase in intensities of the surface rainbows for an increase in the angle of incidence qualitatively follows the trend predicted in calculations by McClure[illegible] for classical scattering of helium atoms. At grazing angles of incidence the surface appears less spatially rough and, thus, allows a more intense elastic scattering distribution. At more normal angles of incidence the elastic scattering distribution is less intense due to an increase in spatial roughening of the surface as seen by the helium atom. Also, there is a preferential transfer of normal momentum between the helium atom and the surface. At glancing incidence, the normal component of momentum is smaller and thus there is less chance for inelasticity.

A platinum(111) surface exhibits only specular scattering.[17] The fact that rainbow scattering has been observed from a platinum stepped surface is indicative of a strong periodic potential introduced by the steps which is seen clearly only when this periodicity lies in a perpendicular direction to the incoming particle.

Garcia and Cabrera have recently performed a quantum mechanical calculation employing a hard wall sawtooth surface under the present experimental conditions.[18] Their calculated diffraction intensities reproduce somewhat the rainbow peak as a result of scattering from the terrace but fail to fit the second rainbow peak. The sawtooth surface model probably overestimates the slope of the step with respect to the terrace and thus even at 35° angle of incidence the step is still hidden from the incident beam.

Diffraction features under these experimental conditions are not expected to be observed. The Maxwellian velocity distribution of the incoming beam makes the coherence width of the beam small (30 Å). The acceptance angle of the detector is about 5°. The diffraction peaks from a (553) surface are separated by about 5°. The surface temperature is high leading to large inelastic effects which mask the diffraction features. Thus, under proper experimental conditions, diffraction from a stepped surface should be observable. A more recent experiment employing a monoenergetic incident beam and a small acceptance angle of the detector has yielded well-defined diffraction peaks from a Cu(117) stepped surface.[19]

E. References

1. G. Boato, P. Cantini, L. Mattera, Surf. Sci. 55, 141 (1976).
2. D. E. Houston, D. R. Frankl, Phys. Rev. Lett. 31, 298 (1973).
3. J. A. Meyers, D. R. Frankl, Surf. Sci. 51, 61 (1974).
4. G. Boato, P. Cantini, U. Garibaldi, A. C. Levi, L. Mattera, R. Spadacini, G. E. Tommei, J. Phys. C 6, L394 (1973).
5. D. Wood, B. F. Mason B. R. Williams, J. Chem. Phys. 61, 1435 (1974).
6. H. Wilsch, H. U. Finzel, H. Frank, H. Hoinkes, H. Nahr, H. Luschka, H. Wonka, Surf. Sci. 49, 577 (1975).
7. H. Hoinkes, H. Nahr, H. Wilsch, Surf. Sci. 30, 363 (1972).
8. R. Chappell, D. O. Hayward, J. Vac. Sci. Tech. 9, 1052 (1972).
9. D. O. Hayward, M. R. Walters, Proc. 2nd Int. Conf. Solid Surf., Kyoto, Japan, 1974, J. Appl. Phys. Suppl. 2, Pt. 2, pp 563-66.
10. G. Boato, P. Cantini, R. Tatarek, J. Phys. F 6, L237 (1976).
11. J. M. Horne, D. R. Miller, Surf. Sci. 66, 365 (1977).
12. S. T. Ceyer, R. J. Gale, S. L. Bernasek and G. A. Somorjai, J. Chem. Phys. 64, 1934 (1976).
13. J. D. McClure, J. Chem. Phys. 52, 2712 (1970); 57, 2810 (1972).
14. S. L. Bernasek, Ph.D. Thesis, University of California, Berkeley, 1975.
15. S. L. Bernasek and G. A. Somorjai, J. Chem. Phys. 62, 3149 (1975).
16. D. V. Tendulkar and R. E. Stickney, Surf. Sci. 27, 516 (1971).
17. S. L. Bernasek, G. A. Somorjai and R. P. Merrill, J. Vac. Sci. Tech. 12, 655 (1975).

18. N. Garcia and N. Cabrera, 3rd Int. Conf. Solid Surf., Vienna, September 12-16, 1977.

19. J. Lapujoulade and Y. Lejay, Surf. Sci. 69, 354 (1977).

IV. DESIGN OF A MOLECULAR BEAM SURFACE SCATTERING APPARATUS

A. Introduction

In the last four years, significant progress has been made in understanding the structure of atomic and simple molecular adsorbates on a variety of single crystal metal surfaces. This has mainly been due to the continued and new development, as well as the combination of, several techniques. Advances in the computational facility of electron surface multiple scattering calculations have enhanced the structural information (relative atomic positions) attainable by low energy electron diffraction (LEED).[1] The combination of LEED and electron energy loss spectroscopy (EELS),[2] which yields directly the vibrational frequencies of surface adsorbates, can and has provided definitive information on the orientation of a molecule adsorbed on a surface.[3] The combination of yet another technique, ion angular distributions following electron stimulated desorption (ESDIAD)[4] with both EELS and LEED promises further definitive structural information. Helium beam diffraction has been shown to successfully provide structural information especially in cases where the LEED sensitivity is small for the adsorbate.[5] Ultraviolet and x-ray photoelectron spectroscopy (UPS, XPS)[6] has successfully measured binding energies for the emitted electrons for surface adsorbates and recently, diffraction of the backscattered photoelectrons has been observed.[7] The interpretation of a photoelectron spectrum is presently being facilitated by the scattering of He metastables which are sensitive only to the outermost layer.[8]

The progress, however, in understanding the dynamics of the initial collision of these adsorbates with the surface or of their subsequent reaction with themselves, another adsorbate or the surface has not proceeded very rapidly. Thermal desorption experiments can correctly identify reaction products when the reactants are initially completely equilibrated with the surface, can yield average quantities for binding energies of an adsorbate at various sites and can yield average quantities for kinetic data. However, interesting questions such as how do the translational and internal energy and the orientation of a molecule affect its ability to exchange energy, bind or dissociate on a surface, what are the energetics and intermediates along the reaction coordinate, what is the time scale of the reaction and what happens to the energy liberated in an exothermic reaction are questions not readily answerable by thermal desorption experiments.

Questions of the first type essentially require a single collision of a molecule which has a well-defined initial kinetic and internal energy and direction with a surface as in a beam-surface scattering experiment and some way to determine whether the molecule has just undergone an inelastic event with the surface or whether it has been trapped in the surface-adsorbate well. The angular distribution in conjunction with a velocity distribution of the scattered molecules can yield this information.[9] Knowledge of the energetics along the reaction coordinate and the fate of the exoergicity of a reaction can also be obtained from a velocity distribution measurement. For example, the three existing velocity distribution measurements for reactive systems (H_2 desorbing from Ni[10,11] after recombination of adsorbed H atoms and CO_2 formed by reaction of CO and O_2 on Pt[12]) indicate that there is a substantial exit channel barrier for both H_2 and CO_2 desorption in the normal direction since the kinetic energy of the H_2 and CO_2 is substantially faster than that which would be predicted from assuming that the products were in equilibrium with the surface. It is also clear from the velocity distribution measurements as a function of angle that a one-dimensional barrier model does not fit the observed data and that very interesting dynamical effects are occuring here.

A molecular beam gas-surface scattering apparatus is particularly well suited for studying the dynamics of a gas-surface reaction by observing the product angular and velocity distribution. The collimation characteristics of the beam allows the reactants, atoms, molecules or radicals, to hit with a well defined angle a small area of the surface under study so that the product signal detected does originate from this surface. Differential pumping of the beam source allows the pressure of the beam at the surface to be high (10^{-5} torr) while the ambient pressure is three or four orders of magnitude lower. The main drawback of this technique is the low signal level intensity of the products due to low reaction probabilities (<1%) and a long flight path (6") between the surface under study and the detector required to obtain a reasonable velocity distribution (8%) with a time of flight technique. This drawback is partly eliminated by differentially pumping the detector which reduces the background intensity to be between 1-10 times larger than the signal. Without differential pumping, the background at the detector could easily be 10^5 times the signal intensity. In addition, modulation of the beams allows unambiguous subtraction of the DC background from the total signal measured. This chapter describes the design, construction and operation of a beam surface scattering apparatus which can help advance the knowledge of surface dynamics as rapidly as the knowledge of surface structure has recently advanced.

A schematic diagram is shown in Fig. 1. The apparatus consists of seven independently pumped chambers. The largest is the main scattering chamber in which the crystal surface under study is mounted on the axis. The background pressure in this chamber is 3×10^{-10} torr so that clean surface experiments can be performed. The crystal surface is mounted on a manipulator to provide movement of it under vacuum. The four chambers associated with the beam production are welded as a unit into the main chamber. The two beams intersect at the center of the main chamber where the surface is mounted. A quadrupole mass spectrometer is employed as a detector. The chamber which houses the detector and its differential chamber is referred to as one chamber, the detector chamber. The detector chamber is housed entirely inside of the main scattering chamber and rotates with respect to it with the crystal at the center of rotation. A motor with a chopper blade is mounted on the detector chamber, modulating the beam as it enters the chamber.

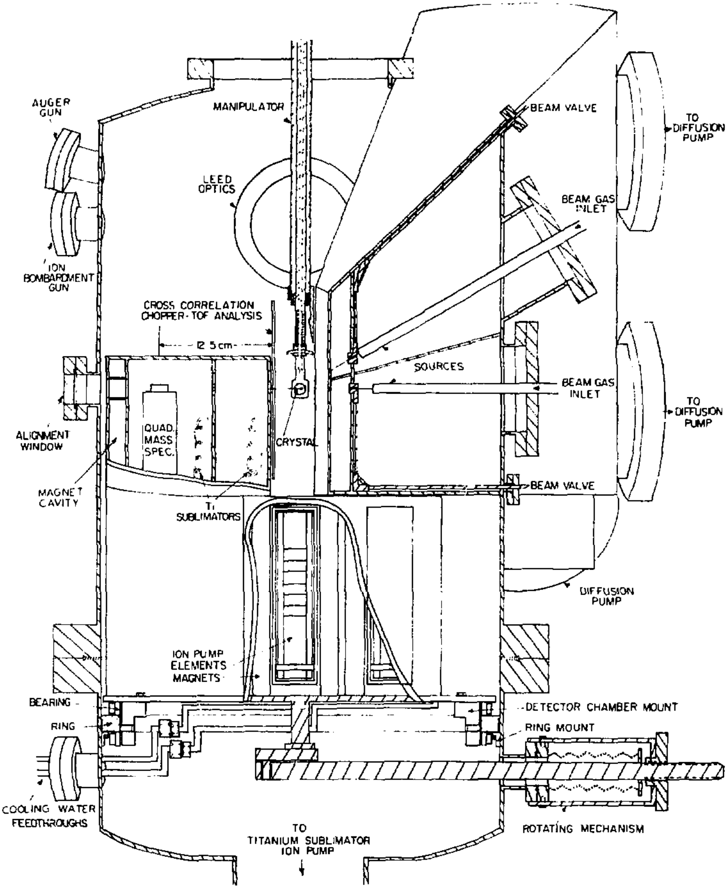

XBL 799-11376

Fig. 1. Schematic assembly drawing.

In this fashion, angular distributions and velocity distributions as a function of angle of the products from a surface chemical reaction can be measured.

Sections B-K detail the various parts of the apparatus. Section L discusses the signal intensities expected and measured. Chapter V presents some of the first data.

B. Source and Source Buffer Chambers

1. Construction

The apparatus can accommodate two independent beam sources. The two source and two buffer chambers were constructed out of 0.125" 304 stainless steel pieces of sheet metal. The individual walls are labeled A-K in Figures 2 and 3. On wall B, two 0.500" holes, counterbored with 0.625" holes 0.019" deep, were drilled through the sheet metal at the calculated positions for the beam to pass from the source chamber into the buffer chamber. These 0.500" holes are to accommodate the beam valves described in Section B.4 which isolate the source chamber from the buffer chamber and the UHV main chamber. On wall A, two countersunk clearance holes for 4^{40} screws and a 0.125" hole are drilled for mounting a motor in the primary source buffer chamber. Holes 1.5" in diameter were machined in wall H to accommodate two 2.75" OD conflat flanges for ionization gauges in each of the source chambers. Holes 8" in diameter were machined in walls I and J to accommodate 11" ASA flanges which ultimately mount the diffusion pumps. Two 6" holes and three 1.5" holes were machined in wall G to accommodate 8" and 2.75" OD conflat flanges to mount the diffusion pumps and to provide ports for roughing, ionization gauges and in the primary source buffer chamber a feedthrough for coolant for the chopper motor and electrical feedthroughs.

The walls were then bent into the correct configuration for welding. Walls D, E and F were bent into a cone configuration. Thus the

Fig. 2. View of source and source buffer chambers with wall H, part of wall A and main chamber removed. Small dotted lines indicate path of beams. (A) Primary wall. (B) Source-buffer chamber dividing wall. (C) Source chamber bottom plate. (D) Top plate. (E) Primary-secondary source chamber dividing wall. (F) Primary and secondary buffer chamber dividing wall. (G) Buffer chamber walls. (I) Primary source chamber back plate. (J) Secondary source chamber back plate. (K) Buffer chamber bottom plate. (L) Secondary source diffusion pump flange. (M) Primary source diffusion pump flange. (N) Primary buffer diffusion pump flange. (O) Secondary buffer diffusion pump flange. (P) Electrical feedthrough. (Q) Roughing port. (R) Ion gauge. (S) Blank 2.75" OD flange. (T) Ion gauge. (U) Roughing port secondary buffer chamber.

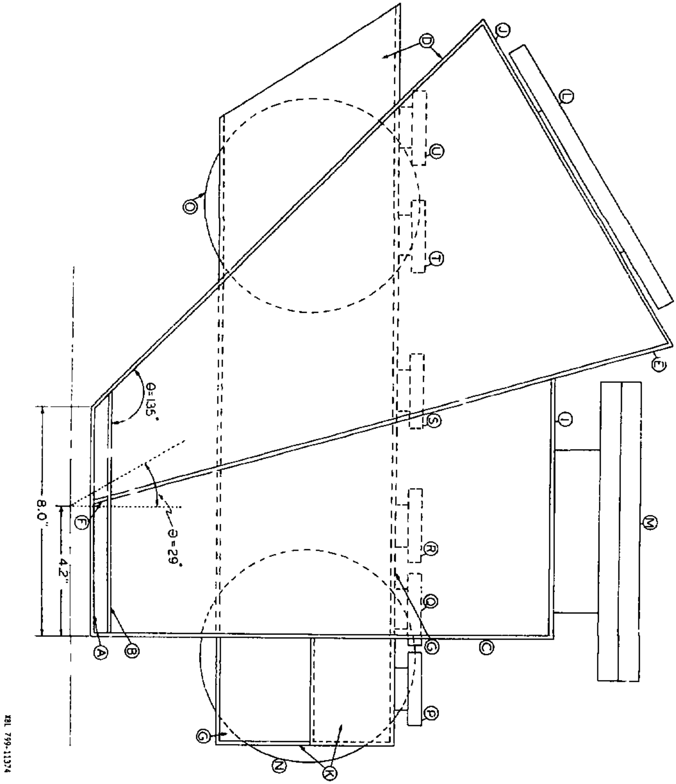

Fig. 2

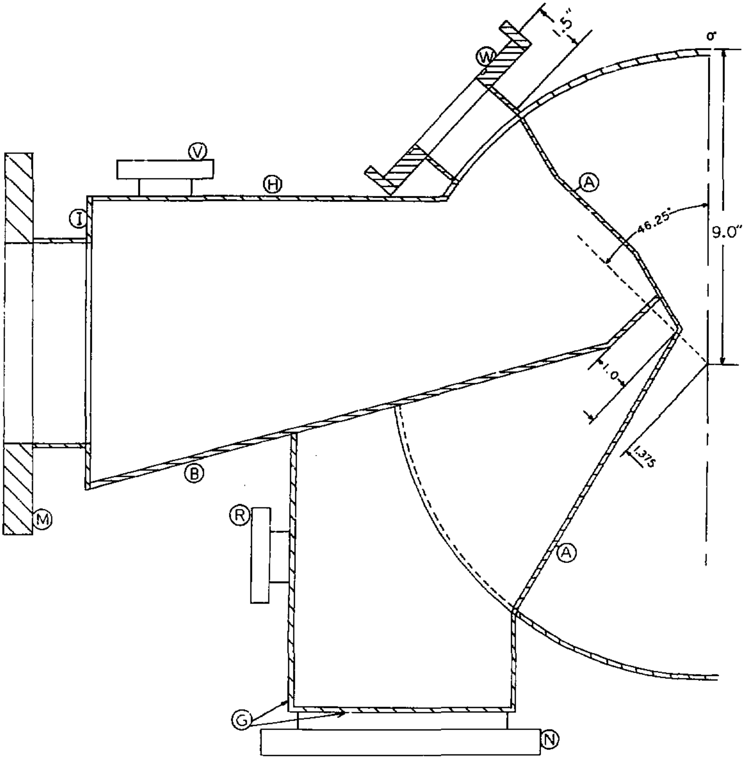

XBL 799-11602

Fig. 3. Cross section through primary beam line. Labels are the same as previous figure. (H) Side wall. (V) Ion gauge primary source. (W) Source flange.

lengths of walls A, B, G, and I are determined by their intercept with the surface of the cone centered on the major axis of the main chamber at a 45° angle to the large 22" flange. This geometry was necessary so that the LEED screen could be viewed over the source chamber thus preventing the main chamber from being unduly long. This source and source buffer chamber geometry also allows the closest packing of four 6" diffusion pumps to achieve maximum pumping speed and the closest placement of the two sources to the crystal surface. The source chambers can also accommodate 10" diffusion pumps.

The source and source buffer chambers were welded together as a unit, leak checked and then welded into the main chamber. The main scattering chamber had the holes for the source chamber unit and for the main chamber flanges already machined into it at this time. The welds were performed on the more stringent vacuum side. The flanges indicated in Figs. 2 and 3 were then welded on the source and source buffer chambers with reference to a arbitrarily chosen 0° mark on the 22" flange. Since no machining of the flanges was carried out after welding positions of the source and buffer chamber flanges can not be used as references.

2. Beam Source Flanges

The beam source flanges are rectangular with an useable opening of 4" x 2.25". The rectangular O-ring groove receives a 16" OD, 0.187" wall O-ring. There are ledges bolted onto the sides of the flanges so that 1/4[28] screws can be held to push or pull the mating beam source flanges. The available travel in each of two dimensions is ± 0.25" with the appropriate screws and nuts mounted in place.

3. Beam Holes

The beam holes in the main chamber/buffer chamber wall A and in the seat of the beam valves were drilled with reference to the 22" flange after the flange had been remachined flat and round to within 0.001". The primary beam hole in all A was drilled parallel to the 22" flange and at the center of the 0.500" hole in wall B. The hole makes an angle of 46.25° ± 0.25° with the 0° mark on the 22" flange. With the same setting the beam hole in wall B was drilled after installing the seat of the beam valve. The secondary source beam holes were drilled with the same procedure at 29.0° ± 0.25° with respect to the primary beam line.

A 1 mm drill was employed to drill all four beam holes. In the secondary chambers the walls make approximately a 30° angle to the beam line with reference to the 22" flange. Thus, the holes in the secondary chamber walls are elliptical in shape where the penumbra is 1.15 mm in length and the umbra is 1.0 mm.

4. Beam Hole Valves

The beam hole valves are shown in cross section in Fig. 4. The seat of the beam valve has a groove milled into it which accepts a 0.563" OD, 0.468" ID O-ring fashioned from a 0.063" thick sheet of viton. This O-ring is the seal between the source and the source buffer chambers. The seat of the valve fits into a key in wall B

Fig. 4. Cross section through plane of primary and secondary beams showing beam valves. Dotted lines indicate path of beam. (A) Beam valve seat. (B) Wedged track. (C) Linkage blocks. (D) Lever. (E) Valve stem. (F) Slide arm. (G) Brass bellows.

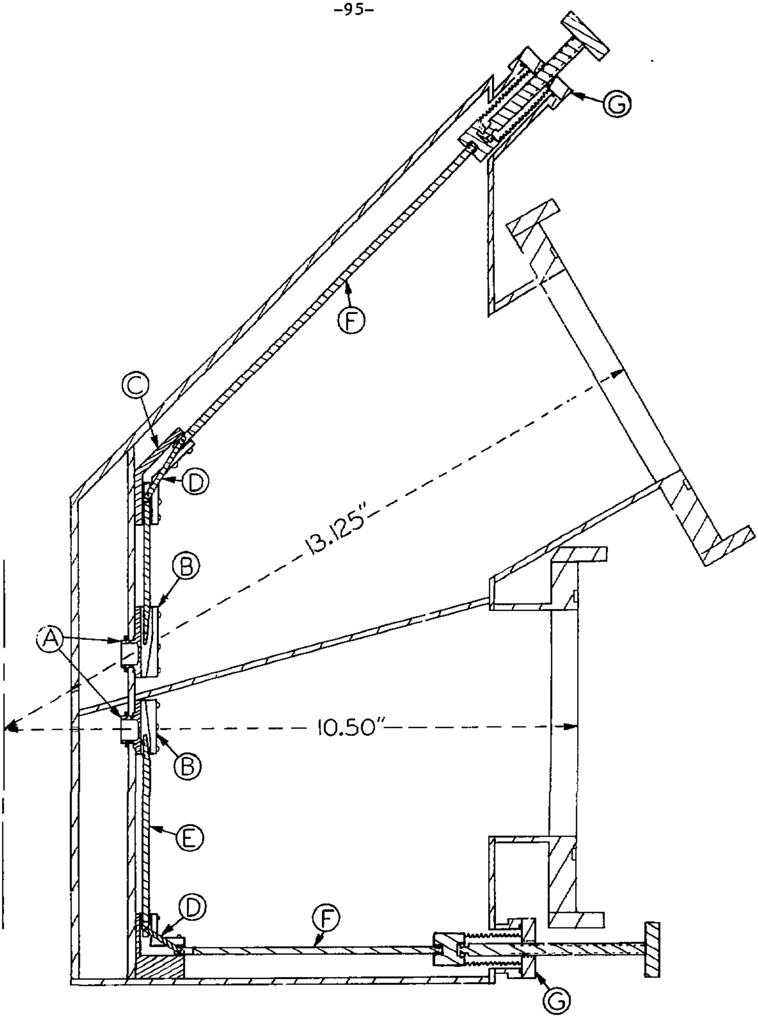

XBL 799-11678

Fig. 4

and is fastened in place with a $1/2^{27}$ nut in the buffer chamber. Thus, the diffusion pumps on the buffer chambers have to be removed in order to insert or remove the seats of the beam valves. The seals over the beam holes are made by wedging a slide arm which holds a 0.313" OD, 0.063" wall O-ring against two sloping tracks attached by 0^{80} screws to the beam valve seat. A pressure of 7×10^{-9} torr can be maintained in the buffer chambers after bakeout of the main chamber with the source chambers at atmospheric pressure. The 0.5" of translation required to operate the valve is accomplished by a linear motion O-ring sealed brass bellows feedthrough and transferred through a 90° or a 135° linkage. The bellows and flange are part of a brass bellows vacuum valve. The linkage blocks were tack-welded into place after the insertion of the source and source buffer chambers into the main chamber so as to be correctly positioned with respect to the bellows feedthrough. The motion transfer is accomplished by loose fits of a lever on 0.063" dowel pins press fit into the ends of the slide arm and the valve stem. The slide arm, valve stem and lever have to be assembled prior to insertion into the beam valve seat, linkage block and the brass bellows linear motion feedthroughs.

5. Pumping

Both source chambers are pumped by a 6" NRC type HS-0162 1500 watt 120 V diffusion pump rated at 1500 l/sec, trapped by a Varian type 0362 6" LN_2 trap with a conductance of 2000 l/sec and isolated from the source chamber via Airco Temescal Series 2500, Style 30 pneumatically actuated aluminum right angle valves. The primary source diffusion pumped is backed by a Kinney KDH 130 cfm mechanical pump and the secondary source diffusion pump is backed a Welch 1375 35.4 cfm mechanical pump. The buffer chambers are pumped by Varian VHS-6 2200 watts, 208 V diffusion pumps rated at 2400 l/sec, trapped by Varian type 0362 6" LN_2 traps and isolated from the chamber by Huntington 6" gate valves. The primary and secondary buffer diffusion pumps are backed by the respective mechanical pumps which back the source chamber.

C. Main Chamber

1. Construction

A commerical 18" OD Ultek belljar with a 0.187" wall was employed as the main scattering chamber. One half of the original bell jar was extended to its final length of 27.25" as measured from the 10" manipulator flange to the 22" flange. The other half remains at its original length of 21.25" as measured from the 22" to the 6" flange which accommodates the poppet valve over the titanium sublimator and ion pump. Including the length of the manipulator and the poppet valve the machine is 103.5 ± 1" long. An additional clearance of a minimum of 19" is required to separate the two halves of the belljar so as to remove the detector chamber. An additional minimum clearance of 15" is required to remove the manipulator. A minimum of

9" clearance is required to remove the poppet valve. The effective length of the chamber is then 146.5 ± 1". The height of the room in which the apparatus was to be installed is 136.75 ± 0.5" from the floor to the ceiling and 128.75 ± 0.5" from the floor to the overhead room lights. Thus, the longest axis of the apparatus was placed parallel to the floor.

All holes into which the flanges are welded were machined within 0.25° of a given angle with reference to the 0° mark on the 22" flange. The flanges were first tack-welded into place before the final welding was performed in an attempt to make the plane of the flange perpendicular to a radius of the 18" belljar. There are two mini-conflat flanges whose planes are not perpendicular to a radius but whose planes are parallel to each other. A line perpendicular to the plane of these flanges intersects a radius of the 18" chamber about 1" from the center. The 10" flange on which the manipulator is mounted was placed parallel to the 22" flange and approximately at the center of the 18" belljar. Since no machining of any flange on the main chamber was performed after welding except for the 22" flange, only the 22" flange can be used as a reference surface.

2. Schematic

There are two levels of the main scattering chamber on which the flanges are welded. The level closest to the manipulator accommodates most of the flanges for the analytical techniques: the Varian retarding gird optics and electron gun, the glancing electron gun for Auger Electron Spectroscopy oriented 75° away from the retarding grid optics, the ion bombardment gun, and the window for viewing the phosphorescent LEED screen. Also on this level is a 8" OD flange which holds a window and a 10" flange on which a diffusion pump is mounted. A cross section of this level of the main chamber is shown in Fig. 5. The second level the cross section of which is shown in Fig. 6 is the scattering level which has three flanges for windows to view the crystal, the two mini-conflat flanges which do not point on a radius, ionization gauge flange, and a mini-conflat flange to view the laser beam aligned through the primary source. At a third level closest to the 22" flange there is also a flange for a window in line of sight of the secondary source beam line and a blank 8" OD flange mainly for access.

The movable part of the belljar has seventeen 2.75" OD flanges eight of which were original in the commerical belljar. Eleven of these flanges accommodate feedthroughs which provide the electrical power and the cooling facilities to the detector chamber. The additional flanges were welded into the belljar on one side so that the electrical cables could be conveniently grouped. One of the flanges accommodates the rotating drive mechanism which is described in Section E.4. Another one serves as a roughing and vent port through a metal sealed right angle Varian valve. The commerical belljar has a T welded to its end which has two 8" OD flanges and a a 6" OD flange welded to it. A titanium sublimator and ion pump

Fig. 5. Assembly cross section of main chamber through LEED level, view towards manipulator. (A) Secondary source flange. (B) Window. (C) Blank flange. (D) Ion gun. (E) Auger gun. (F) LEED optics. (G) Secondary source chamber. (H) Buffer chamber. (I) LN_2 trap. (J) Gate valve. (K) Diffusion pump. (L) Right angle pneumatic valve.

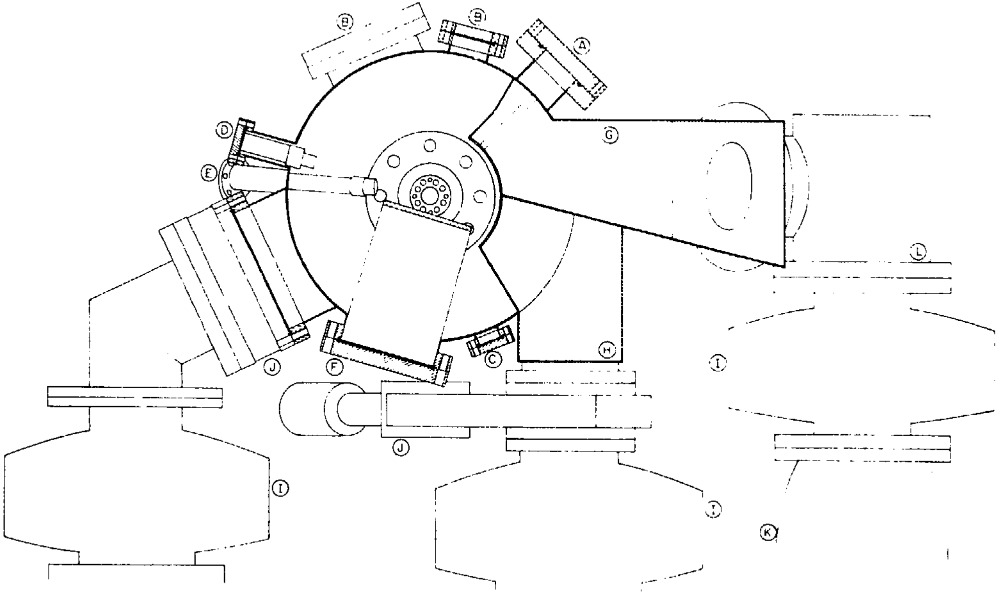

Fig. 5

XBL 799-7017

Fig. 6. Assembly cross section through scattering level towards poppet valve. (A) Primary source flange. (B) Window. (C) Blank flange. (D) Ion gauge. (E) Chopper motor cooling block. (F) Ring. (G) Mass spectrometer. (H) Motor water cooling lines. (I) Primary source chamber. (J) Primary buffer chamber. (K) Ion gauge, roughing port. (L) Right angle pneumatic valve (M) LN trap. (N) Gate valve. (O) Detector chamber. (P) Bearing mounting block. (Q) Main chamber ion pump. (R) Main chamber titanium sublimator. (S) Rotation drive mechanism. (T) Diffusion pump.

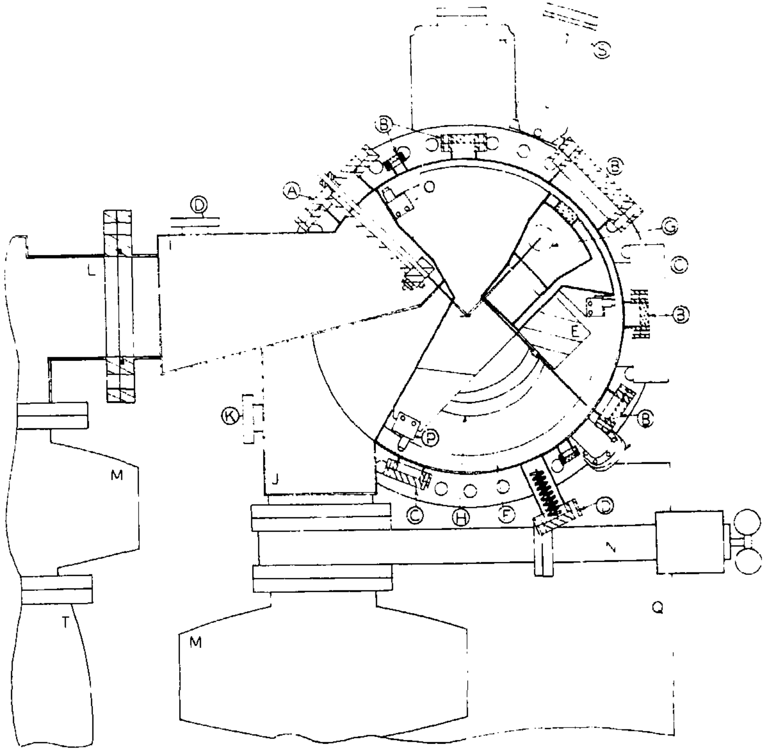

XBL 799-11679

Fig. 6

are bolted to the 8" OD flanges. The 6" flange holds a poppet valve to isolate the sublimator and ion pump from the main chamber. This bellows valve translates seven inches from its retracted position clearing the titanium sublimator and ion pump ports to its closed position which abuts against a metal ring welded into the tee which holds a viton O-ring. Thus, the sealing plate of the valve cannot be removed from the chamber without removing the welded ring in the tee. Also, the valve drive mechanism cannot be removed from the chamber without gaining access through one of the 8" OD flanges to remove the spring ring which joins the drive mechanism to the sealing plate. Note that there is a right-handed thread in the drive mechanism so that a clockwise motion shortens the drive rod thus opening the valve.

The 22" wire seal flange requires a Ultek copper wire gasket (268-9189). The plane of the 22" flange on the longer part of the belljar and thus the axis of the machine slopes toward the manipulator by about 0.2°. The line between the 0° mark and the 180° mark on the 22" flange is also not perpendicular to the floor with the machine being rotated toward the source chamber by 2 or 3°.

3. Pumping

The main chamber is pumped by a Varian VHS-6, 2200 watts, 208 V, 2400 l/sec diffusion pump which is trapped by a Varian type 0362 6" LN_2 trap and isolated from the chamber by a Huntington 10" metal sealed bonnet gate valve. A 400 l/sec Varian noble ion pump and a

Ultek 214-0400 titanium sublimator with a total H_2O cooled pumping surface of 150 sq. in. also are provided as pumping for the main chamber.

After bakeout (accomplished with heating tapes wrapped around the chamber) at 200°C for 72 hours the pressure in the main chamber is 3×10^{-10} torr with the diffusion pump and ion pump operational. The pressures rises to 8×10^{-10} torr with only the ion pump operational.

D. Detector Chamber

The physical shape and size of the detector chamber were dictated by the dimensions of the Ultek belljar employed as the scattering chamber. The detector has to be differentially pumped and had to rotate a minimum of 135° around the center of the main chamber in a plane parallel to the 22" flange. The distance between the center of rotation and the mass spectrometer detector itself had to be a minimum of 6" in order to obtain a velocity resolution of 8%. A requirement that the belljar geometry not be extensively modified dictated that ion pumps had to be totally enclosed inside the main scattering chamber. Since the magnets of the ion pumps are incompatible with ultra high vacuum, the detector chamber is double walled with the outer compartment at atmospheric pressure containing the magnets and poles of the ion pumps. Since the titanium sublimators pump more efficiently on a cooled surface, cooling water is circulated through the outer compartment. Since the source chamber unit sticks into the main chamber, the detector chamber is at two levels: one level at which the ionizer of the quadrupole is mounted in line with the primary source and another level which contains the ion pump. Thus the ion pumps can pass to the side of the primary source and buffer chambers so that the scattered beam can be detected at a 22.5° angle from the incident beam.

1. Construction

Since the detector chamber will undergo temperature cycling and since the chambers are difficult to access and view in the completed condition, the construction and welding sequence of the detector chamber will be detailed.

A 0.375" stainless steel 304 plate was initially machined to the correct configuration forming the bottom plate of the detector chamber. Using a 0.75" diameter hole in the center of the bottom plate as a reference, the six 0.313" diameter mounting holes for the bearing blocks were drilled precisely on a radius on the bottom plate. This operation should have been done after welding of the entire chamber. All of the detector chamber walls are 0.125" thick. The walls are labeled in Figs. 7 and 8.

The pump pockets front wall was welded on the inside to the 8 pump pocket side walls. This assembly of 9 walls was welded on the inside to the bottom plate. The inner wall I and the mass spectrometer insert can not shown in Fig. 8 were welded to the bottom plate. The inner wall I was welded to the pump front wall on the inside. The pump top plate was welded to the pump front wall and the inner wall I. Inner wall II was welded to the pump top plate and inner wall I on the outside. The top lid was welded to inner wall I and II on the inside. The dividing wall was welded to the bottom plate, pump front wall, pump top plate, and inner walls I and II all on the quadrupole side. The inner back wall was welded to the bottom plate, pump top plate, top lid, inner walls I and II, the mass spectrometer insert can and the pump front wall all on the inside. Five, 0.375" long pieces of 0.25" tubing were welded to the

Fig. 7. View of detector chamber with top most lid removed and no pumps installed. (A) Buffer chamber pump pocket for elements. (B) Quadrupole chamber pump pocket. (C) Magnet cavity. (D) Coolant feedthrough. (E) Mass spectrometer flange. (F) Titanium sublimator flange. (1) Pump back wall. (2) Pump pockets front wall. (3) Pump pockets side walls. (4) Outer back wall. (5) Inner back wall. (6) Pump front wall. (7) Dividing wall. (8) Inner wall II. (9) Inner Wall I. (10) Outer wall. (11) Window tube. (12) Bottom plate. (13) Insert.

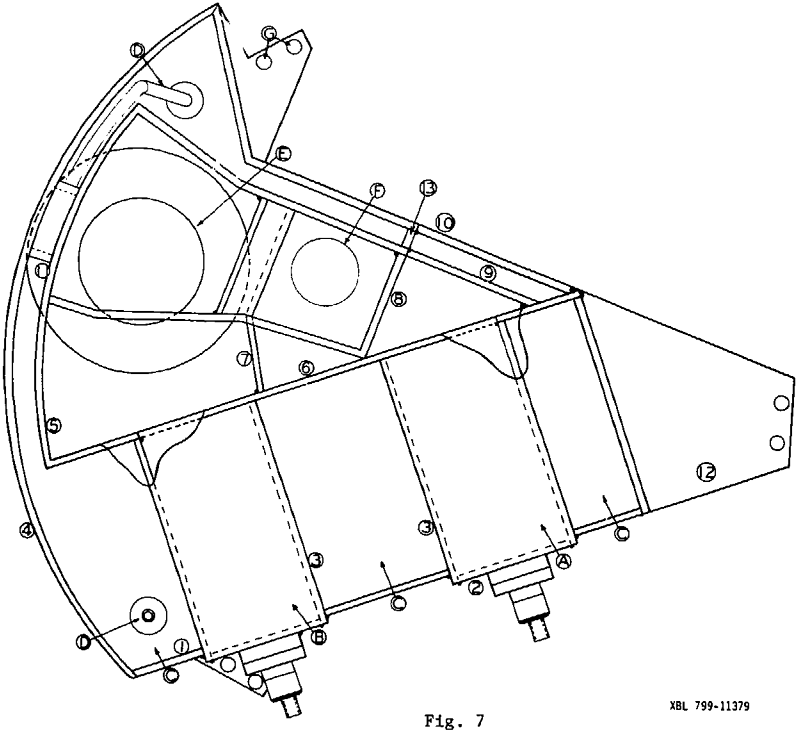

Fig. 7

XBL 799-11379

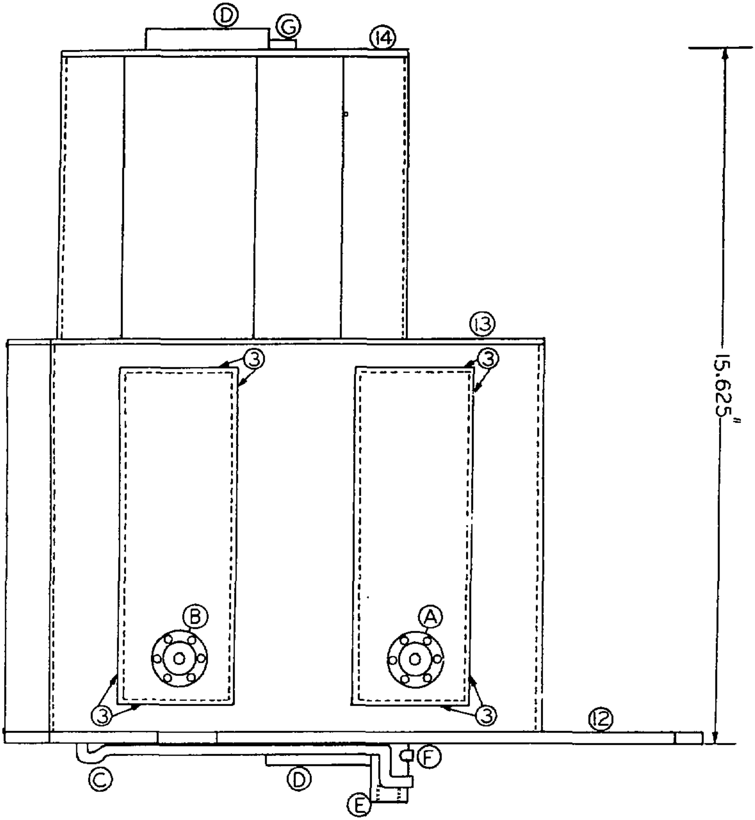

Fig. 8. View of detector chamber from ion pumps. (A) Buffer chamber ion pump feedthrough. (B) Quadrupole chamber ion pump feedthrough. (C) Coolant feedthrough outlet. (D) Titanium sublimator flange. (E) Stud at center of chamber. (F) Coolant inlet. (G) Magnet cavity access flange. (3) Pump pockets side walls. (12) Bottom plate. (13) Intermediate lid. (14) Top lid.

inner wall I and the outer wall to provide support for this flat, large area, thin wall against atmospheric pressure. Welding of the outer wall and the outer back wall to each other and to the top lid, pump top plate, and insert, were performed on the outside. A short piece of 1.5" OD tubing was welded between the inner back wall and the outer back wall on the outside to provide an opening along the beam line for a window. A mini-conflat flange was then welded from the inside on the inner back wall. The titanium sublimator flanges were welded to the detector chamber at this time.

At points where the inside and outside welds were joined (top plate to inner walls I, II and inner back wall, inner back wall to pump front wall, inner wall I to pump top plate and inner wall II), a penetrating weld was made on one side and then picked up on the other side by burning away material and then refilling the weld with stainless steel welding rod. All welds were checked for leaks at appropriate stages in the construction. The entire chamber, buffer, quadrupole, and magnet cavity chambers, are leak free on a scale of 1×10^{-10} standard cc per sec.

At this point the bottom face of the bottom plate of the chamber was machined flat to a 0.25" thickness. The beam line was defined to pass through the center of the chamber and across the center of the mass spectrometer flange. Its position is approximately at the center of the 0.75" opening of the miniconflat flange and parallel to the bottom plate of the chamber. A hole in the dividing wall was drilled and reamed to a 0.500". With the same setting a number 53 center drill (0.0595") was employed to create the beam entrance hole in the inner wall II. The wall was then ground down around the hole leaving the channel portion of the hole to be about 0.01" long. A 0.500" OD plug with a step on it and a 0.120" hole drilled precisely into the center was press fit into the dividing wall as the second collimating slit.

The chamber was cleaned with various solvents and baked out in a vacuum furnace at 700°C for 24 hours. This procedure outgasses the H_2 from the bulk of the stainless steel.[13]

The magnets are wedged in against the bottom plate and the pump pocket side walls. The back pump wall was welded on the pump pocket side walls by temporarily placing chunks of soft iron in the pump pockets and by placing a 0.25" thick mu-metal shield over the pump back wall. The anodes of the pump elements abut against a stop tack welded to the pump front wall. The pump pocket front walls were welded to the side walls again employing a mu-metal cutout shield.

This last welding operation caused considerable warpage in the bottom plate of the detector chamber. To correct for this the beam line as determined by the beam entrance hole and the collimating slit was placed exactly parallel to the bed of an end mill by using a laser mounted parallel to the mill as a reference. The top face of the bottom plate where the bearing blocks are mounted was then machined flat and parallel to the beam line.

2. Schematic

The resultant detector chamber has a distance of 6.187 ± 0.030" from the center of rotation to the center of the mass spectrometer flange. The distance from the center to the front edge of the beam entrance hole is 1.406 ± 0.030" and from the front edge of the beam hole to the front edge of the collimating beam hole the distance is 3.187 ± 0.063". If the front edge of the time of flight beam chopper sits at 0.170" away from the front edge of the beam hole the flight path is approximately 4.9" or 12.58 cm. The distance of 0.170" is necessary for the chopper blade to clear the outside welds of the insert walls to the outer walls.

Four 10^{32} threaded rods are tack welded to the outer wall to support the chopper motor mount. The chopper motor mount will be described in detail in Section G.1.

Also tack welded to the outer walls are two screws which support a counterweight on the chamber. This counterweight is necessary to balance the weight of the magnets, so as to provide a smooth rotation for the chamber. The detector rotation will be discussed further in Section E. The counterweight is a stainless stell can which was filled up with small chunks of scrap tungsten and scrap lead. This cauldron was heated up to melt the lead thus leaving a solid mass in the can. A lid was welded to the can. This counterweight, when place in a separate UHV chamber and baked out, attained a pressure of 5×10^{-10} torr, the base pressure of the chamber.

3. Pumping

Each chamber is pumped by one triode element and magnet from a Varian (911-4053) 60 l/sec ion pump. The high voltage to the ion pumps is supplied through a mini-conflat mounted feedthrough whose stem screws into a nut which is spot welded to a flexible bridge which passes over the anode of the elements to each end of the cathode.

In addition, each chamber is pumped by a Varian Mini-Ti-Ball sublimation source with approximately 48 sq. in. and 90 sq. in. of cooled surface area available for pumping in the buffer and quadrupole chambers respectively. The present design for mounting the detector chamber accommodates water cooling.

The detector chamber is baked out by radiation from the titanium subliminators and by radiation from the main chamber walls. A temperature of 130°C has been measured on the outer wall of the detector chamber with 20 amps flowing through each of the sublimators and with the bake out tapes on the main chamber at 200°C. A bake out of 96 hours is required for the chamber to attain its utlimate pressure.

4. Cooling Water Feedthroughs

Three, 0.25" OD pieces of stainless steel tubing were welded into thin wall sleeves, welded onto a 2.75" OD flange. On the vacuum end of the tubing, Cajon fittings were welded. These attach to 0.40" OD, 0.2" ID, 8" and 9.5" long bellows whose ends are welded to the stud in the center of the chamber as shown in Fig. 8. The fill line penetrates the stud which is hollow and allows water to enter the magnet cavity chamber. The other two lines are return lines which are tack welded to the stud but which continue with rigid tubing to the two extreme positions of the magnet cavity chamber. At these two extremes, the tubing breaks into the magnet cavity chamber. The return line which breaks into the chamber underneath the quardrupole chamber magnet terminates there. The 0.25" tubing of the other return line actually continues into the magnet cavity chamber and terminates underneath the alignment window. This arrangement allows the largest volume of water to fill the chamber when the detector viewing angle is approximately 0.25° to either side of the 0° mark on the 22" flange. When the detector viewing angle is at a position between the 0° mark and the position closest to the source chamber the return line underneath the quadrupole magnet chamber should be shut off by a valve on the outside of the 2.75" OD flange feedthrough. At any other angle of the chamber the opposite arrangement of the return valves should be effected. This arrangement of two return lines is necessary to maintain a constant coolant level in the chamber to prevent pressure fluctuations.

The tubing from the feedthrough to the bellows was fitted in place prior to welding to insure that no twist on the bellows would occur and that the bellows cleared each other during rotation. Nevertheless, a spiraled teflon sleeve was put over the bellows as protection against rubbing on another surface.

5. Angular Resolution

Figure 9 indicates the geometry necessary to calculate the angular resolution of the detector. The defining holes were drilled as described in Section D.1. The distances indicated in Fig. 9 are accurate to ± 0.03". The first and second defining slits are respectively 0.060" and 0.120" in diameter. This yields an angular resolution of 1.5° or 5.3×10^{-4} sr. The cross sectional area of the beam at the ionizer is approximately 0.133 cm^2.

Figure 10 indicates the diameter of the crystal seen by the detector at the normal angle to be 0.14" For angle of incidence $\leq 57°$, the detector at the normal angle views the entire beam spot.

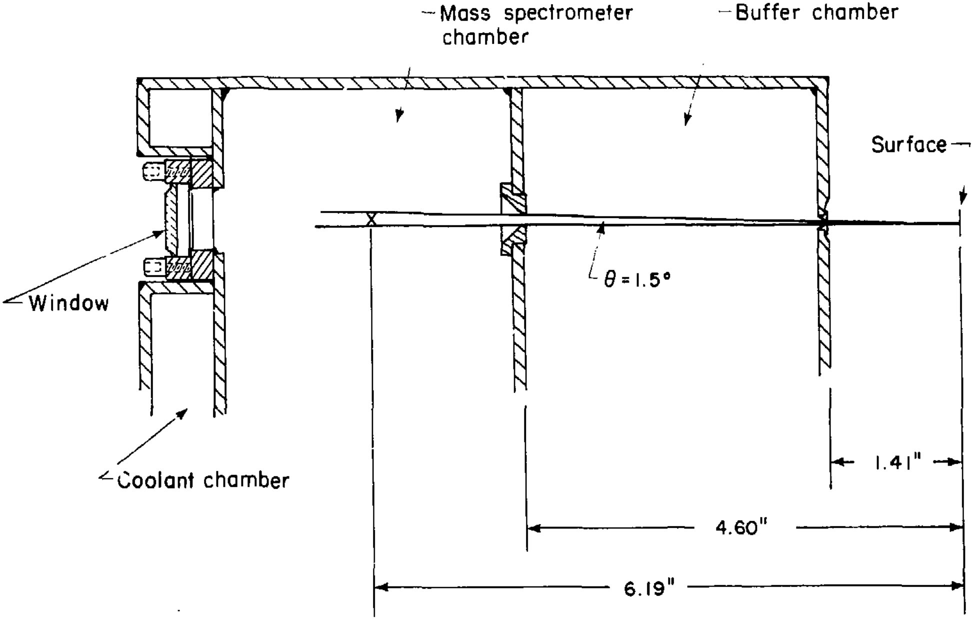

Fig. 9. Angular resolution of the detector chamber. First and second defining slits are 0.060" and 0.120" in diameter, respectively.

XBL 799-2860

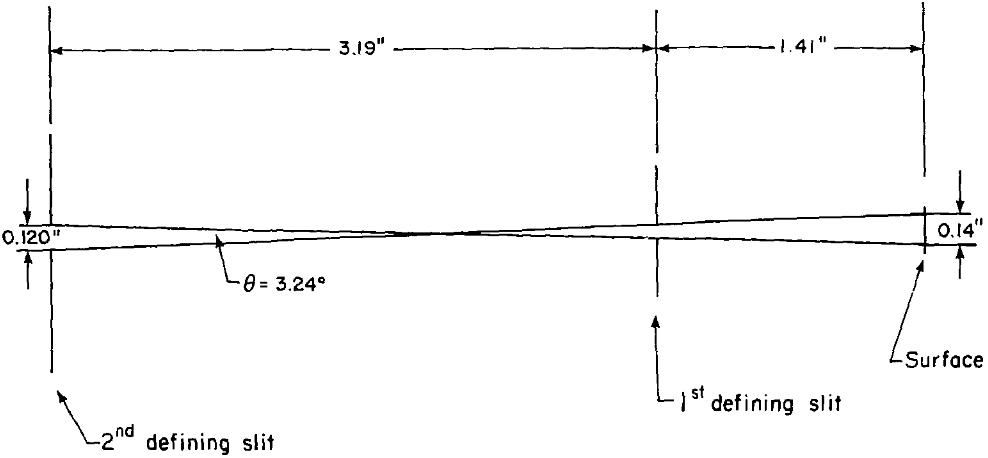

XBL799-2859

Fig. 10. Diameter of the crystal surface viewed by the detector.

E. Detector Chamber Rotation System

1. Bearing Blocks

The three bearing blocks serve two purposes: To mount the detector chamber on the ring in the main scattering chamber and to mount the bearings onto the chamber. Three Fafnir aircraft bearings are mounted on each block as shown in Fig. 11. Two bearings (0.813" OD, 0.313" bore) run on the top and bottom faces of the ring and mainly serve as the mounts and alignment for the chamber on the ring. The third bearing (0.75" OD, 0.25" bore) carries the load of the chamber and rotates on the inside diameter of the ring. In some positions this bearing carries the entire weight of the chamber, approximately 90 lbs. The load on all three bearings is essentially radial. They are lubricated with MoS_2 powder and have to be relubricated periodically.

The bearing blocks are mounted on the bottom plate of the detector chamber by two 0.313" bolts. However, in order to correct for a slight misalignment of the detector beam line (i.e, the beam line defined by the entrance hole and collimating hole do not lie on a radius of a circle defined by the bearing block mounting holes) smaller bolts in four of the six mounting holes are used so that the bearing blocks can be angled in position. This allows the beam line to be on a radius of the ring and thus the chamber rotates around one point. Shims must be wedged between the edge of the bottom plate and the bearing block to prevent movement of the block

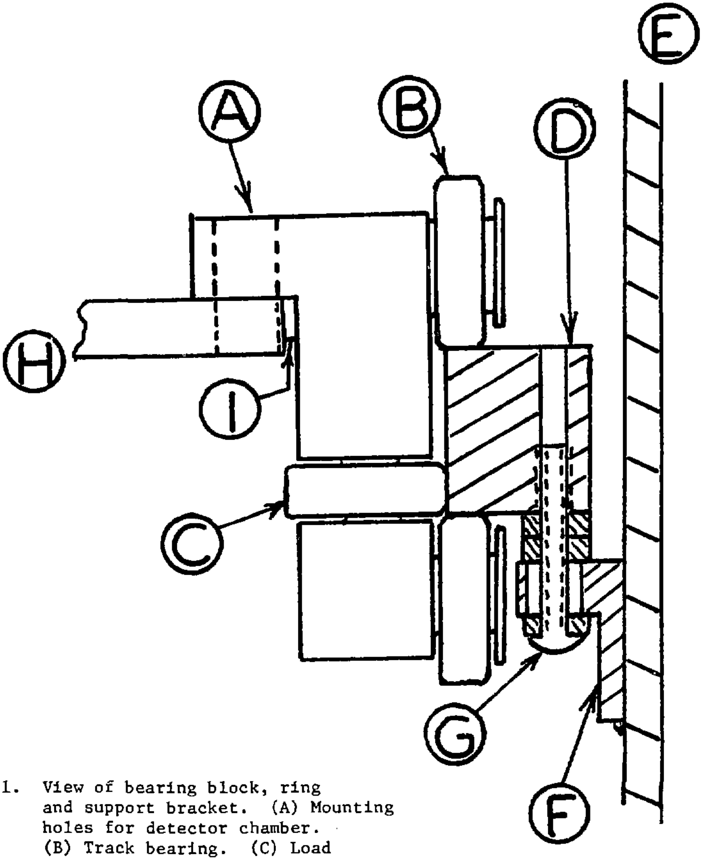

Fig. 11. View of bearing block, ring and support bracket. (A) Mounting holes for detector chamber. (B) Track bearing. (C) Load bearing. (D) Ring. (E) Main chamber wall. (F) Support bracket. (G) Ring mounting screw and nuts. (H) Detector chamber bottom plate. (I) Shims.

XBL 799-11399

with respect to the chamber when smaller bolts are used. The alignment procedure will be described in more detail in Section E.3.

2. Ring

The ring (17.430" OD, 16.115" ID, 0.790" wide) has 24 6^{32} set screws along its circumference. These set screws serve to initially set the ring in position. Another set of 24 6^{32} threaded holes on one face of the ring spaced between the set screws serve to bolt the ring onto 24 brackets which are welded onto the cricumference of the inner wall of the movable part of the belljar as shown in Fig. 12. The brackets have a 0.23" hole drilled into them which provides less than 0.1" of positioning adjustment for the ring. Thus, the ring can be translated in three dimensions. This is essential since the walls of the movable part of the scattering chamber are not necessarily perpendicular or concentric with the 22" flange on the stationary part of the scattering chamber, which was the reference flange. With one nut tight against the ring and the other two tight against the bracket, the ring can be bolted into position.

The ring was machined out of one piece of stainless steel 304 to be flat and concentric to within 0.001". Care must be taken not to wrap the ring by excessive uneven tightening of the set screws or bolts.

3. Detector Chamber Alignment

The following the is the procedure for aligning the detector chamber:

a. Set up both lasers through both the primary and secondary source beam holes. The best alignment produces the most symmetric diffraction rings seen around the laser spot shining through the beam holes.

b. Insert a etched down welding rod through the primary beam hole allowing it to intersect the laser beam shining through the secondary source beam holes. Align a cathetometer with this spot and the intersection of the cross hairs on the 22" flange. There are markings on this flange for placement of the cross hairs.

c. Set the ring parallel to the 22" flange on the movable part of the main chamber by employing the L shaped jigs which have two parallel faces one of which bolts on the 22" flange and the other which is clamped with small c-clamps onto the ring. The ring can then be bolted in place by four of the bolts in the brackets. Take off the jigs and mount the chamber fixed in approximately the position to view the incident beam. It is easier not to mount the drive rod onto the chamber at this time. Bolt the 22" flanges together and check the height at which the primary laser beam hits the detector chamber relative to the detector chamber entrance hole. Use a ruler or your eyeball. Repeat the procedure again using shin stock material between the ring and the jigs to move the ring further from the 22" flange. In no case should the ring have to be moved closer to the 22" flange than the distance dictated by jigs. Note that at this point the incident laser beam need not go through the detector chamber hole openings since the radius of the rotating chamber and the x-y position of the ring have not been determined.

d. Insert a pointed, etched down welding rod through the detector chamber beam holes until it just intersects the spot made by the intersection of the secondary source laser beam and the primary beam welding rod. As the detector chamber is rotated watch through the cathometer the point of the welding rod and determine if the point remains in one place. If it does not, then the detector beam line is not a radius of the ring and the bearing blocks have to be rotated and clamped with smaller bolts as described in Section D.1. This adjustment is non-trivial as there is no easy way to measure the magnitude and direction of the necessary corrections. Once it has been accomplished, however, the positions of the two blocks can be marked and need not be removed when the chamber is removed from the ring. The third block is always put back in a position to complete tightly the circle the inner diameter of the ring.

e. When the detector chamber is determined to rotate concentrically around one point, determine whether this point is in line with the cathetometer. If not, then its position is easy to measure with the cathetometer. The x-y position of the ring from the wall of the chamber can be measured and changed to the new position by loosening up one of the nuts on the four brackets that were tightened and adjusting the ring with the set screws on the inner diameter. When the correct position is determined thread all of the bolts into the ring and fasten them to the brackets.

4. Rotation Drive Mechanism

The rotation drive mechanism which is accessible outside the main chamber converts linear and angular motion into pure angular rotation of the detector chamber. The bellows (1.89" OD, 1.36" ID) sealed linear feedthrough is designed for three inches of translation and about 16° of angular tilt parallel to the plane in which the detector rotates as indicated in Fig. 12. The controlled linear motion is accomplished by threading a nut held stationary from linear motion in a bracket on a threaded (40 threads/in) 0.75" diameter stainless steel rod. The nut is spring loaded so that it is always held in the bracket with a constant force whether the chamber is being pulled up or pushed down. The bracket into which the rod is threaded pivots a maximum of 7.68° from its position parallel to the 2.75" OD flange to provide the angular motion for the rod as the rod translates. Two bearings (NMB 0.625" OD, 0.375" ID, 0.156" thick) are press fit into the end of the drive rod. A 0.375" shaft which is at one end of a 1.5" lever is secured into the bearings by a spring ring. The other end of the lever has a 0.030" deep step bored into it into which the stud at the center of the detector chamber fits snugly and two 0.125" holes to accommodate dowel pins. These dowel pins position the lever with respect to the detector chamber. One dowel pin is pressed

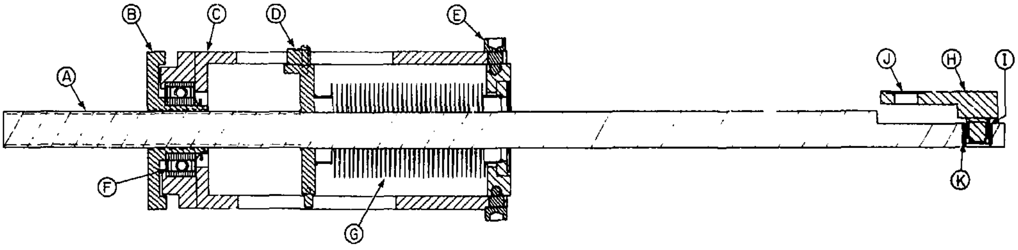

XBL 799-2864

Fig. 12. Rotation drive mechanism. (A) 0.75" drive rod. (B) Nut. (C) Bracket. (D) Z Indicator. (E) Pivot bolts. (F) Bearing, 2" OD, 1" bore, 0.625" wide. (G) Bellows. (H) Lever. (I) Lever bearings. (J) Detector chamber stud seat. (K) Spacer.

into the stud of the detector chamber. The other pin slips through the lever and into the stud and is held captive by the 1/2 ^{20} bolt which bolts the lever to the stud. The drive mechanism is positioned so that the weight of the chamber pulls on the rod rather than pushes on it, thus minimizing the necessary diameter of the drive rod. The larger markings on the bracket are in tenths of inches and the smaller markings are each 0.025". One revolution of the drive nut corresponds to 0.025" translation of the rod. The 360 markings on the circumference of the drive nut are in degrees.

Table I shows the reproducibility of the detector rotation as a function of the position of the drive rod. In column one is a reading in inches of the position of the drive rod as indicated on the scale marked on the bracket. In columns 2 through 5 are measurements of an arbitrary angle of a flat edge of the detector chamber measured with a protractor and a plomb. The protractor can only be read to the nearest 0.25°, but the precision of three measurements is 0.13° on the average. The angles in columns 2 and 4 were measured upon moving the detector chamber in a clockwise fashion and those in columns 3 and 5 upon moving the detector chamber in a counterclockwise direction as viewed from the manipulator end. There is no measureable hysteresis in the movement of the detector chamber until a value of 0.6 is reached. Apparently, the force acting on the chamber's center of mass which eliminated any play in the drive mechanism for larger z values is too small to be effective at these

Table I

z	θ_{cw}	θ_{ccw}	θ_{cw}	θ_{ccw}
3.1	35.0	35.0		
3.0	27.5	27.25		
2.9	21.5	21.0		
2.8	16.0			
2.7	10.75	10.75		
2.6	6.25	6.25		
2.2	-10.00	-10.25		
1.8	-26.00	-25.75		
1.6	-33.75	-34.25		
1.3	-46.00	-46.50		
1.0	-59.5	-59.5	-59.25	-59.5
0.6	-81.75	-82.75	-81.50	-83.0

angles. A z value of 0.6 corresponds to an angle of about 15° from direct line of sight of the incident beam. Thus these angles of the detector chamber would only be used for very glancing incidence experiments were $\theta_i \geq 80°$.

5. Detector Chamber - Angular Calibration

The absolute angle at which the detector sits is determined by referencing it to the position at which the detector is in direct line of sight of the incident beam. The rotary feedthrough on the manipulator which controls the angle of incidence rotation of the crystal and which has angular markings in degrees on its head is employed to measure the changes in angle at which the detector is located. A flat polished aluminum disk is mounted in the crystal holder of the manipulator. The disk is tilted in the manipulator such that the plane determined by the specularly scattered laser light shone through the primary source for two different angles of incidence of the disk is the same as the plane in which the detector line of sight rotates. Another words, the disk is oriented such that the specularly scattered laser beam shines off the disk and through the detector for two angles of incidence and thus two angular positions of the detector. The angular calibration can then proceed. The detector is first placed in direct line of sight of the incident laser beam. The aluminum disk correctly mounted in the manipulator is oriented now such that the laser beam makes a 90° incident angle to the crystal. This is determined when half of the laser spot seen through the detector disappears. This angle on the rotary feedthrough now becomes the reference angle. The angle θ_D at which the detector is positioned is given a value $\theta_D = 135°$. The precision of five angle measurements on this head is 0.22°. The z value of the drive mechanism rod is also noted. The crystal is then rotated exactly 22.5 ± 0.255° from the incident beam position. The detector is then rotated such that the specularly scattered beam passes through the detector. The detector now sits at an 45° angle with respect to the incident beam or $\theta_D = 90°$ and the z value is again noted. This procedure is repeated twice more with the crystal being rotated 45° and 65.68° away from its initial position. This brings the detector to 90° ($\theta_D = 45°$) and a 131.36° ($\theta_D = 3.64°$) respectively away from the incident beam. The results are tabulated in Table II. The angular position of the detector chamber relative to the incident beam has now been determined for three values of z.

The angular positions of the detector chamber for values of z other than the ones listed in Table II have to be calculated. It is clear from Tables I and II that the relationship between the z value and the angular position of the detector chamber is not a linear one. The angular position of the detector is proportional to the arccos of the square of the length of the drive rod from the lever to the pivot point of the bracket plus some constants.

Table II

θ_i	z value	θ_D
90.0°		135°
67.5°	1.211 ± 0.002	90°
45.0°	2.365 ± 0.002	45°
24.3°	3.111 ± 0.004	3.64°

In order to calculate the angular position of the detector chamber, the length of the lever, 1.50" and the distance from the center of rotation to the pivot point, 10.82 ± 0.05" must be known. Also known is the length of the drive rod from the pivot point on the bracket to the lever, $\ell = 12.20 \pm 0.015"$ with the drive rod marker at $z = 0.400"$. The geometry is indicated in Fig. 13. Thus, for $z = 2.365$, $\ell = 10.235$ and $\alpha = 63.34°$.

$$\ell = 12.20 - (z - 0.40) = 12.60 - z \qquad (1)$$

$$\alpha = \arccos\left[\frac{\ell^2 - (10.82)^2 - (1.5)^2}{-2(10.82)1.5}\right] \qquad (2)$$

The value of α obtained for $z = 2.365$ will be called α_{REF}. A value for α can be calculated from equation 1 and 2 for any value of z. The difference between this new α and α_{REF} is exactly the angle through which the detector has rotated. At α_{REF}, the detector makes an angle of 45° from an imaginary line 45° away from the incident beam as indicated in Table II and Fig. 14. The imaginary line would correspond to the macroscopic surface normal of a crystal for an angle of incidence of 45°. Thus, the position of the detector as measured from the surface normal can be calculated as

$$45 - (\alpha - \alpha_{REF}) = \theta_D \qquad (3)$$

Fig. 13. Drive mechanism geometry. Geometry for calculating angular position of detector. System constants are indicated.

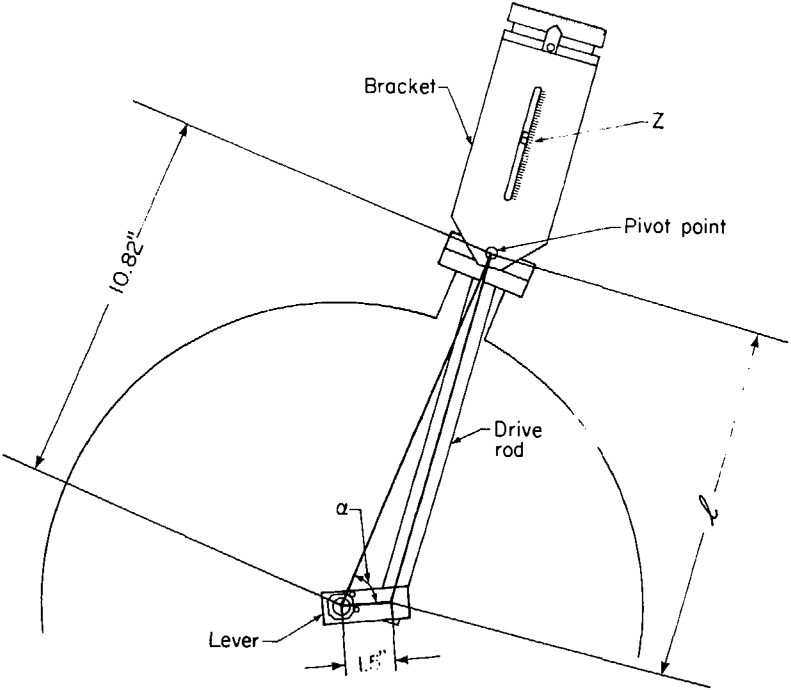

Fig. 13

XBL 799-2861

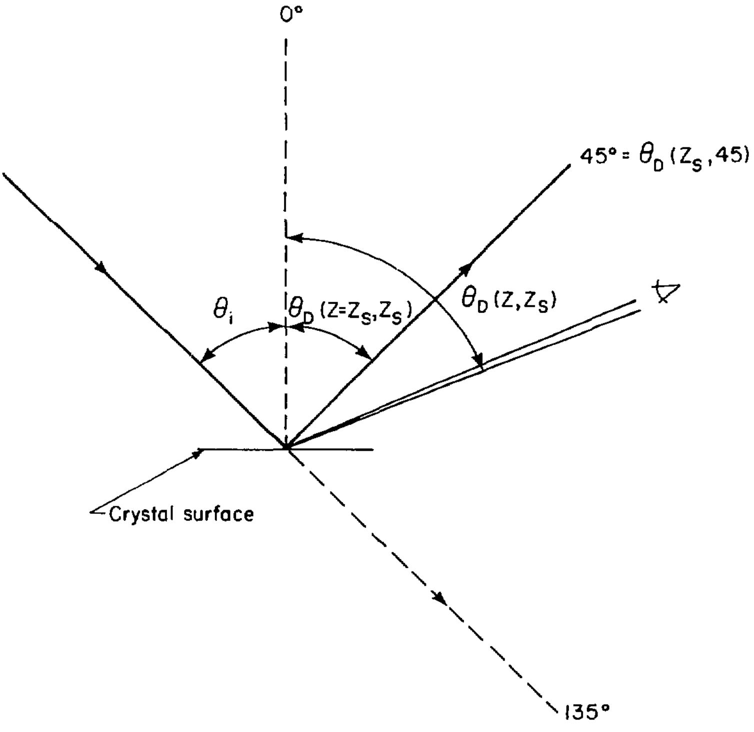

XBL799-2862

Fig. 14. Definition of θ_i and θ_D. The darker lines indicate the incoming and specularly reflected beams. The numerical values are correct for $\theta_i = 45°$.

This is done for many values of z in Table III. Also listed in Table III is a list of values of θ_D obtained from the two other absolute measurements of θ_D in Table II and from the differences in angles listed in Table I. For example, the θ_D measured value at $z = 3.1$ was obtained by first calculating $\alpha(z = 2.6) - \alpha(z = 3.1)$ and then comparing it the measured difference of $\theta(z = 2.6) - \theta(z = 3.1)$ listed in Table I.

$$\alpha(z = 2.6) - \alpha(z = 3.1) = 27.05 \text{ calculated}$$

$$\left|\theta(z = 3.1) - \theta(z = 2.6)\right| = 6.25 - 35 = 28.75 \text{ measured}$$

The measured value is 1.7° larger than the calculated one indicating that the detector is sitting 1.7° closer to the surface normal than is indicated through use of equations 1 and 2. Thus, the measured $\theta_D = 6.519°$. This provides a starting point for listing the other measured values of θ_D. From Table I the detector should rotate by 7.625° from $z = 3.1$ when z is changed to 3.0. Thus, $\theta_D = 14.147°$. The measured values in Table I are thus used to fill in this list in Table III. It can be seen that the correspondence between the measured values of θ_D and the calculated values of θ_D is poor for $z > 2.7$. Thus equations 1 and 2 can only be applied to calculate angles between $z = 2.7$ and 0.6. For $z > 2.7$ measured values of θ_D

Table III

z	θ_D(CALCULATED)	θ_D(MEASURED)
3.111"	7.23°	3.64°
3.100	8.07	6.32
3.000	14.86	13.94
2.900	20.64	20.07
2.800	25.83	25.32
2.700	30.62	30.57
2.600	35.13	35.07
2.200	51.55	51.45
1.800	66.92	67.20
1.211	90.32	90.00

have to be employed for determination of θ_D. The values of z between 3.1, 3.0, 2.9, 2.8 and 2.7 are interpolated from the measured values. Table IV presents the correct calibration of the position of the detector chamber when the beam is at a 45° angle of incidence to the crystal surface. The precision of these angles is ± 0.3° with the largest errors in the manipulator head and protractor readings.

The calibration in Table IV can be used to find the position of the detector chamber relative to the surface normal for other angles of incidence of the beam. First, the specular angle has to be determined by rotating the detector so that the specularly reflected laser beam shines through the detector. The z value is read off the drive mechanism (z_S) and the corresponding angle $\theta_D(z_S, 45)$ read from Table IV for $\theta_i = 45°$. The new angle of incidence measured from the surface normal is

$$\theta_i = \frac{\theta_D(z_S, 45) + 45}{2} \tag{4}$$

The surface normal has now rotated

$$\Delta\theta(z_S) = \theta_i - \theta_D(z_S, 45) \tag{5}$$

Alternatively, the angle of incidence can be determined by setting the crystal so that its angle of incidence is 45°, noting the reading on the head of the manipulator and then rotating the manipulator head by $\Delta\theta$ which is the same angle through which the surface normal has rotated. Values of $\theta_D(z, z_S)$ are given in Table IV for several angles of incidence. The new positions of the detector chamber relative to the surface normal for each value of z are given as

$$\theta_D(z, z_S) = \theta_D(z, 45) - \Delta\theta(z_S) \tag{6}$$

Values of $\theta_D(z, z_S)$ are given in Table IV for several angles of incidence.

Table IV

	$\theta_i = 60°$	$Z_S = 2.050$ $\theta_i = 51.2°$	$Z_S = 2.365$ $\theta_i = 45°$	$Z = 2.600$ $\theta_i = 40°$
Z	θ_D	θ_D	θ_D	θ_D
3.111	-11.36	-2.56	3.64	8.64
3.100	-8.68	.12	6.32	11.32
3.075	-6.64	2.16	8.36	13.36
3.050	-4.80	4.00	10.2	15.2
3.025	-2.80	6.00	12.2	17.2
3.000	-1.10	7.70	13.9	18.9
2.975	.60	9.40	15.6	20.6
2.950	2.10	10.9	17.1	22.1
2.925	3.60	12.4	18.6	23.6
2.900	5.10	13.9	20.1	25.1
2.850	7.80	16.6	22.8	27.8
2.800	10.3	19.1	25.3	30.3
2.950	13.0	21.8	28.0	33.3
2.700	15.6	24.4	30.6	35.6
2.650	17.9	26.7	32.9	37.9
2.600	20.1	28.9	35.1	40.1
2.550	22.3	31.1	37.3	42.3
2.500	24.4	33.2	39.4	44.4

2.450	26.5	35.3	41.5	46.5
2.400	28.6	37.4	43.6	48.6
2.365	30.0	38.8	45.0	50.0
2.350	30.6	39.4	45.6	50.6
2.300	32.6	41.4	47.6	52.6
2.250	34.6	43.4	49.6	54.6
2.200	36.5	45.3	51.5	56.5
2.150	38.5	47.3	53.5	58.5
2.100	40.4	49.2	55.4	60.4
2.050	42.4	51.2	57.4	62.4
2.000	44.3	53.1	59.3	64.3
1.950	46.2	55.0	61.2	66.2
1.900	48.1	56.9	63.1	68.1
1.850	50.0	58.8	65.0	70.0
1.800	51.9	60.7	66.9	71.9
1.750	53.8	62.6	68.8	73.8
1.700	55.8	64.6	70.8	75.8
1.650	57.7	66.5	72.7	77.7
1.600	59.6	68.4	74.6	79.6
1.550	61.6	70.4	76.6	81.6
1.500	63.5	72.3	78.5	83.5
1.450	65.5	74.3	80.5	85.5
1.400	67.5	76.3	82.5	87.5

1.350	69.5	78.3	84.5	[illegible].5
1.300	71.6	80.4	86.6	91.6
1.250	73.7	82.5	88.7	93.7
1.211	75.0	83.8	90.0	95.0
1.200	75.8	84.6	90.8	95.8
1.150	77.9	86.7	92.9	97.9
1.100	80.1	88.9	95.1	100.1
1.050	82.4	91.2	97.4	102.4
1.000	84.7	93.5	99.7	104.7
.950	87.0	95.8	102.0	107.0
.900	89.4	98.2	104.4	109.4

F. Manipulator

The purpose of the manipulator is to translate the crystal in three dimensions, 7.25" between the scattering center and the center of the retarding grids for electron energy analysis and ± 0.5" in the x-y positions, to rotate the crystal around its diameter ± 180° and around its center ± 180° and to provide a slight tilt motion, ± 6°, mainly for correction of warpage of the crystal when it is heated. The manipulator has four main parts; the x-y carriage on which the whole of the manipulator is mounted, the bottom flange on which the translation rods are anchored and which provides bearing surfaces for the tilt tube, the intermediate flange whose purpose is to provide the rotation and translation of the tilt wedge and to provide a feedthrough for the power lines and the top flange which actually holds the crystal and provides the rotational and z translational degrees of freedom. The manipulator will be described by each of its functions.

1. X-Y Carriage

The x-y carriage consists of three stages as shown in Fig. 15. The stationary stage bolts onto the machine and directly supports the secondary stage. The secondary stage moves vertically with respect to the stationary stage and directly supports the primary stage. Thus, the primary stage floats on the secondary stage moving horizontally and vertically with respect to the stationary stage. The whole of the manipulator then bolts onto the primary stage.

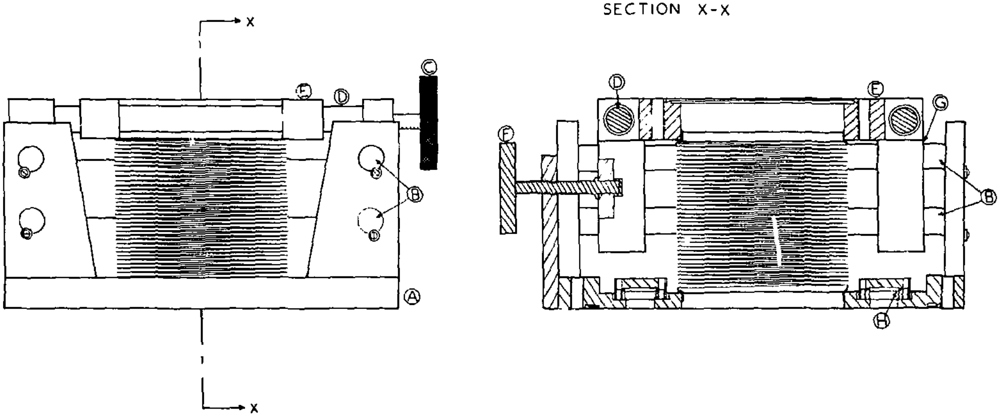

XBL 799-11375

Fig. 15. Side view and cross section of x-y carriage. (A) Rectangular plate stationary stage. (B) Secondary stage or vertical slide rods. (C) Primary stage handle. (D) Primary stage or horizontal slide rods. (E) Primary stage. (F) Secondary stage handle. (G) Secondary stage. (H) Mini-conflat flange.

The first stage is a rectangular plate 10" x 9.75" which bolts onto the main chamber via a 10" conflat flange. This plate also carried at each corner four, 0.625" case hardened stainless steel rods (two on each of two sides) on which the secondary stage slides to provide the vertical motion. Between two of the mounting brackets is another bracket which at its center position has a $5/16^{24}$ tapped hole. This accomodates a threaded rod with a handle to move the secondary stage vertically. A dial indicator is also attached to this plate and rests against the secondary stage to register its vertical position. The rectangular plate is 0.75" thick but has a 8" diameter 0.313" deep counterbore positioned at the center of the plate. Eight equally spaced mini-conflat flanges are welded into this plate on a 6" diameter. These could accomodate feedthroughs for cooling the crystal below room temperature. The rectangular plate has a 4" diameter hole in its center int which the collar of stainless steel welded bellows, 4.25" OD, 3.2" ID, 48 convolutions is welded. The other end of the bellows is welded to the first stage. Because this plate is too thin, there is considerable warpage of it upon bolting it to the 10" flange on the main chamber where an annealed copper gasket is employed between the rectangular plate and the 10" flange. This warpage causes the secondary and primary stages to bind on the slide rods. The warpage was measured at points between the bolts around the perimeter of the flange as the binding of the x-y motion began to occur. Shims ranging in thicknesses from 0.001" to 0.008" corresponding to the measured warpage were wedged between the rectangular plate and the 10" flange on the chamber. The rectangular plate was then bolted down securely with the x-y motion thus remaining free.

The secondary stage consists of three independent pieces which are held together by the slide rods. Each piece has press fit into it Cu-Be bushings which slide on the vertical slide rods. Two of the vertical rods between the two smaller pieces actually form the frame for the secondary stage. This arrangement allows access to the mini-conflat flanges on the rectangular plate. On the opposite side, the bracket sliding on the rods is one piece thus providing its own frame for support in addition to the support provided by the two vertical rods. This bracket has at its center position a $5/16^{24}$ threaded hole to mount the threaded rod and handle to move the primary stage horizontally. This bracket also mounts a dial indicator against the primary stage to measure the horizontal movement. The threaded rod used to move the secondary stage vertically passes through a hole in an additional brace bolted between the larger bracket and one of the smaller ones and is fastened on the opposite side. The secondary stage also mounts the two horizontal slide rods. All of the slide rods are easily removed by removing the stop screws mounted on the brackets by each end of the slide rods and then tapping the rods gently.

The rectangular primary stage has four Cu-Be bushings press fit into it which allow it to ride easily over the two horizontal slide rods. A centered 4" OD hole has the collar of the x-y bellows welded into it. The primary stage has machined into its face a knife edge to accomodate a 6" flange. The threaded rod for horizontal movement of this stage fits into a hole drilled into the side of the stage with a thin plate holding it in position.

2. Z Translation

The 7.25" Z translation of the crystal occurs by movement of the top flange, which holds the crystal via a 0.375" shaft along a set of three support shafts relative to the bottom flange. There a set of 3, 0.625" threaded rods threaded into the top flange. These rods are threaded for 20" of their 22" length. The smooth ends are fit into bronze bushings press fit into the bottom flange and are secured with spring rings. Rotary motion of one of the threaded rods is tranferred to the other two by a sprocket and chain arrangement near the bottom flange as shown in Fig. 16. The top flange slides along a set of 3, 0.75" support shafts, 21.5" in length, press fit into the bottom flange. These shafts are not equally spaced between any two threaded rods to allow accessibility for the electrical feedthroughs on the intermediate flange. The top flange as well as the intermediate flange has three ball bushings held securely by spring rings for smooth motion of the flanges along the shaft. The intermediate flange, which has clearance holes for the 0.625" threaded rods, retains its position relative to the top flange during this translation. Thus, the tilt wedge and the crystal holder do not move with respect to one another. The gold plated, MoS_2 covered, phosphor bronze bushing brazed into the tilt tube support as shown in Fig. 16 guides the translational motion of

Fig. 16. Cross section of bottom flange and tilt tube support. (A) 0.75" support flange. (B) Bottom flange. (C) Tilt tube support. (D) Tilt tube support bearing. (E) 0.625" threaded rods. (F) Sprocket and chain for z translation drive. (G) Bellows.

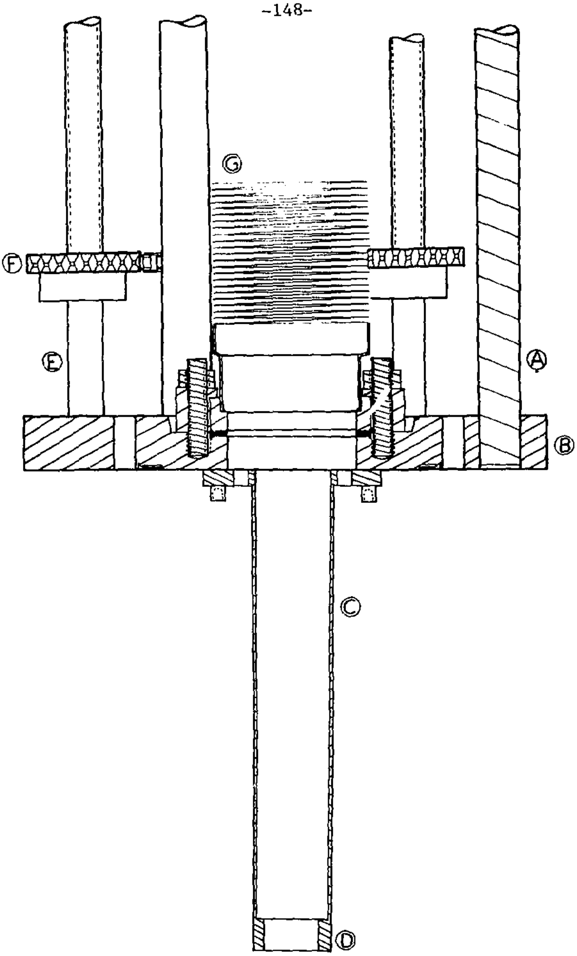

Fig. 16

XBL 799-11381

tilt tube and thus the translational motion of the crystal holder. A 2.44" OD, 1.53" ID stainless steel welded bellows with a total stroke of 12.84" maintains the vacuum seal between the intermediate flange and the bottom flange. The 2.50" OD collar of one end of the bellows is welded to a rotatable 3.5" OD flange. This is bolted to the bottom flange. The other end is welded via a 2" OD, 0.125" extension to what looks like a simple 3.5" OD flange. This flange, however, has been machined out of one piece to provide a holder for the tilt tube and the ceramic disk spacers in addition to securing one end of the bellows. Thus, this holder fits through the intermediate flange before bolting onto the intermediate flange. This flange will be described in more detail in section F.5.

3. Angle of Incidence Rotation

A rotary feedthrough with coaxial linear motion (Huntington PR-276) is bolted to the top flange via a 2.75" OD flange. This feedthrough allows one to change the angle that the beam makes with the crystal surface by rotating the entire crystal holder assembly. The original length of the 0.375" shaft, 11.625" is extended to a total length of 33.89" by two segments which have a $5/16^{24}$ threaded stud machined on one end of each segment. Thus, the other end of the segments has been drilled and tapped with the $5/16^{24}$ thread. Each segment also has a key machined into its end to correctly and rigidly align the shaft. The shaft is shown in Fig. 17. The crystal holder assembly, as shown in Fig. 18, is attached to the shaft by four set screws threaded through the upper tilt support. Thus, by loosening these screws the

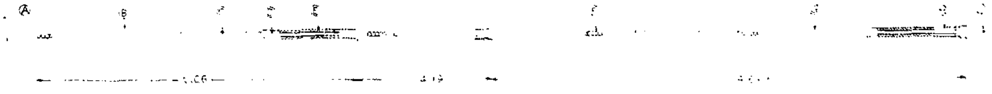

XBL 799-11603

Fig. 17. Cross section of 0.375" shaft. Cross hatching is not included. The first (10.06"), second (4.19") and third (19.63") segments of the 0.375" shaft are shown. (A) Bearing holder - Huntington rotary feedthrough. (B) 0.375" shaft. (C) 0.125" rod. (D) Spring stop. (E) Spring. (F) 0.125" ball bearings. (G) 0.130" bore of 0.375" shaft. (H) Set screw. (I) Cut out for roller assembly.

Fig. 18. Assembly cross section of crystal holder, tilt wedge and tilt tube. (A) Tilt tube. (B) 0.125" stainless steel balls. (C) 0.375" shaft. (D) Ceramic rings. (E) 0.0625" copper wire. (F) 0.125" azimuthal drive rod. (G) Spring. (H) Tilt wedge. (I) Roller assembly and 0.005" wire. (J) Ceramic crystal mount. (K) Clock spring. (L) Ceramic filament holder. (M) Lower tilt surface. (N) Crystal holder. (O) Upper tilt surface. (P) Set screw. (Q) 0.375" shaft bearing and metal spacer for electrical wires.

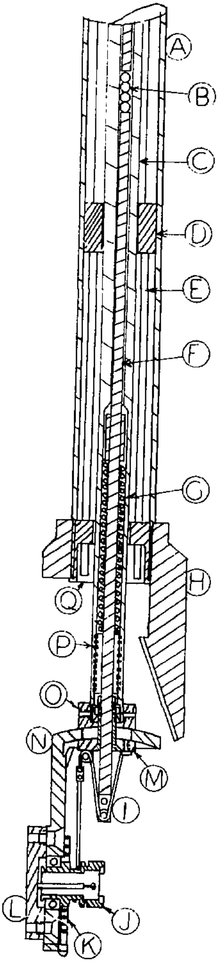

XBL 799-11380

Fig. 18

whole crystal holder assembly including the upper and lower tilt surfaces can be removed as a unit. A gold plated bronze bushing located in the end of the tilt tube and held in place by four screws passing through the tilt tube and the tilt wedge provides support and a bearing surface for the 0.375" shaft about 3.75" away from the crystal. The rotary feedthrough can provide a continuous 360° rotation but this rotation is limited here to ± 180° by the length of the flexible electrical wires emerging from the tilt tube which remains stationary during this operation. The head of the rotary feedthrough has markings in degrees. The accuracy of repositioning a chosen angle is 0.22°.

4. Azimuthal Rotation

The azimuthal rotation of the crystal involves rotation of the crystal surface around a line perpendicular to its center. This is accomplished by rotating the ceramic crystal mount. The ceramic crystal mount fits tightly into a 0.625" OD, 0.375" bore, 0.156" wide ball bearing which is press fit into the crystal holder as shown in Fig. 18. A step in the ceramic crystal mount fits up against the inner race of the bearing and is secured on the other side of the bearing with a spring ring. The ceramic crystal mount is rotated by pulling a 0.005" stainless steel wire which is wrapped around the smallest outer diameter (0.318") of the mount and anchored from the inside of the ceramic mount by being knotted after passing through a small hole. Upon releasing the wire, the crystal mount rotates back to its original position by the tension provided by a small clock spring anchored in the ceramic crystal mount and on the stationary crystal holder. This wire is actuated by attaching it to the 0.125" rod which runs coaxially down the 0.375" shaft of the rotary feedthrough described in the previous section. This 0.125" rod has an available translation of 0.50" which is actuated by a small micrometer on the rotary head In order to rotate the crystal 360°, a linear translation of 1" is required for the diameter of the ceramic crystal mount employed. Thus, the wire has to be looped once to double the length of translation as shown in Fig. 18. The wire is screwed securely at one end to the lower tilt surface and rides along a groove on a roller which is attached to the end of the 0.125" drive rod. The wire is then looped through another grooved roller which is part of the lower tilt surface before wrapping around the ceramic crystal mount. The roller assembly is bolted on the end of the 0.125" rod and has to be removed before the crystal holder assembly can be removed. The 0.125" rod is really a set of 5, 0.125" molybdenum rods intersperced with 0.125" stainless steel ball bearings. This arrangement alleviates the necessity of having a very straight piece of 0.125" rod for 36" of length which might buckle when force was applied to it. These rods are spring loaded at the end of the shaft of the commercial part of the rotary head and near the end where the 0.375" fits into the upper tilt surface. The first segment of the 0.375" shaft is bored out to 0.257" for a length of 3". This allows clearance for the 0.25" collar attached to the 0.125" rod. This collar acts as a stop for a 2" long, 0.045" wall, 0.24" diameter spring which is initially put under tension by screwing in the end of the second segment. This is shown in Fig. 17. The length of the rod above the collar, 6.719", in addition to 19, 0.125" ball bearings and 2, 0.25" long, 0.125" dowel pins are required to achieve the correct initial tension on the spring when the micrometer on the rotary head is retracted and when the second segment is screwed in place. The end on the third segment is also bored out to accomodate a 0.125" rod with a 0.25" collar. The same type of spring is used on the third segment as on the first and it is initially put under tension by a 5/16^{24}, 0.675" long set screw with a 0.125" hole through its center which is threaded into the end of the 0.375" shaft. The 0.125" bore along the assembled shaft is filled with two, 6" rods, 1, 2.905" rod, 18 balls and the length above the collar 3.285", to achieve the correct tension on the spring and the correct length of the 0.125" rod for pushing the wire. Thus, as the pressure from the micrometer is released, the 0.125" rod retracts back into the 0.375" shaft extending about 0.3" (which includes the length of the roller assembly) beyond the lower tilt surface.

5. Tilt

The crystal holder is made out of two parts, the stem and the spherical surface, which have been brazed together. The crystal sits on the ceramic mount which sits in the stem. It is at the center of a sphere of which the spherical surface is a section. The spherical surface is called the tilt surface. The inner and outer radii of the of the spherical shell section are 1.625" and 1.75" respectively. The spherical shell section is lubricated with imbedded MoS_2 particles. This spherical shell sections is clamped between two spherical surfaces, the upper and lower tilt surfaces. The three pieces are tightly clamped with spring tension provided by a Belville washer by a specially machined with a 10^{32} flat head screw and a 10^{32} nut machined down to fit inside of the 0.310" diameter bore (for 0.320" length) inside of the 0.375" shaft. The 10^{32} screw has a 0.130" center hole through its length to allow the 0.125" azimuthal drive rod to pass. When the crystal holder assembly is bolted onto the 0.375" shaft, movement of the tilt surface with respect to the upper and lower tilt surfaces causes the crystal surface to tilt around its center in any direction with respect to the 0.375" shaft. The angular tilt is limited to ± 5.9° by the sizes of the 10^{32} screw and the clearance hole in the tilt surface.

The movement of the tilt surface is effected by translating the tilt wedge to touch the circumference of the tilt surface. As the translation of the tilt wedge continues, it causes the tilt surface to slide with respect to the upper and lower tilt surfaces because of its wedge shape. The phosphor bronze wedge has machined on its inside surface the radius of the spherical shell section so that the crystal will not rotate as the wedge pushes. The tilt wedge is bolted onto the tilt tube by four screws which also hold the 0.375" shaft bearing. The tilt tube translation occurs by movement of the intermediate flange relative to the top flange. There are a set a 3, $3/8^{24}$ threaded rods which thread into the intermediate flange and which rotate in bronze bushings press fit into the top flange. The three rods are simultaneously driven by a sprocket and chain arrangement on the top flange. The translational motion of the intermediate flange employs the 0.75" diameter shafts as support and guides. A 3.25" OD, 2.25" ID stainless steel welded bellows with a stroke of 1" is welded to one end of the electrical feedthrough can and the other end is welded to a 4.5" OD rotatable flange to maintain the vacuum seal between the top and intermediate flanges. These flanges are shown in Fig. 19.

The tilt tube holder is part of the 3.5" OD flange which bolts onto the intermediate flange and on which is welded the Z translation bellows. The tilt tube is mounted in the tube holder. The tilt tube rests in a Cu-Be bushing and against a step in the Cu-Be bushing which is screwed into the tilt tube holder. It is secured in this position by clamping it together with the ceramic disk spacers. The tilt tube has a 0.125" plate which has 4, 4^{40} threaded holes, 8 clearance holes for the electrical wires, and a clearance hole for the 0.375" shaft brazed into its inner diameter 0.313" from its end. Four, 4^{40}, 3" long threaded rods thread into these holes. These rods then mount the ceramic disk spacers which when screwed down tightly with socket head nuts clamp the tilt tube against the step in the Cu-Be bushing and hold the spacers in the tilt tube. The ceramic disk spacers will be described in more detail in section F.7.

The tilt tube also has brazed on it a stainless steel gear 1" from its end. This gear engages perpendicularly in a gold plated gear which is screwed on a 0.187" shaft of a bellows sealed rotary

Fig. 19. Assembly of top and intermediate flanges. (A) Rotary motion feedthrough for angle of incidence rotation. (B) Micrometer for azimuthal rotation. (C) Threaded rods for z translation. (D) Sprocket chain and threaded rods for tilt wedge translation. (E) Top flange. (F) 4^{40} threaded rods and nuts. (G) Ceramic disk spacers. (H) Gear on rotary feedthrough. (I) Rotary feedthrough for tilt wedge rotation. (J) Tilt tube holder. (K) Tilt tube. (L) 3/8" shaft. (M) 1/8" rod. (N) 1/16" electrical wire. (O) Tilt tube gear. (P) 1/8" plate. (Q) Cu-Be bushing. (R) Intermediate flange. (S) Electrical feedthrough flange. (T) Copper ring.

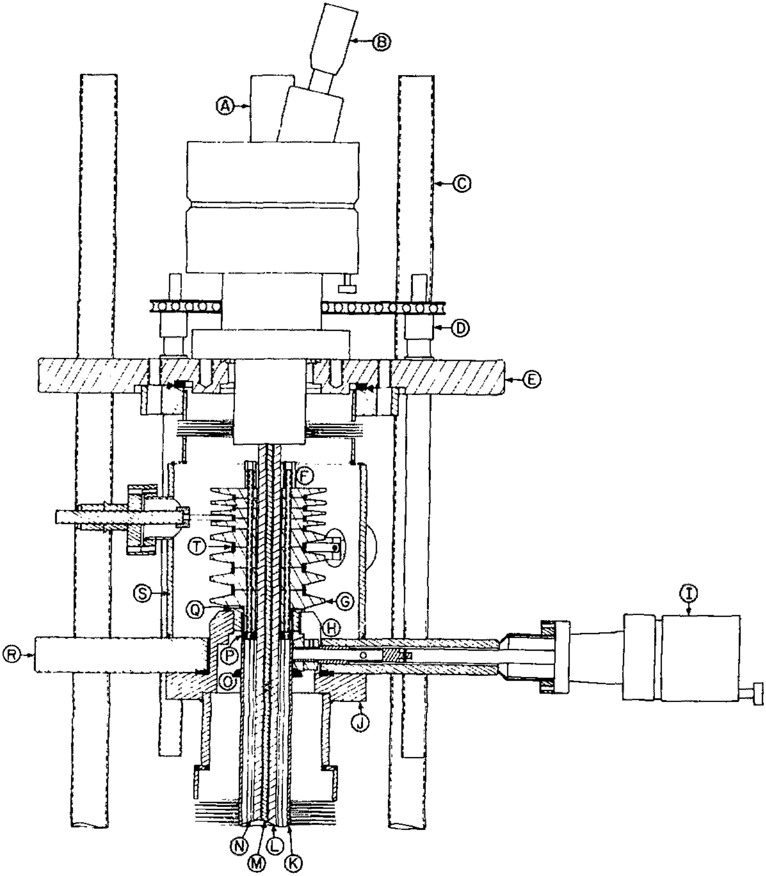

Fig. 19

Varian feedthrough. This arrangement allows the tilt wedge to rotate ± 180° so that the tilt motion of the crystal can occur in any plane. The shaft of the rotary feedthrough passed through a 0.310" diameter channel cut along a radius of the intermediate flange. The shaft has its own Cu-Be bearing on its end to rotate in this channel. The Cu-Be bearing has flats machined on it for pump out of the long channel. The rotary feedthrough bolts onto a mini-conflat flange welded to the intermediate flange. The rotary feedthrough has to be unbolted from the flange and pulled back in order to remove the tilt tube holder. The tilt tube holder has a slot cut into it to clear the gear on the rotary feedthrough when in operation but does not have enough clearance for its removal from the intermediate flange. The tilt tube support bearing supports and guides the motion of the tilt tube.

6. Crystal Mount and Crystal Heater

The crystal surface forms the lid of a ceramic cylinder whose other end is press fit in a bearing as described in section F.4. The crystal has 2, 0.005" Pt wires running near the edges of it but across its face. These wires are spot-welded to the 0.010" thick platinum backing foil which has a 1cm diameter hole in the center of it. The backing foil fits into a step machined into the edge of the ceramic cylinder. The shape of the step allows an oval crystal to be mounted. The backing foil has a long 0.005" wire spot-welded to it which loops through four small holes in the step edge of the ceramic mount. The ends of the wire are tied tightly together and spot-welded thus securing the backing foil to the ceramic mount. This wire is also attached to the wire which controls the azimuthal rotation of the ceramic crystal mount. This wire is electrically insulated from the 0.125" rod by a small ceramic piece. Thus, the crystal is electrically insulated from the machine ground so that a bias voltage can be applied to it or current to the crystal can be measured. The thermocouple which is spot-welded to the backing plate is wrapped in a groove on the outside of the ceramic crystal mount.

The crystal is heated by electron bombardment by a filament located at the center of the ceramic crystal mount and behind the crystal surface. The filament is a wound piece of 0.004" 2% thoriated tungsten wire. Each end of this wire is spot-welded to a 0.020" tungsten rod. Each of the 0.020" rods slips into a 0.531" long ceramic tube which is part of the ceramic filament holder. The ceramic tubes holding the filament fit through the center of the ceramic crystal mount and the whole ceramic filament holder screws onto the stem of the crystal holder. With typically 1.2 amps flowing through the filament biased at 2kV and the crystal grounded, the current to the crystal is typically 5ma. The temperature of the crystal at these settings is about 700°C. Crystal temperatures up to 1100°C have been obtained but these higher temperatures are more difficult to maintain due to charging of the ceramic crystal mount but the required higher emissions. The crystal can be additionally biased by a maximum of 600 V.

7. Electrical Feedthroughs

The electrical feedthrough can is welded to the intermediate flange. On it are welded seven mini-conflat flanges every 60° and in increasing distance from the intermediate flange as shown in Fig. 20. Each flange accomodates a 0.25" diameter copper rod feedthrough. At the end of each copper rod, a stainless steel trapezoidal block is bolted. A gold plated Cu-Be, 2" long, .020" thick strip is screwed onto the non-parallel sides of the stainless steel block. These strips which are forced open by a copper ring form the prongs of the stationary part of the rotatable electrical contact. The copper rings are stacked and spaced by the ceramic disk spacers. Each copper ring has a slightly etched down 0.0625" diameter copper wire soldered at a right angle on its inside diameter. The copper wires pass through holes drilled in a circular pattern in the ceramic disk spacers and pass through the tilt tube. The end of the first ceramic disk spacer fits into the inside diameter of the tilt tube but has a thin stainless steel ring around its circumference which forms the bearing surface with the Cu-Be bushing in which the tilt tube rotates.

The ceramic disk spacers are aligned by the 4, 4^{40} threaded rods which thread into the plate brazed 0.313" from the end of the tilt tube. The whole stack of ceramic disk spacers and copper rings bolt together with the tilt tube. Thus, the copper rings rotate with the tilt tube relative to the prongs of the electrical feedthroughs.

The 7, 0.0625" copper wires hanging in the tilt tube are kept spaced by 7, 0.625" long ceramic rings which have holes drilled into them in the same pattern as in the ceramic disk spacers. A ceramic ring is shown in Fig.18. These rings also have a clearance hole in the

Fig. 20. Top view of electrical feedthrough as seen with six of the seven spacers and rings stacked. (A) Electrical feedthrough can. (B) Trapezoidal block. (C) Prongs. (D) Ceramic disk spacer. (E) Copper ring with tab for mounting 0.0625" wire.

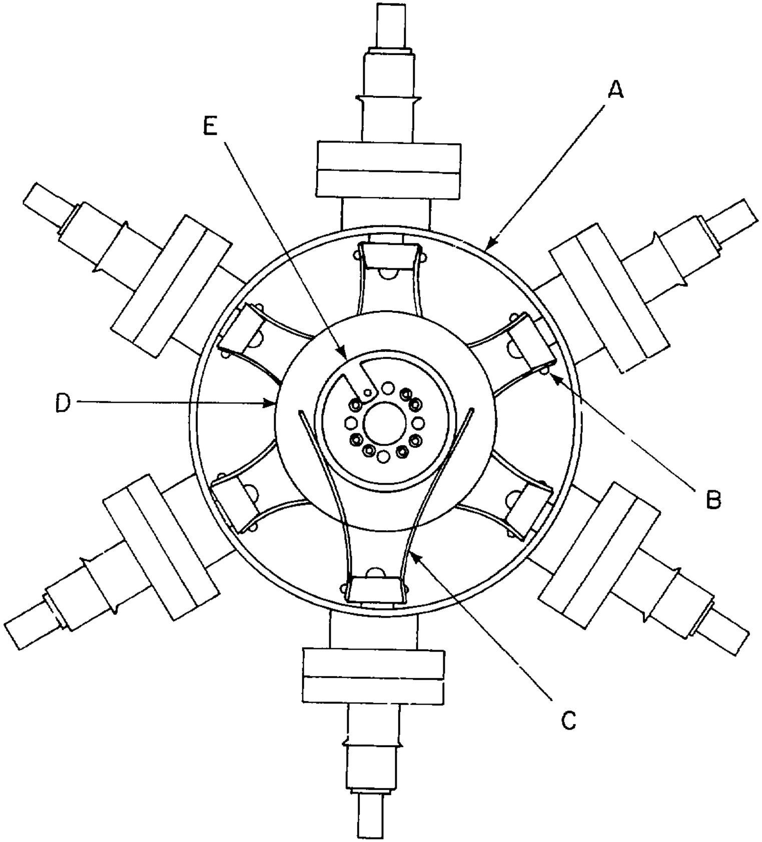

Fig. 20

XBL 799-2863

center for the 0.375" shaft. The rings are kept in position along the tilt tube by passing ceramic tubes over one of the wires between each ring. The spacer closest to the crystal is a metal one which also serves as the 0.375" shaft bearing as shown in Fig. 18. The wires emerge from the tilt tube where they have copper lugs screwed onto them which prevent the ceramic rings from falling out. At this point, flexible copper braid is attached to the lugs to run through the holes drilled in the tilt surface of the crystal holder down to the crystal.

C. Motor, Chopper and Trigger

The scattered beam rather than the incident beam will be modulated or some experiments in order to obtain velocity information by measuring the time of flight of scattered beam as a function of angle from the normal. A motor with a chopper blade is mounted on the detector chamber such that the beam is modulated just before entering the first collimating slit of the detector chamber. A trigger mechanism which consists of a light emitting diode and an photodiode mounted on opposite sides of the chopper blade provides a starting time for measuring the flight time of a molecule. An assembly drawing is shown in Fig. 21.

1. Motor and Motor Mount

The motor employed was a Globe 75A814. A high temperature coating on its windings and Barden stainless steel dry lubricated bearings, 0.625" OD, 0.250" ID, 0.187" thick with a glass reinforced telfon ball retainer are employed. The motor housing has been machined out to allow a spacer for the chopper blade to clamp against the inner race of the front bearing. The motor fits very tightly into a water cooled copper cylinder. The copper cylinder then floats on two O-rings in an aluminum block. A box fashioned out of 0.010" co-netic foil and spot welded together encloses the aluminum block. It is not known whether this box is necessary to shield the ion optics from the alternating magnetic field. The

Fig. 21. Cross section of motor, cooling block, chopper and trigger. (A) Chopper blade. (B) Al mounting block. (C) Cooling water cavity. (D) Motor. (E) Blade to shaft mounting pieces. (F) LED (G) Photodiode. (H) Boron nitride electrical insulator.

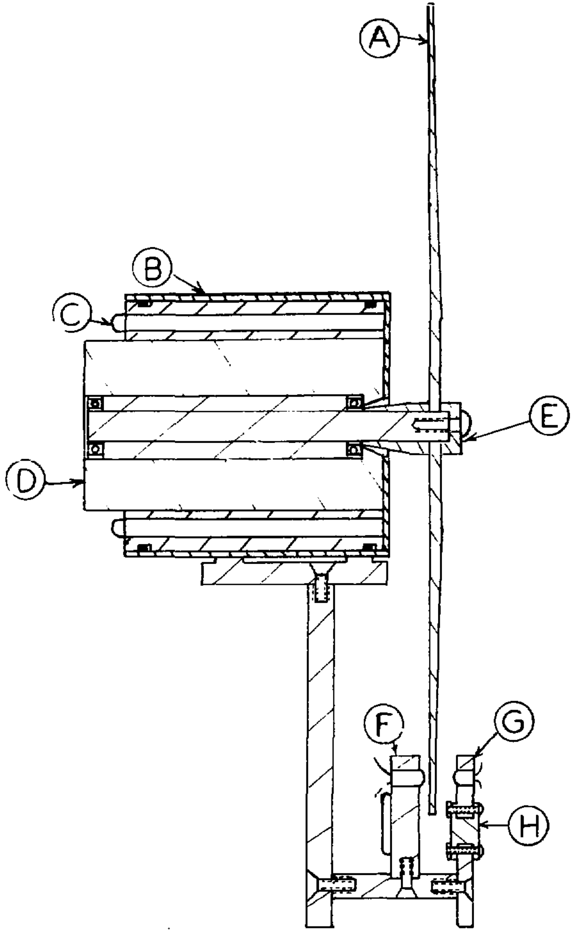

XBL 799-11674

Fig. 21

aluminum block fits onto four 10^{32} studs welded to the detector chamber and pushes against the wall with the appropriate length spacers between the block and the wall to fully cover the collimating slit.

The cooling water to the copper cylinder is provided by 0.125" OD, 0.016" wall stainless steel tubing soldered into the copper cylinder. The copper cylinder is actually two concentric hollow cylinders with the ends capped off so that the water can flow completely around the cylinder. The 0.125" tubing routes itself along the detector chamber and is welded to a right angle piece which is bolted down to the corner of the lever of the rotation drive mechanism. The tubing then forms a flat coil of about 8 turns behind the detector chamber before hooking up via a Cajon fitting to a feedthrough mounted on a 2.75" flange on the lower half of the belljar. The coil flexes as the detector chamber rotates since the tubing is securely mounted at the lever and at the feedthrough where the 0.125" is welded to 0.25" OD, 0.049" wall stainless steel tubing.

2. Chopper

The 8" diameter chopper wheel is fabricated out of a titanium-aluminum alloy (Ti-6Al-6V-2Sn). This material has a 140,000 psi yield strength which will allow the chopper to rotate safely as fast as 700 Hz without the tangential stress in the material exceeding the limit. Assuming a uniform thickness of the disk the maximum radial stress S_r and the tangential stress S_t are given by[14]

$$S_{r_{max}} = \frac{3+\nu}{8} \frac{\delta w^2}{386.4} (R - R_o)^2 \qquad \text{lb/sq. in.} \qquad (7)$$

$$\text{at} \quad r_{max_r} = \sqrt{RR_o}$$

$$S_{T_{max}} = \frac{1}{4} \frac{\delta w^2}{386.4} \left[(3+\nu)R^2 + (1-\nu)R_o^2\right] \qquad (8)$$

$$\text{at} \quad r_{max_t} = R_o$$

and R = radius of disk

R_o = radius of shaft hole

ν = Poisson's ratio = 0.3

δ = density of material = 0.0164 lb/cu. in.

ω = frequency of rotation rad/sec.

Note that these formulas will yield only lower limits to the maximum stress developed in the disk since the disk has additional off-center holes drilled into it for balancing.

The disk is 0.125" thick in the center for a diameter of 2" and then tapers down on one side to a thickness of 0.040" at a at a diameter of 4.5". The slits in the disk were cut radially with the disk clamped firmly between 2 brass plates. Each machined slit was filled in with cement before the next one was cut to prevent the slits from bending.

The slit pattern machined in the periphery of the disk is pseudorandom with each slit being a integral multiple (up to 8) of the smallest slit size. The pseudorandom binary sequence employed was generated by the output of a k bit binary shift register. The method of modulating the beam by a pseudorandom sequence is known as the cross correlation technique and is described in detail in references 15 and 16. One of the slits was machined more deeply along a radius of the disk to provide an opening for the trigger pulse as described in the next section.

Because of the random position of the slits a hole has to be cut into the disk to correct for the dynamical imbalance. The position of the hole and the area of the hole were calculated by requiring that the resultant force on the rotating disk be zero. Since the force on a uniform rotating disk is zero, (since the center of mass is on the axis of rotation) the resultant force on the cross correlation chopper is

$$\vec{F} = -\int \rho t \omega^2 \vec{r}\, dA \qquad (9)$$

where the slits are considered to have negative mass. The condition that has to be met is then given by

$$\vec{F} = \int\limits_{\text{slit holes}} \rho t w^2 \, \vec{r} dA - \int\limits_{\text{balance hole}} \rho t w^2 \, \vec{r}_b dA = 0 \qquad (10)$$

Where ρ is the density of material, t is the thickness, w is the angular velocity, $\vec{r}$ is the radial vector and A is the area. A program to solve this equation with the appropriate correction for the trigger slot is listed in Appendix A. In addition to this correction, the wheel was physically dynamically balanced. After machining, the wheel was again clamped tightly between two plates machined to fit the shape of the wheel and heated for 24 hours in a vacuum oven at 600°C to achieve a flat disk.

The chopper wheel fits tightly on the shaft of the motor and is bolted up against a conical piece which rides on the inner race of the motor bearing as shown in Fig. 21.

3. Trigger

The trigger provides a means of measuring the rotational frequency of the chopper. It consists of a Sharp GL 514 light emitting diode for the source and a Sharp PD 50PI pin photodiode as the receptor. They are mounted facing each other in a copper arm which is bolted to and extend out from the aluminum block holding the motor. The chopper blade passes between them as shown in Fig. 21. Both of the copper plates clamping the LED and the photodiode onto the arm and the arm itself have slotted screw clearance holes that the LED and the photodiode can be aligned with respect to each other and with respect to the slot on the chopper blade. One of the motor water cooling lines is soldered to the plate clamping down the LED.

The LED is forward biased with 5 volts with a 30 Ω resistor in series so that the forward current is about 100 mA. The photodiode is reverse biased such that the can is the cathode and is insulated from the copper arm by a boron nitride insert. The output from the diode is fed into a RCA CA 3130 op amp. The current to voltage converter circuitry is shown in Fig. 22. With no reverse voltage applied and a 20 mΩ load resistance the output pulse from the op amp is about 11 V at zero frequency with a rise time of 10 μsec.

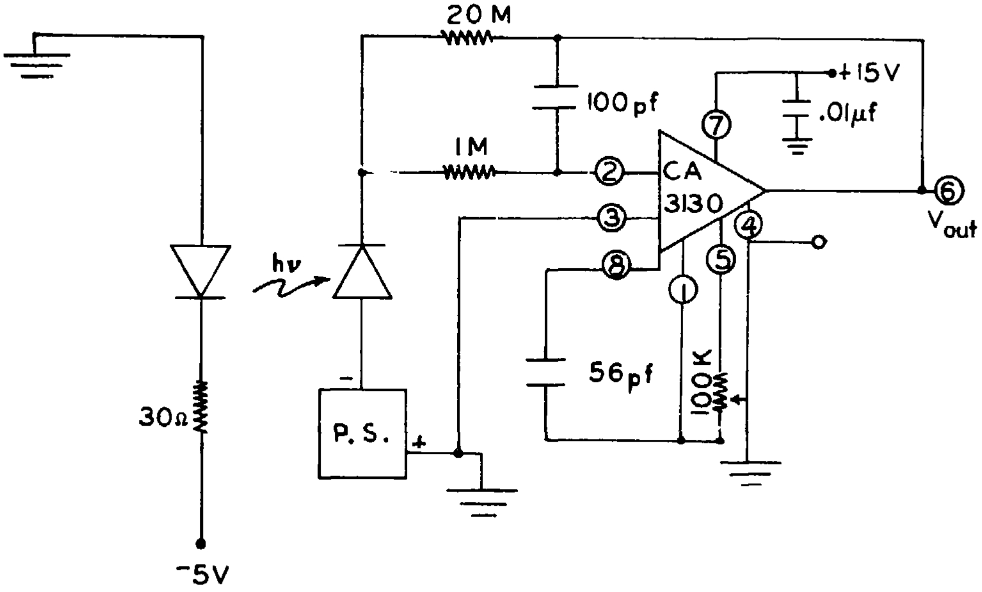

Fig. 22. LED and photodiode signal and amplifier circuitry.

XBL 799-11691

H. Hydrogen Atom Source

1. Construction

The hydrogen atoms are produced in a discharge located at the nozzle tip. The plasma is produced by a microwave cavity resonating at 2450 MHz which is held in a bracket attached to the source brass flange as shown in Fig. 23. The cavity is available from Opthos Instruments.[17] Water cooling coils were soldered to both the coaxial stem and body of the cavity. An unshielded copper wire brings the power from the electrical feedthrough to the cavity. An O-ring compression fitting is soldered into the center of the brass flange to hold the glass nozzle.

The glass nozzle consists of two concentric tubes. The inner tube with a 1 mm diameter hole on one end carries the source gas. The wall of the tubing is very thin, 0.010", for a length of about 3" from the nozzle. At this position the wall becomes thicker, (0.040") and the cross section of the tube becomes an ellipse. The two ends of the major axis of the inner tube are fused onto the outer tube dividing the outer tube into 2 sections. The inner tube is sealed off on the opposite end by an optical flat such that a laser beam can be shined through the tube and nozzle for alignment. The coolant flows down one side of the outer tube, around the nozzl area and back up the other side of the tube. Transformer oil is used to cool the glass tube since water efficiently adsorbs microwave radiation.

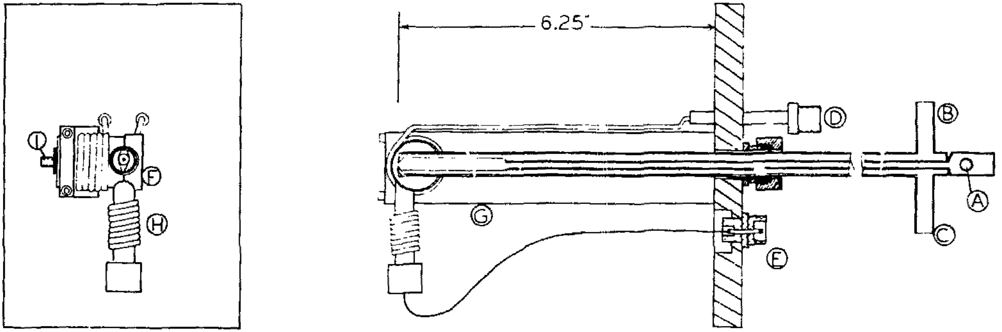

Fig. 23. Front and cross-sectional view of H-atom beam source. (A) Beam gas inlet. (B) Cooling oil inlet. (C) Cooling oil outlet. (D) Cooling water inlet. (E) Electrical feedthrough. (F) Microwave cavity. (G) Cavity support. (H) Cooling water coils. (I) Tuning stub.

The source was aligned by first aligning the laser through the beam holes in the buffer and source chamber walls and then inserting the source and aligning it with the laser. This alignment was effected by shims placed under the four corners of the beam source flange The thicknesses of the shins were then measured and the underside of the source flange was remachined according to the shim measurements. Final alignment is effected by varying the pressure of the clamps which hold the source flange against an overly thick o-ring.

2. Operation

A microwave diathermy unit (Burdick MW 200) is employed to deliver a maximum of 125 W of power to the cavity. If the cavity is well tuned, the discharge will remain stable with as little as 60 W power. Since the reflected power was not measured, it is not known how much power is actually adsorbed by the plasma. The cavity is first tuned by varying the length of the tuning stub and coupling slide outside of the source chamber so that the intensity of the discharge and the distance it extends out of the cavity region are maximized. The tuning remains adequate once the cavity is inserted into the source chamber. A spark from a Tesla coil is sometimes required to initiate the discharge. The flow of the oil coolant for the glass tube is interlocked to the microwave power supply. The water coolant for the cavity is not interlocked to the supply.

3. Performance

The per cent dissociation of H_2 was measured with a quadrupole mass spectrometer in another apparatus[18] which employed quadrupole rods which are longer, larger in diamter and are operated at a higher frequency than the ones employed in this apparatus (1.9 cm, 22 cm, 5.5 MHz versus 1.3 cm, 15 cm, 2 MHz). This allowed for unit mass resolution between masses 1 and 2 to be obtained with high sensitivity. The per cent dissociation was calculated as shown in equation .

$$\% \text{ Dis} = \frac{[H(f) + H_2(0.064)]}{H_2 + \text{NUM}} \; \frac{1}{2} \; (1.41) * \frac{0.8}{0.5} \qquad (11)$$

$$\text{where} \quad \text{NUM} = [H(f) + H_2(0.064)] \; \frac{1}{2} \; (1.41) * \frac{0.8}{0.5}$$

$$f = \frac{0.064}{H_{off}/H_{2\ off}}$$

H = mass 1 counts/sec

H_2 = mass 2 counts/sec

The probability for dissociative ionization via the processes shown in equations 12 and 13 is 0.064 at 200 eV electron energy.[19]

$$H_2 + e^- \longrightarrow H^+ + H + 2e^- \qquad (12)$$

$$H_2 + e^- \longrightarrow H^+ + H^+ + 3e^- \qquad (13)$$

The factor f is determined by dividing the H/H_2 ratio measured with the plasma off by 0.064. The factor f corrects for the transmission and detection of H relative to H_2. The 1/2 corrects for the number of H atoms produced relative to H_2. The factor 1.41 corrects for relative velocities of H/H_2 through the ionizer region. The factor 0.8/0.5 corrects for the difference in the ionization cross sections of H and H_2.[20]

The per cent dissociation measured did vary somewhat with emission in the ionizer. In 6 mA emission the mean per cent dissociation was 54% ± 3%. For 12 mA emission the mean per cent dissociation was 72% ± 4%. The effect of emission on the per cent dissociation was not fully investigated. The per cent dissociation does not vary significantly with pressure behind the nozzle between 0.4 torr and 1.1 torr. Below 0.4 torr the discharge cannot be maintained. Above 1.1 torr the per cent dissociation drops dramatically. The source has been operated stably for 24 hours at a time.

I. Surface Analytical Techniques.

The main chamber has facilities to ion bombard the crystal surface, analyze the composition of the surface by Auger electron spectroscopy and analyze its structure by low energy electron diffraction. Since this equipment is commercially available, it will not be detailed here. The ion gun is a Varian model 981-2043 with deflection plates. Typical emission is 15-20mA for a filament current of 3.5 amps About 15-20 A of Ar^+ ions will reach the crystal for a Ar background pressure of 1 x 10^{-4} torr. The detector chamber ion pumps are turned of when the main chamber is flooded with Ar for sputtering. The glancing incidence Auger electron gun is an oscilloscope gun mounted on a 2.75" OD flange and modified with a Varian 981-2612 filament and filament holder. Typical emission is 15mA at 3.3 amps filament current and at 60 V extraction potential. About 40 μA (2kV electron incident energy) will reach the crystal if it is properly aligned. The Auger electrons are energy analyzed on a Varian 3-grid optical system. The 3 grids are used as a retarding field energy analyzer. The high voltage impressed on the second grid is modulated at 2450hz and the signal collected on a screen biased at 300 V. A lock-in amplifier (PAR 124A) is employed in the notch filter mode to measure the signal. The 3 grid optical system is also used to measure LEED intensities by impressing the potential of the incident electrons on the first and third grids to allow only the elastically scattered electrons to reach the screen biased at high potential (6kV). A normal incidence electron gun is employed for LEED work. Its emission is about 30 μA for 1 amp filament current.

J. Mass Spectrometer

The mass spectrometer is mounted on a 4.5" OD flange which bolts into the detector chamber with a 0.700" thick spacer flange through the bottom plate. The mass spectrometer flange is about 3.4" inset from the bottom plate so that the feedthroughs can clear the ring. The length of the mass spectrometer from the inner surface of the flange to the filament is 11.187". The mass spectrometer is aligned visually with the entrance holes in the detector chamber both in height and in angular orientation of the filament with the entering beam by inserting an appropriate size rod through the detector chamber slits. The major height adjustment is accomplished with the spacer flange described above. The final adjustment is made by varying the compression of the mass spectrometer flange on the annealed copper gasket. Note that because this is a seal between the mass spectrometer chamber and the main chamber the flanges do not need to be metal to metal. The angular orientation of the filament can be varied by rotating the bottom plate of the Faraday cage along with the extractor plate. The four mounting rods of the ionizer pass through slots in the bottom plate of the Faraday cage and the extractor rather than holes for this adjustment. The filament should be parallel to the beam.

The ions are generated by electron bombardment from a Pierce gun.[21] The 1 cm long, 0.010" thick 2% thoriated tungsten filament held under tension can generate 6 mA emission at an extraction voltage of 200 V (electron energy) with 5.7 amps flowing through it. The filament sits about 0.5" away from the center of the ionizer making the width of the sheet of electrons from the gun about 3.4 mm at the center of the ionizer for an electron energy of 200 V and current density of 2.5×10^{-2} amps/cm^2. This spreading of the electron beam due to space charge can be calculated from equation 14.[22]

$$\frac{b_1}{b_o} = \frac{4.8 \times 10^8\ jl^2}{V^{3/2}} + 1 \tag{14}$$

where b_1 = thickness of the sheet of electrons at distance 1 from the filament.

b_o = original thickness of the sheet of electrons ~2 mm.

j = current density of electron beam in A/cm^2.

1 = distance measured from filament in M.

V = electron energy in V.

The extraction plate sits immediately beneath the ionization region bending the ions 90° from their initial direction. The extraction plate as well as the bottom plate of the Faraday cage has a slot 0.71" long and 0.25" wide to extract the ions formed over a 1 cm length and in a 0.133 cm^2 cross section. The first and second lenses have circular holes 0.710" in diameter and 0.500" in diameter respectively to collect the diverging ion beam and then to focus it down to the opening of the quadrupole housing 0.188" in diameter.

The lenses are mounted on four threaded rods which bolt into a ring mounted on the quadrupole housing and are insulated from the rods and separated from each other by ceramic spacers. An assembly drawing of the ionizer is shown in Fig. 24. The height of the ionizer from the bottom of the mounting ring to the filament is about 1".

Figures 25 and 26 show the calculated equipotential lines and the calculated trajectories of an ion for approximately the lens system employed. The extraction plate opening is smaller in this calculation by 30% compared to the one employed. This calculation also assumes cylindrically symmetric geometry which is not strictly true in the ionizer region. The calculations are described in Appendix B. A value for the space charge density due to the presence of the ionizing electron beam was calculated and employed in the calculations. Figure 26 shows the trajectories of particles with initial kinetic energies varying from 0.025 to 5 eV. Except for the two ions whose initial kinetic energies were 5 and 3 eV, all the ions are focussed successfully into the opening of the quadrupole housing with an angle smaller than 30° with respect to the axis of the mass filter. Thus, for wide energy distributions of the scattered beam the lens system for a given setting will not extract ions with widely different initial kinetic energy with the same efficiency. Calibration of the ionizer as a function of incident kinetic energy of the beam will have to be carried out.

Fig. 24. Side and top assembly views of ionizer. (A) Bottom plate Faraday cage. (B) Back plate Faraday cage. (C) Left anode support. (D) Right anode support. (E) Cathode-Pierce gun. (F) Top plate Faraday cage. (G) Extractor. (H) First lens. (I) Second lens. (J) Quadrupole entrance. (K) Quadrupole rods. (L) Anode. (M) Threaded rods. (N) Ceramic ring insulator. (O) Threaded rod mounting ring. (P) Cathode-anode insulator. (Q) Cathode mount. (R) Ceramic filament holder.

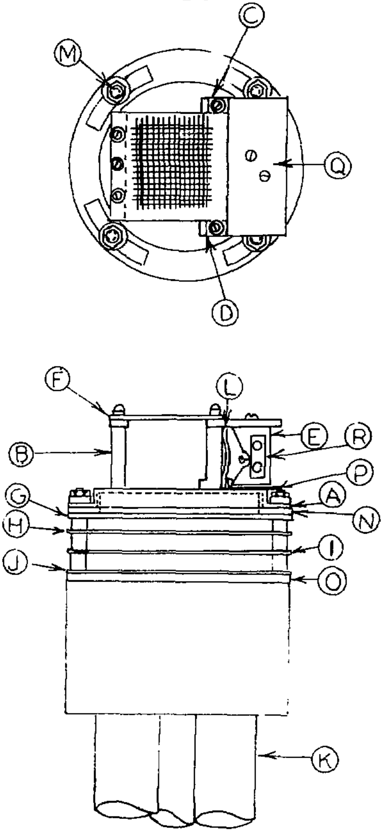

XBL 799-11378

Fig. 24

Fig. 25. Equipotential plot for ionizer lens system assuming cylindrical symmetry around z. The two adjacent squares indicate the ionization region where the electron charge density is assumed to be 1×10^{-10} coul/cm^3. Anode = +50 V, extraction lens = -5 V, first lens = -250 V, second lens = -500 V, quadrupole entrance = 0 V. The voltages are labeled in Fig. 26.

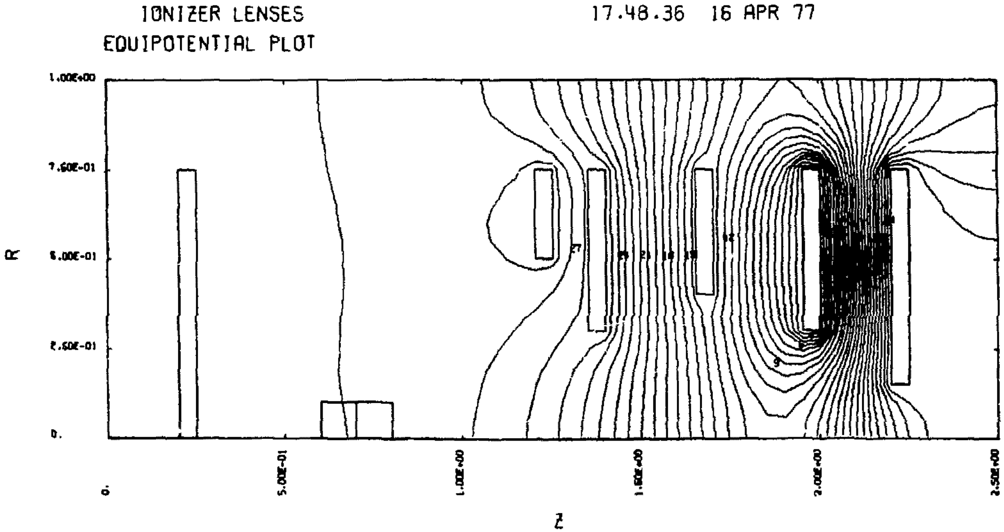

XBL 799-11712

Fig. 25

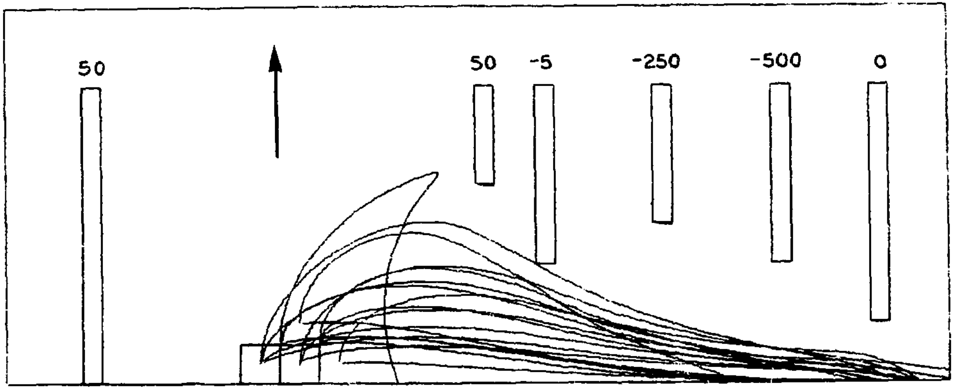

XBL 799-11713

Fig. 26. Positive ion trajectories in the field whose equipotential lines are shown in Fig. 25. Arrow indicates direction of neutral beam. The two sets of trajectories with the smallest initial values for the abscissa and ordinate represent initial kinetic energies of 0.026, 0.1, 1 and 3 eV in the direction of the arrow.

A UTI 100C mass filter, mounting and Channeltron 4770 series electron multiplier make up the remainder of the mass spectrometer. The size of the mass filter employed (6" rods, 1.27" diameter) was dictated by the dimensions of the lower half of the belljar. The Channeltron is offset from the axis of the quadrupole with a Faraday cup in direct line of sight of the ions as they emerge from the quadrupoles.

Experimentally, it has been found that the following potentials on the ionizer give the maximum signal and the maximum signal to noise for mass 32.

Electron energy	200 V
Emission	5 mA
Ion Energy	85 V
Extraction Voltage	-130 V
1st Lens	0 V
2nd Lens	+260 V
Faraday cup voltage	-135 V

K. Signal Electronics

The 10-15mV pulses out of the Channeltron are passed through a preamplifier, discriminator and pulse shaper, 13x 3032-51A. The output of this amplifier are +3V pulses into 120Ω. In the angular distribution mode these +3V pulses are fed into two counters, Ortec 775. The two counters are gated by a timer-gater module, 13x 3050, which outputs two gates whose phase and width are variable. The phase and width are set to maximize the difference in counting rate between the two counters. The timer-gater module is triggered from a pick-up coil of a 150hz tuning fork chopper mounted in the buffer chamber of the primary beam. Thus, one of the counters corresponds to the signal plus background when the chopper is open and the other corresponds to background counts when the chopper is closed. The timer-gater will count for a preset amount of time. A schematic is shown in Fig. 27.

In the velocity analysis mode, the +3V pulses from the amplifier are fed into a 255 multi-channel scalar, 13x 3501-P1. The multichannel scalar is triggered to start the address advance by the trigger pulses once every revolution of the chopper wheel as described in section G.3. The multi-channel scalar has its own oscillator to susequently advance the addresses and it also puts out a TTL compatible motor synch pulse every dwell time to externally drive the motor diver oscillator. The motor synch pulses are divided down by the motor synch scalar, 13x 3441-P1, to the correct frequency for driving the oscillator. The multi-channel scalar is interfaced to a Nova 2-10 computer

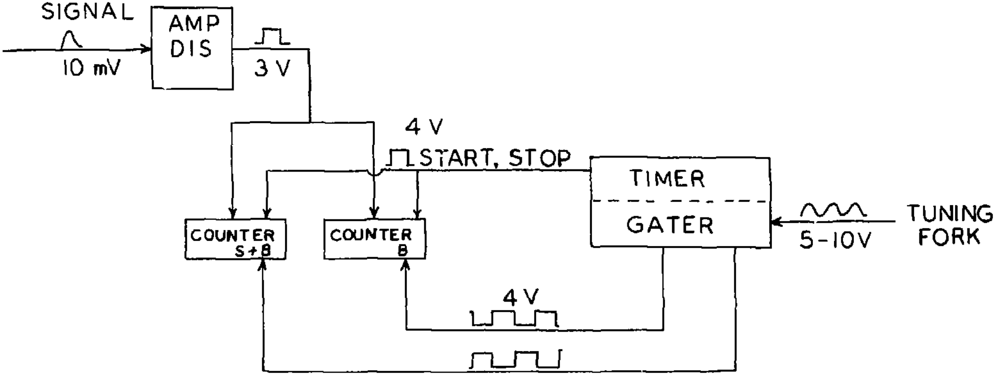

XBL 799-11714

Fig. 27. Angular distribution mode counting electronics.

via a CAMAC crate (NEI) and controller (Bi-Ra 1303). An oscilloscope display is also interfaced to the computer via a point plotter (Ortec PP012) in the CAMAC crate. A schematic is shown in Fig. 28. A computer program controls the acquisition of the data and the deconvolution of it. A flow diagram of the program is shown in Fig. 29.*

In the initialization, the program asks for the title (T:), date and starting run number (SRN:). These are used simply as headings. It then requests that the dwell time or time per channel in μsec (T/C:) and the number of trigger pulses per cycle (LP/C:) be set. It requests whether the chopper wheel is a correlation chopper (0) or a single shot chopper (1), the channel offset in channels (OFFS:), the rotation direction of the chopper wheel (RD (A or B):) (A corresponds to a rotation direction where the largest slit width passes the trigger immediately after the trigger pulse), disk storage of data (D:) (response is always N here), oscilloscope display (OD:) (Y or N), continuous display (CD:) (response is always N here) and automatic DC background subtraction (Y or N). The program then proceeds according to the flow chart. A sample of the teletype input/output is shown in Fig. 30. The deconvolution of the cross correlated data has been described in great detail.[15,16]

---

* The program is courtesy of the Y.T. Lee group.

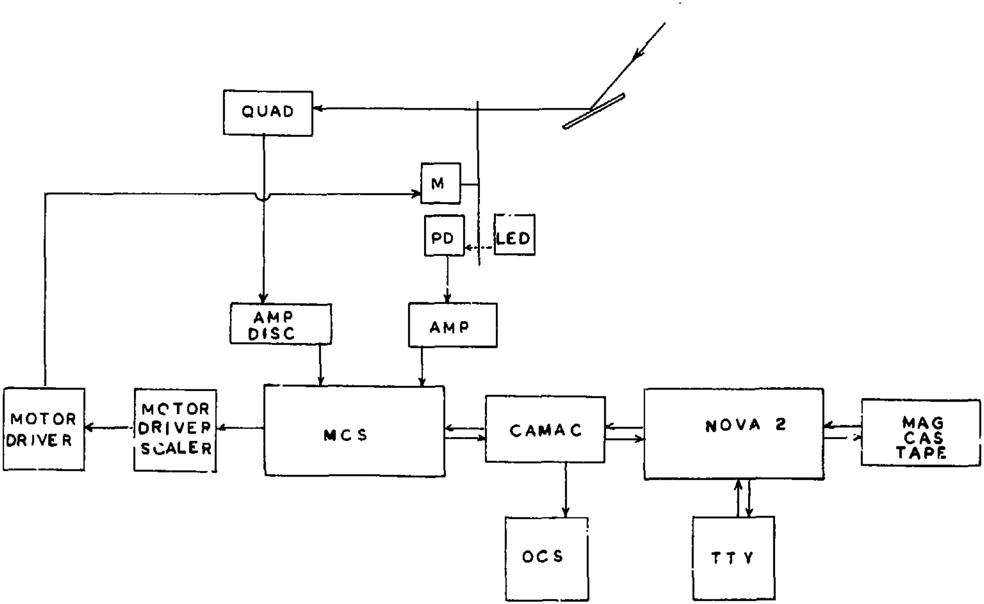

Fig. 28. Velocity distribution mode counting electronics.

XBL 799-11715

Fig. 29. Time of flight data acquisition program command flow chart. R = initialization, S = start data acquisition, B = debug routine, D = display, I = increase cycles, C = continue, P = print data on teletype, U = uncorrelated data, C = correlated data, F = full scale, H = half scale, Q = quarter scale.

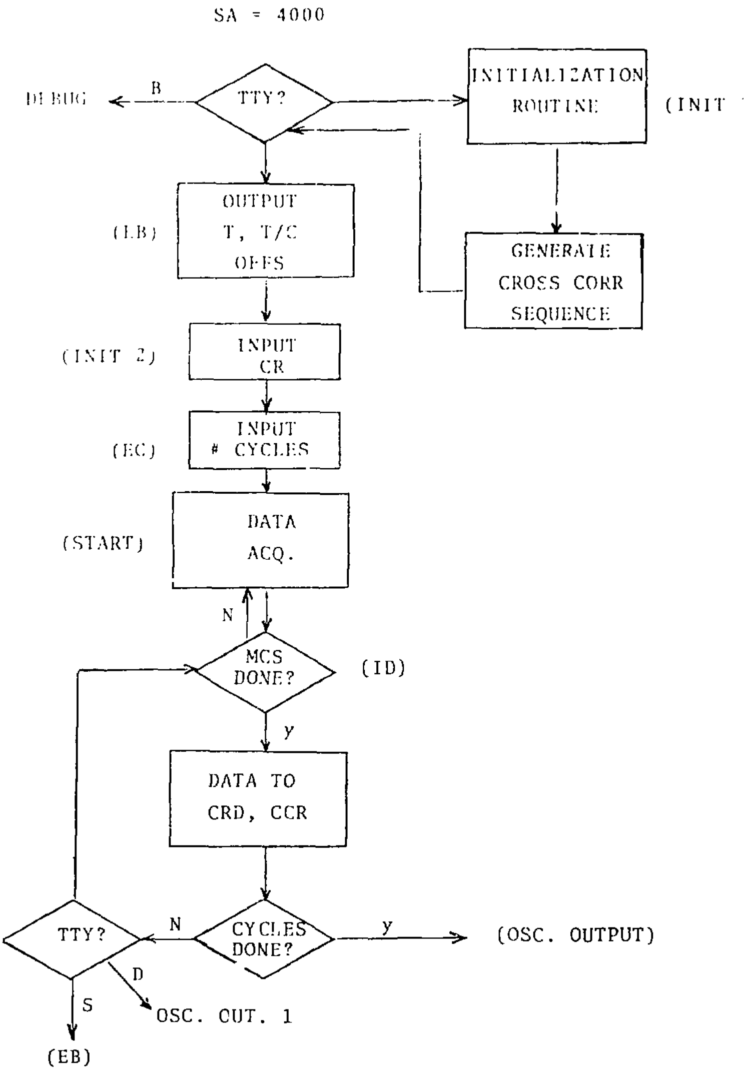
SA = 4000
DEBUG
B
TTY?
INITIALIZATION
ROUTINE
(INIT
OUTPUT
T, T/C
OFFS
(LB)
GENERATE
CROSS CORR
SEQUENCE
(INIT 2)
INPUT
CR
(EC)
INPUT
CYCLES
(START)
DATA
ACQ.
N
MCS
DONE?
(ID)
y
DATA TO
CRD, CCR
TTY?
N
CYCLES
DONE?
y
(OSC. OUTPUT)
D
S
OSC. OUT. 1
(EB)

Fig. 29a.

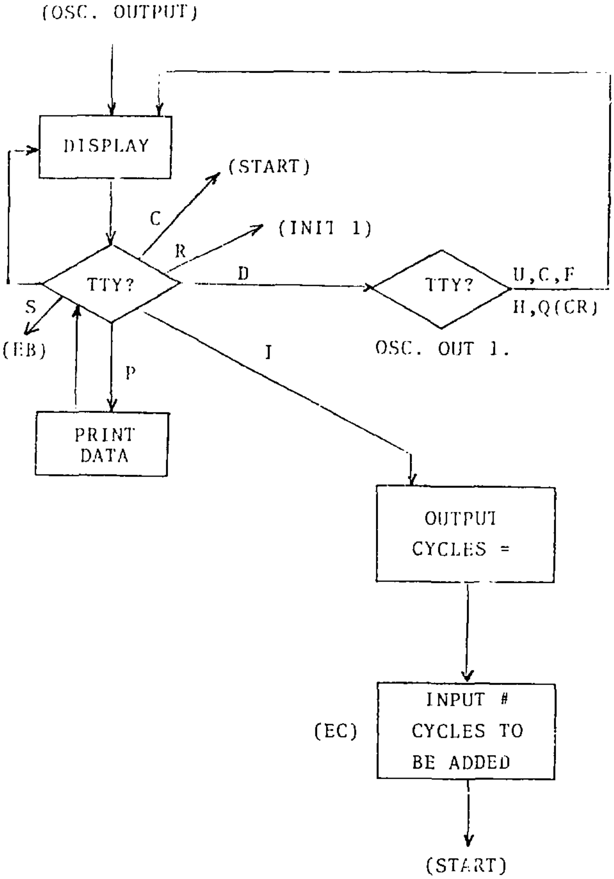
(OSC. OUTPUT)
DISPLAY
(START)
C
(INIT 1)
R
TTY?
D
TTY?
U,C,F
H,Q(CR)
S
(EB)
OSC. OUT 1.
I
P
PRINT DATA
OUTPUT CYCLES =
(EC)
INPUT # CYCLES TO BE ADDED
(START)

Fig. 29b.

```
=>R
     =>  TIME-OF-FLIGHT DATA ACQUISITION PROGRAM  <=

VERSION:08
T:
DATE (MM/DD/YY):

SRN:
T/C: 25
LP/C:9999
CC(0), SS(1) OR PLT(2): 1
OFFS:
RD (A OR B): A
D: N
OD:Y
CD:N
AUTO DC BCK SUB: N

=>S



T/C: 25
OFFS:0 A/SS
*

CYCLES = 1

=>D?
        8         8         8         7         8         8         7         7
        7         8         7         8         8         8         8         8
        8         8         8         7         7         8         7         7
        8         8         8         8         8         7         8         7
        8         7         8         8         8         8         7         7
        8         8         7         8         8         8         8         8
        7         8         7         7         7         8         8         8
        8         7         7         8         8         7         8         8
        8         8         7         7         8         7         7         7
        8         8         8         8         8         8         8         8
        7         8         8         8         8         7         8         8
        8         7         8         8         8         8         8         8
        8         8         8         8         8         7         7         8
        7         8         8         8         7         8         8         7
        8         7         8         7         8         8         8         8
        7         7         8         8         7         8         8         8
        8         7         7         8         7         7         7         8
        8         8         8         7         7         8         8         7
        8         8         8         8         7         7         8         7
        7         7         8         8         8         8         8         8
        8         8         7         8         8         8         8         7
        7         8         8         7         8         8         8         8
        7         8         8         8         8         7         8         7
        7         8         7         8         8         8         7         8
        8         8         8         7         8         7         8         8
        8         8         7         7         8         8         8         8
        8         8         8         7         7         8         7         8
        7         8         8         8         8         7         7         8
        8         7         8         8         8         8         7         7
        8         8         7         7         8         8         8         8
        8         8         8         8         7         8         8         8
        8         7         7         8         8         7         8         1

TOTAL COUNTS =     1958
```

Fig. 30. Teletype input/output for TOF Data Acquisition Program.

L. Signal Intensity Analysis

The pressures expected in each of the chambers and the intensity of the beam can be calculated as follows:

The intensity out of an effusive source ($K_n = 1$) is given as

$$I = \frac{nA\vec{v}}{4\pi} \quad \frac{P}{\text{sec sr}} \tag{15}$$

where $\vec{v} = (\frac{8kt}{\pi m})^{1/2}$ is the average velocity of the beam, m is the gas number density, and A is the area of source orifice. For a pressure 1 torr of O_2 behind the orifice at 300°K and a 1 mm diamet - orifice,

$$I = 9 \times 10^{17} \quad \frac{P}{\text{sec sr}}$$

The total amount of gas flowing into the source chamber is $I = 5.5 \times 10^{18}$ P/sec. For a pumping speed of approximately 800 l/sec (through the right angle valve, and trap to the 6" diffusion pump), the pressure in the source chamber is

$$P = \frac{5.5 \times 10^{18} \text{ P/sec}}{3.3 \times 10^{19} \text{ P/torr l} \times 800 \text{ l/sec}}$$

$$P = 1.7 \times 10^{-4} \text{ torr}$$

where 1 torr-l corresponds to 3.3×10^{19} particles at 300 K. A pressure of 1.5×10^{-4} torr is observed. The source subtends a solid angle of 4.0×10^{-4} sr with the collimating slit into the buffer chamber and an solid angle of 1.5×10^{-4} sr with the main chamber. The necessary geometry is indicated in Figs. 2-4. The beam load on the buffer chamber from the part of the beam that does not flow into the main chamber is then 2.3×10^{14} P/sec which corresponds to a pressure of 7×10^{-9} torr for a pumping speed of 1000 l/sec. There is also an additional gas load through the first collimating slit due to the background gas in the source chamber. The collision frequency of a gas with a wall is given by

$$Z = P\left(\frac{1}{2\pi mRT}\right)^{1/2} \frac{\text{moles}}{\text{cm}^2\,\text{sec}} \tag{16}$$

$$Z' = Z\,RT\ \frac{\text{torr l}}{\text{cm}^2\,\text{sec}} \quad \text{where } R = 62.3\ \frac{\text{torr l}}{\text{deg mole}} \tag{17}$$

For a background pressure of 2×10^{-4} torr in the source chamber and a 1 mm diameter hole.

$$Z' = 1.8 \times 10^{-5}\ \frac{\text{torr l}}{\text{sec}}$$

Thus

$$P_{\text{BUFF-BCK}} = \frac{1.8 \times 10^{-5}\ \text{torr l/sec}}{1000\ \text{l/sec}} = 1.8 \times 10^{-8}\ \text{torr}$$

The total pressure in the buffer chamber is

$$P_{\text{BUFF TOT}} = 1.8 \times 10^{-8} + 7 \times 10^{-9} = 2.5 \times 10^{-8} \text{ torr}$$

A pressure of 4×10^{-8} torr is observed. The intensity of the beam in the main chamber is 1.4×10^{14} P/sec and the flux at the surface is 5.4×10^{15} P/sec cm^2 calculated for a surface at a 45° angle of incident to the beam. The pressure of the main chamber due to the load of the beam is 2.8×10^{-9} torr for a pumping speed of 1500 l/sec (the titanium sublimator is not on here). The observed pressure is 1.3×10^{-9}. The sticking of O_2 by the clean walls increases the effective pumping speed. The pressure in the main chamber due to the effusive background from the differential chamber is 1.4×10^{-11} torr and from the source chamber is 4.0×10^{-12} torr. (A beam of Ar flowing into the main chamber gives a correct pressure reading.)

The O_2 scattering distribution is broad and scatters into 60° in the plane in which the detector rotates. It is assumed that the scattering distribution is cylindrically symmetric around the specular angle, thus the O_2 scatters into a solid angle of 2.6 sr. This also assumes a constant intensity over the solid angle and probably overestimates the volume into which the O_2 scatters. The scattered flux is then 5.4×10^{13} P/sec sr. The solid angle subtended by the buffer chamber of the detector is 1.4×10^{-3} sr. The required geometry is shown in Fig. 9. The pressures in the buffer chamber due to the beam and effusive background from the main chamber are 1.4×10^{-11} torr and 3.8×10^{-12} torr respectively assuming a 150 l/sec pumping speed. The solid angle subtended by the quadrupole chamber is 1.3×10^{-4} sr and the pressure in this chamber from the beam load and effusive background load from the buffer chamber and the main chamber is 1.1×10^{-12} torr, 2.3×10^{-13} torr and 8.7×10^{-13} torr for a 200 l/sec pumping speed. The flux at the ionizer is 2.1×10^{11} P/cm^2 sec which corresponds to a density of 4.8×10^{6} P/cm^3 or a pressure of 1.5×10^{-10} torr for O_2 at 300 K. The necessity of differentially pumping the detector is clear. The signal intensity is two orders of magnitude above the background in this case whereas without differential pumping it would be twenty times below it.

The O_2 scattered intensity has been measured to be 5000 counts/sec. This would correspond to a density at the detector of 3.4 P/cm^3. The total efficiency of the quadrupole mass spectrometer (ionizer and transmission of the mass filter) appears to be 7×10^{-7}. This number is somewhat misleading since the apparent ionizer efficiency can be improved substantially by decreasing the modulation frequency. The period of the 150 Hz modulation frequency employed is approximately the time constant for the pumping speed of the chambers. Use of a higher RF frequency on the quadrupole rods will increase the sensitivity of the mass filter for low mass numbers and additional lensing on the ionizer should increase the extraction efficiency.

It is desirable to increase the detection efficiency since the time required to achieve a given signal to noise ratio decreases in proportion to an increase in the counting rate. Higher pumping speed in the detector chamber is required since it could decrease the background and thus the counting time could decrease proportionately. The higher intensity available from a nozzle source as compared to effusive sources used here will increase the signal and decrease the counting time by the square of the factor that the signal increased. All of these considerations are essential to tractable counting times especially in the case of reactive scattering when the signal level can easily be three orders of magnitude below the one calculated here for O_2 inelastic scattering.

The next chapter present data for three reactive scattering systems under experimental conditions similar to ones predicted here. Typical counting rates are 3 counts/sec with a background counting rate of 1800 c/s. The total counting time is 1800 s at each point. It is clear from the above discussion that without the employment of differential pumping, a high sensitivity detector, and signal averaging that this signal could not be distinguished from the background for the large distances of the detector from the surface required for time of flight measurements.

M. References

1. M. A. Van Hove and S. Y. Tong, Surface Crystallography by LEED, Springer Verlag, Berlin, 1979.
2. H. Ibach, H. Hopster and B. Sexton, Applications of Surface Science, 1, 1 (1977).
3. L. L. Kesmodel, L. H. Dubois, and G. A. Somorjai, Chem. Phys. Lett. 56, 267 (1978).
4. T. E. Madey and J. T. Yates, Jr., Surf. Sci. 76, 397 (1978).
5. K. H. Rieder and T. Engel, Phys. Rev. Lett. 43, 373 (1979).
6. J. E. Demuth and D. E. Eastman, Phys. Rev. Lett. 32, 1123 (1974).
7. S. D. Kevan, D. H. Rosenblatt, D. Denley, B. C. Liu, and D. A. Shirley, Phys. Rev. Lett. 41, 1565 (1978).
8. H. Conrad, G. Ertl, J. Kuppers, S. W. Wang, K. Gerard and H. Haberland, Phys. Rev. Lett. 42, 1082 (1979).
9. S. J. Sibener and Y. T. Lee, Proceedings of the XI International Symposium on Rarefied Gas Dynamics, Cannes, France, 1978.
10. A. E. Dabiri, T. J. Lee and R. E. Stickney, Surf. Sci. 26, 522 (1971).
11. G. Comsa, R. David and K. D. Rendulic, Phys. Rev. Lett. 38, 775 (1977).
12. C. A. Becker, J. P. Cowin, L. Wharton and D. J. Auerbach, J. Chem. Phys. 67, 3394 (1977).
13. R. Calder and G. Lewin, Brit. J. Appl. Phys. 18, 1459 (1967).

14. R. J. Roark, Formulas for Stress and Strain, McGraw Hill, New York, 1954, p. 324.

15. V. L. Hirschy, M. S. Thesis, Florida State University, 1969.

16. V. L. Hirschy and J. P. Aldridge, Rev. Sci. Instr. 42, 381 (1971).

17. F. C. Fehsenfeld, K. M. Evenson and H. P. Broida, Rev. Sci. Instr. 36, 294 (1965).

18. P. E. Siska, J. M. Parson, T. P. Schafer and Y. T. Lee, J. Chem. Phys. 55, 5762 (1971).

19. H. S. W. Massey, Electronic and Ionic Impact Phenomena, Vol. II, Oxford University Press, London, 1969, p. 919.

20. W. L. Fite and R. T. Brackmann, Phys. Rev. 112, 1141 (1958).

21. J. R. Pierce, Theory and Design of Electron Beams, Van Nostrand, New York, 1954, p. 178.

22. M. Von Ardenne, Tabellen zur Angewandten Physik, Band I, Veb Deutschen Verlag der Wissenschaften, Berlin, 1962, p. 132.

V. THE OXIDATION OF D, D_2 AND CO ON Pt(111)

A. Introduction

The identification of reaction intermediates adsorbed on a surface is an intriguing problem in surface chemistry. One way to characterize a reaction intermediate is to employ it as the initial reactant. Molecular beam surface scattering is ideally suited for the study of reaction intermediates provided that a fairly pure beam of the reaction intermediate (radical) can be prepared. Described here is the reaction of incident D atoms in one beam with incident O_2 molecules in a second beam to form D_2O on a platinum (111) surface. The angular distribution of the D_2O product is compared to the one obtained when the initial reactants are the molecular species, D_2 and O_2. In addition, the D_2O angular distribution is compared to that of CO_2 product formed from the oxidation of CO.

B. Experimental

The apparatus is described in the previous chapter. One torr effusive beams at room temperature of D_2 and O_2 and of O_2 and CO were employed at a 50° angle of incidence to the surface. The D atom beam was formed at 1 torr in a microwave discharge which has about 80% dissociation. The D, D_2 or CO beam was modulated at 150 hz. The Pt(111) surface was at a temperature of about 425°C measured by a infra-red pyrometer for all of the reactions. Auger electron spectroscopy indicated that the surface was clean (<0.05 monolayers of C) both before and after the reactions.

C. Results and Discussion

The results are shown in Figs. 1-3. The angular distribution of D_2O obtained from the reaction of D_2 and O_2 is cosine. The angular distribution of D_2O from the D and O_2 reaction exhibits a shoulder near the specular angle on top of a cosine distribution as seen in Fig. 2. This shoulder is due to inelastic scattering of D_2O formed in the hot plasma. Subtraction of the angular distribution obtained with only the plasma on (no O_2 beam) yields a cosine distribution for the D and O_2 reaction as shown in Fig. 3.

The fact that the D_2O product from the D and O_2 reaction has a cosine distribution indicates that the incident D atom loses its kinetic energy upon hitting the surface and rattles down the deep D-Pt well coming to equilibrium with the surface before a reaction can occur. It is reasonable to assume that once the D atom has adsorbed on the surface the lowest energy pathway is followed. From the energetics in Fig. 4, the lowest energy pathway involves first the formation of an OD radical. Any adsorbed oxygen at these surface temperatures of 400°C is dissociated.[1] This is followed by addition of an adsorbed D atom to form D_2O which subsequently desorbs from the surface. The presence of OD on the surface is not consistent with the fact that no D_2O was observed at the specular angle from

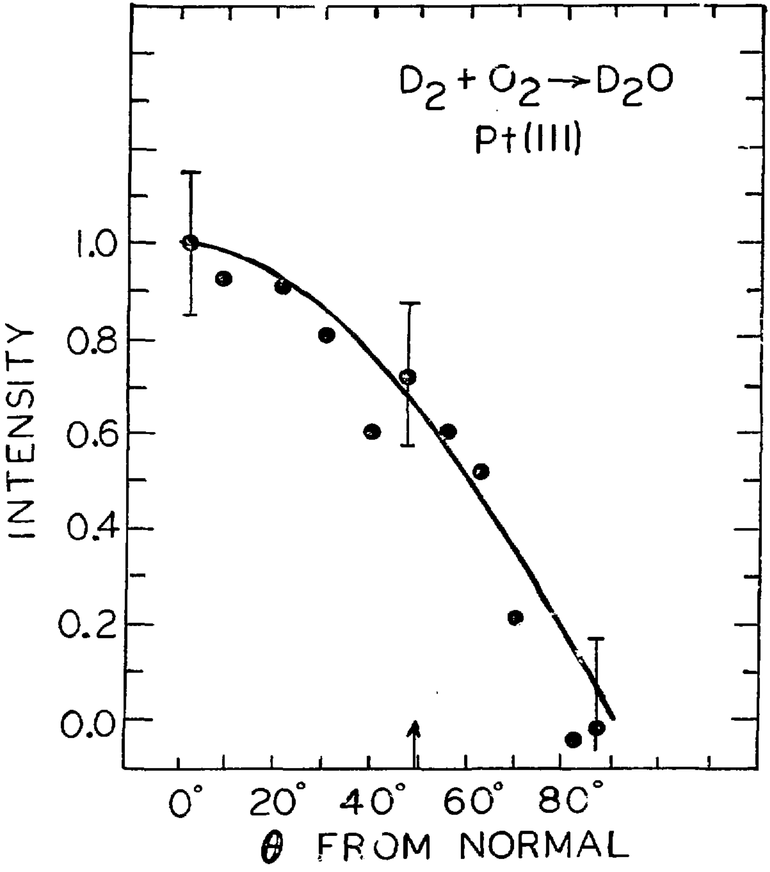

XBL 799-11675

Fig. 1. Angular distribution of D_2O from D_2 + O_2 at T_S = 425°C.

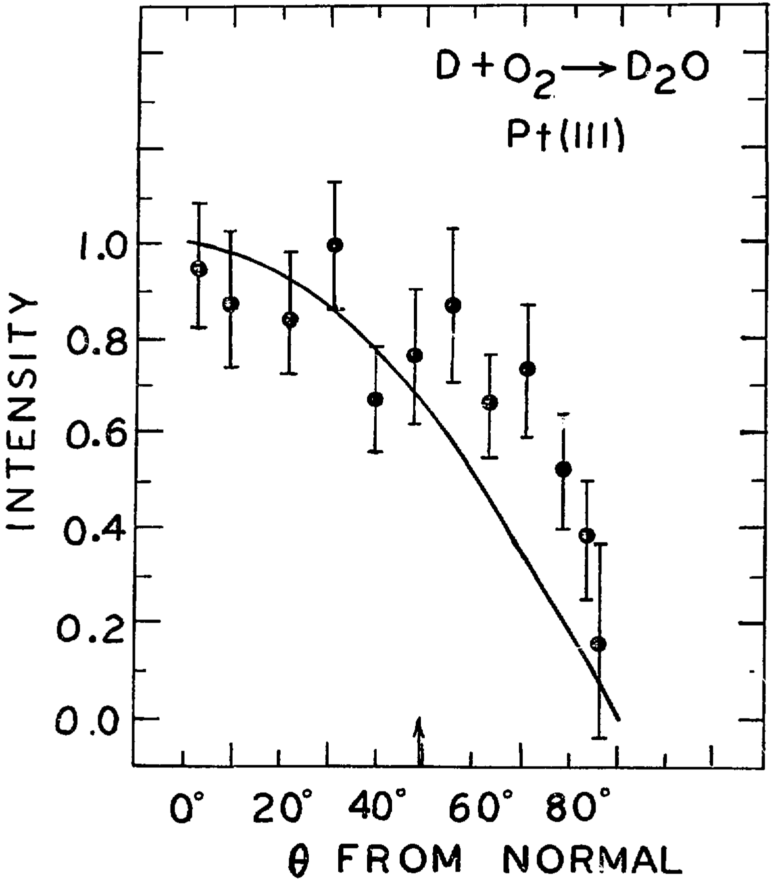

XBL 799-11677

Fig. 2. Angular distribution of D_2O from D + O_2 and D_2 + O_2 from T_S = 425°C.

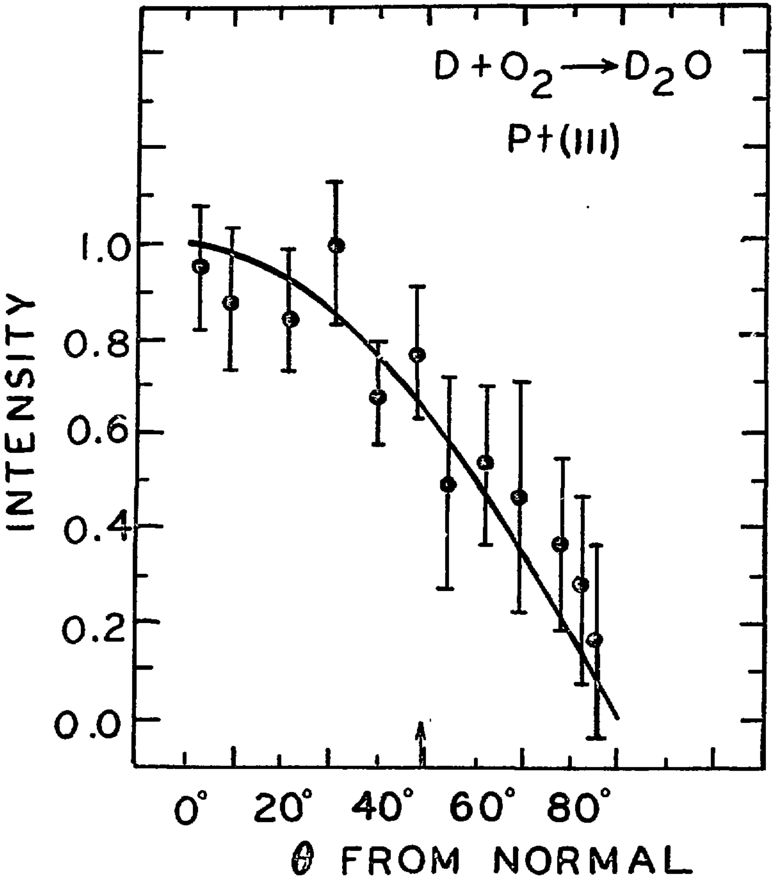

XBL 799-11676

Fig. 3. Angular distribution of D_2O from $O + O_2$ and $D_2 + O_2$ with inelastic contribution of D_2O subtracted out. The inelastic angular distribution was measured with the plasma on and no O_2 beam.

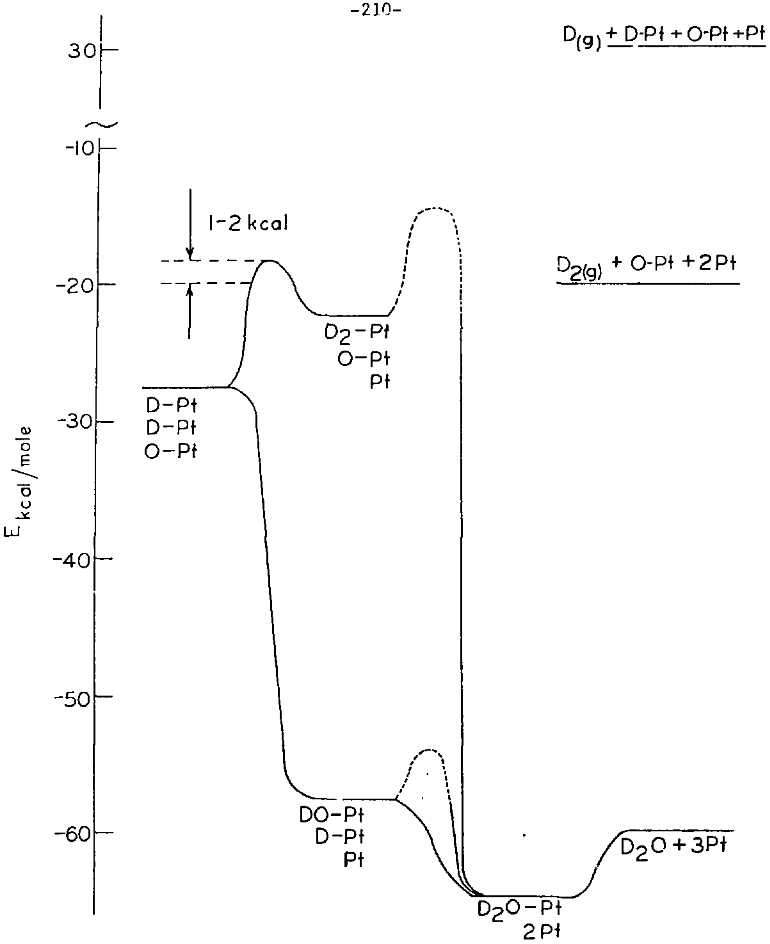

XBL 799-11761

Fig. 4. Energetics for D_2, O_2 system on Pt(111). D, O, OD and D_2O ΔH_f from reference 12. O-Pt bond energy reference 1. D-Pt and D_2-Pt bond energies from references 2 and 3. D_2O-Pt bond energy from reference 6.

the reaction $D_{(g)} + OD_{(ads)}$. Since the OD is bound to the surface through the oxygen, the oxygen is shielded from the incident O atom by the D atom to which it is bound. Thus, the D atom cannot hit the O atom to cause the reaction to occur. At more glancing incidences, this may become a more dominant mechanism leading to a peak near the specular angle in the angular distribution.

The alternate pathway in Fig. 4 involves first the formation of D_2 followed by addition of an adsorbed O atom to form D_2O. However, since $D_2(H_2)$ on Pt(111) has a well known barrier to dissociative adsorption of about 1-2 kcal/mole,[2,3] most of the recombined D_2 would fly off of the surface rather than be bound as molecularly adsorbed D_2 as long as the energy transfer between the forming D_2 molecule and the surface is slow and inefficient. In the case of incident D_2, it is possible that the remnants of the large activation energy barrier present for the ground state O atom and D_2 reaction in the gas phase exist which would prevent this reaction pathway. An isotopic exchange experiment would further clarify this point.

It is interesting to compare the D_2O angular distribution to the one obtained for CO_2 from the reaction of CO and O_2 on Pt(111) as shown in Fig. 5. The more mobile CO molecule bound to the surface through the carbon atom has to migrate to an adsorbed O atom site and has to be forced upwards out of its equilibrium position to bind to the oxygen atom in order to attain a linear configuration for the CO_2. There may well be a barrier perpendicular to the surface for this extension of the OC-Pt bond. Once past this critical configuration, the repulsive

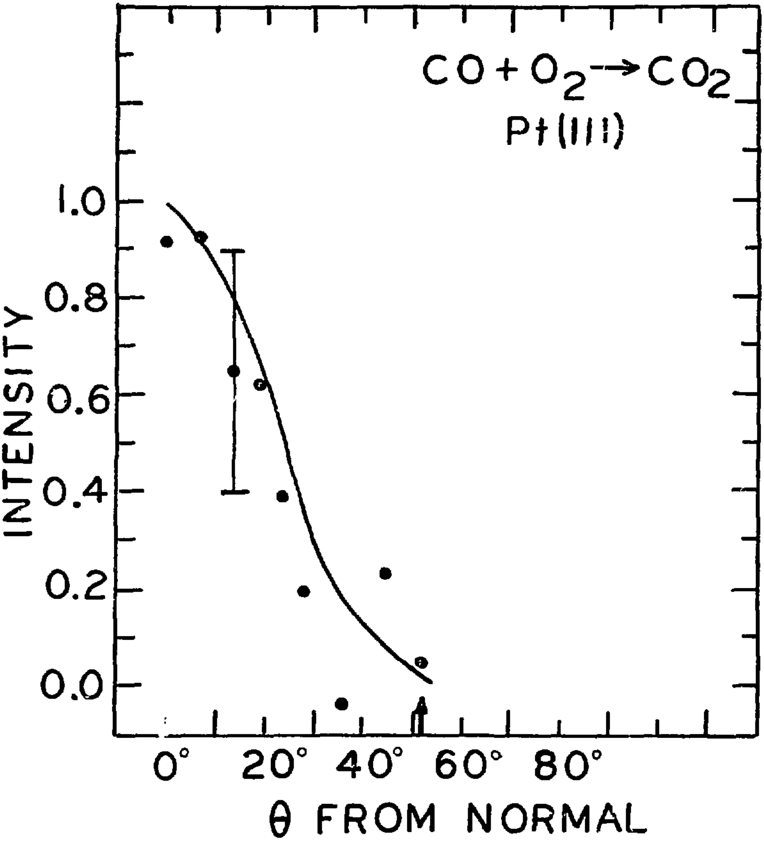

XBL 799-11690

Fig. 5. Angular distribution of CO_2 from $CO + O_2$ at $T_S = 450°C$.

interaction from descending the barrier pushes the CO_2 molecule out directly away from the surface leading to a very peaked angular distribution at the surface normal as seen here and in previous work.[4,5] The D_2O molecule, however, is bent which means that the adsorbed D atom can attack from the side of the adsorbed OD radical not requiring the OD radical to be forced upwards out of its equilibrium position. Therefore, there would be no barrier as in the case of CO_2 formation which would lead to a peaked angular distribution.

It is also possible that the very peaked angular distribution for CO_2 arises from vibrational excitation due to the deformation of the CO_2 molecule as the OC=O bond is being formed. The CO_2 molecule having lots of internal energy would push itself away from the surface in a normal direction. Because D_2O is a bent molecule, no internal excitation would be developed in the transition state. The D_2O molecule would not have a preferred direction for desorption.

This discussion involves reactant species which are adsorbed on the surface. There are many arguments in the literature for both the oxidation of CO and H_2 over whether the reaction mechanism is one involving adsorbed species (Langmuir-Hinshelwood mechanism) or one involving an adsorbed species and a gas phase species (Eley-Rideal mechanism).[5-11] The angular distributions for these systems show that the Eley-Rideal mechanism which would not involve a long lived complex is incorrect since there is no indication of a peak at the specular angle.

Velocity distribution measurements currently in progress will help clarify the nature of the potential energy surface in the exit channel region for this reaction. For example, if the $D_2O_{(g)}$ molecule and the DO-Pt adsorbate do have the relative energy levels shown in Fig. 4 (the DO-Pt bond strength is estimated as less strong than the O-Pt bond and the D_2O-Pt as 5 kcal smaller than an experimental value of D_2O on Pt(100)) then with or without the exit channel barrier the D_2O product should come off the surface at temperatures substantially above the temperature of the surface. If the OD radical is bound more strongly by 3 kcal than the value indicated in Fig. 4 then the D_2O molecule formed can be trapped in its well and equilibrate with the surface. Nevertheless, by comparing the product angular distributions for both the atomic and molecular incident species, it appears that the D atom and thus the OD radical, whether bound or a transient, are important surface reaction intermediates during the oxidation of D_2.

D. References

1. J. L. Gland, submitted to Surface Science, 1979.
2. K. E. Lu and R. R. Rye, Surf. Sci. 45, 677 (1974).
3. K. Christmann and G. Ertl, Surf. Sci. 60, 365 (1976).
4. C. A. Becker, J. P. Cowin, L. Wharton and D. J. Auerbach, J. Chem. Phys. 67, 3394 (1977).
5. R. L. Palmer and J. N. Smith, Jr., J. Chem. Phys. 60, 1453 (1974).
6. F. P. Netzer and G. Kneringer, Surf. Sci. 51, 526 (1975).
7. R. A. Shigeishi and D. A. King, Surf. Sci. 75, L397 (1978).
8. D. M. Collins, J. B. Lee and W. E. Spicer, Phys. Rev. Lett. 35, 592 (1975).
9. J. N. Smith, Jr. and R. L Palmer, J. Chem. Phys. 56, 13 (1972).
10. J. A. Strozier, Jr., G. J. Cosgrove and D. A. Fischer, Surf. Sci. 82, 481 (1979).
11. R. E. Lagos, B. C. Scales and H. Suhl, Surf. Sci. 82, 525 (1979).
12. K. S. Pitzer and L. Brewer, Thermodynamics, McGraw-Hill, New York, 1961, p.672.
13. K. Christmann, G. Ertl and T. Pignet, Surf. Sci. 54, 365 (1976).

Appendix A. Program Balance

This program calculates the x and y positions of a 1 sq. in. area hole required to balance a wheel which has any m = 255 sequence of slots cut radically along its periphery A correction for the larger trigger slot is included. The input variables are as follows

R2 radius of the wheel

R1 radius to the bottom of the slot

RT radius to the bottom of the trigger slot

M(I) I = 1, 255 the m - sequence

M(I) = 0 is a tab

M(I) = 1 is a slot

The coordinate system is defined such that the trigger slot is M(1) with the sequence proceeding in a counter clockwise direction through the first quadrant. If a hole other than unit area is desired the coordinates are

$$X' = \frac{X}{A} \qquad y' = \frac{Y}{A}$$

where A is the area of the hole.

```
73/07/07 UNIVERSITY OF MINNESOTA 7600 FORTRAN COMPILER   DAY  7.0.0  PSR12      01 APR 75 19.07.21
           MNF.
 000477B         1*          PROGRAM SYLVIA (INPUT,OUTPUT,TAPE5=INPUT,TAPE6=OUTPUT)
 001144B         2*          DIMENSIONM(255)
 001144B         3*          READ(5,100)(M(I),I=1,255)
 001354B         4*          READ(5,200)R2,R1,RT
 001363B         5*          RN=(R1+R2)/2.
 001365B         6*          AN=.01232*(R2**2-R1**2)
 001367B         7*          ANT=.01232*(R2**2-RT**2)
 001372B         8*          RNT=(RT+R2)/2.
 001374B         9*          AX=0.0
 001375B        10*          AY=0.0
 001375B        11*          DO 1 I=1,255
 001377B        12*          T=.02464*FLOAT(I-1)
 001400B        13*          EMI=M(I)
 001402B        14*          IF (T)3,2,3
 001404B        15*  2       AX=AX-EMI*ANT*RNT*COS(T)
 001413B        16*          GO TO 4
 001413B        17*  3       AX=AX-EMI*AN*RN*COS(T)
 001422B        18*  4       AY=AY-EMI*AN*RN*SIN(T)
 001431B        19*  1       CONTINUE
 001434B        20*          WRITE(6,300) AX,AY
 001342B        21*  100     FORMAT (80I1)
 001342B        22*  200     FORMAT(3F10.4)
 001342B        23*  300     FORMAT(*AX= *,F10.4, * AY= *,F10.4)
 001342B        24*          STOP
 001444B        25*          END
```

Appendix B. Ion/Electron Trajectory Program

The electrostatic field is calculated in program JASON. It is described in detail in a Lawrence Livermore Laboratory report #UCID-17814 entitled JASON - A Code for Solving General Electrostatics Problems - User's Manual.

The program EXRAY uses the electrostatic field calculated by JASON as input and tracks the trajectory of a charged particle in this field given its initial position, energy, trajectory angles, charge and mass. The charge and mass of an electron should not be specified. A subset of the JASON mesh specifying the area in which the trajectory is to be tracked must also be specified. The order and format of the input is discussed in the comment cards of the listing. A sample output plot is shown in Fig. 26 Chapter IV.

```
          PROGRAM XRAY(INPUT,OUTPUT,JSNDMP,PLOT                          XRAY.2
        +,TAPE5=INPUT,TAPE6=OUTPUT,TAPE1=JSNDMP,TAPE99=PLOT,TAPE98)      XRAY.3
C                                                                        XRAY.4
C [illegible] FORMAT OF JASON DUMP FILE,JSNDMP, 11/1/76                  XRAY.5
C                                                                        XRAY.6
                                                                         XRAY.7
      COMMON  CM(20000)                                                  XRAY.8
                                                                         XRAY.9
      COMMON /FIELD / XC,YC,PX,PY,FF(4),TT(100)                          XRAY.10
      COMMON / [illegible] / KLOT                                        XRAY.11
      COMMON / INTSN / XS,YE,FX,EY                                       XRAY.12
      COMMON / [illegible] / K,DELX,DELY                                 XRAY.13
      COMMON / DATAP / XPL(300),YPL(300)                                 XRAY.14
      COMMON / PTPLT / KPL                                               XRAY.15
      COMMON /LIMIT/ XMIN,XMAX,YMIN,YMAX,CC(4),INC                       XRAY.16
      COMMON / PARAM / EMINV,E0,T4                                       XRAY.17
      COMMON / CSIZE / KMAX,LMAX,KXL                                     XRAY.18
      DIMENSION [illegible](4)                                           XRAY.19
      EQUIVALENCE ([illegible],YL)                                       XRAY.20
                                                                         XRAY.21
      [illegible]                                                        XRAY.22
      [illegible]                                                        XRAY.23
      DATA [illegible] / [illegible] /                                   XRAY.24
C     ELECTRON CHARGE IN ESU, ELECTRON MASS IN GRAMS.                    XRAY.25
      DATA [illegible]/-4.803E-10,9.1091E-28/                            XRAY.26
C     CONVERSION FACTOR, EV TO ERGS.                                     XRAY.27
      DATA [illegible]/1.6021E-12/                                       XRAY.28
C     CONVERSION FACTOR, DEGREES TO RADIANS.                             XRAY.29
      DATA [illegible] / 0.017453292519943 /                             XRAY.30
C                                                                        XRAY.31
C [illegible] PARTICLES IN A NON UNIFORM QUADRILATERAL MESH.             XRAY.32
C FIELD VALUES FROM JASON ARE ASSUMED TO BE VOLTS PER CENTIMETRE. THESE  XRAY.33
C ARE CONVERTED TO STATVOLTS PER CENTIMETRE BY SUBROUTINE FILLUP FOR     XRAY.34
C USE IN XRAY.                                                           XRAY.35
C                                                                        XRAY.36
C THE FIRST DATA CARD SPECIFIES A WINDOW, A SUBSET OF THE JASON MESH TO XRAY.37
C BE USED. FILLUP USES THESE VALUES AND REPLACES THEM WITH THE PLOT SCXRAY.38
C [illegible] PLOT PARAMETERS ARE ALSO SET BY FILLUP.                    XRAY.39
C THE JASON DUMP FILE, JSNDMP, IS READ BY FILLUP.                        XRAY.40
C                                                                        XRAY.41
      READ 1000,XMIN,XMAX,YMIN,YMAX                                      XRAY.42
 1000 FORMAT(4F10.3)                                                     XRAY.43
      CALL FILLUP                                                        XRAY.44
  100 CONTINUE                                                           XRAY.45
      [illegible]                                                        XRAY.46
      [illegible]                                                        XRAY.47
      [illegible] = 1.0E-10                                              XRAY.48
C READ THE PARTICLES INITIAL COORDINATES IN CENTIMETRES, ITS ENERGY IN   XRAY.49
C EV, ITS INITIAL Y ANGLE IN DEGREES, ITS CHARGE IN ESU, AND ITS MASS    XRAY.50
C IN GRAMS.                                                              XRAY.51
      READ 2,[illegible],TD,TDEL,TCM                                     XRAY.52
    2 FORMAT(6E12.3)                                                     XRAY.53
      IF(EOF(5)) 101,102                                                 XRAY.54
  102 CONTINUE                                                           XRAY.55
      IF([illegible] .LT. 0) GO TO 10                                    XRAY.56
      IF([illegible]) EQ=TQ                                              XRAY.57
      IF([illegible]) EM=TEM                                             XRAY.58
```

```
                                                   FTN 4.6+439/04J    28 FEB 77 08.36.54  BKY PAGE    2

            [illegible]                                              XRAY.59
            [illegible]                                              XRAY.60
            [illegible]                                              XRAY.61
            [illegible]                                              XRAY.62
            [illegible]                                              XRAY.63
            [illegible]                                              XRAY.64
            [illegible]                                              XRAY.65
            [illegible]                                              XRAY.66
            [illegible]                                              XRAY.67
            [illegible]                                              XRAY.68
            [illegible]                                              XRAY.69
            [illegible]                                              XRAY.70
            [illegible]                                              XRAY.71
                                                                     XRAY.72
            [illegible]                                              XRAY.73
            [illegible]                                              XRAY.74
                                                                     XRAY.75
            [illegible]                                              XRAY.76
            [illegible]                                              XRAY.77
            [illegible]                                              XRAY.78
            [illegible]                                              XRAY.79
            [illegible]                                              XRAY.80
            [illegible]                                              XRAY.81
            [illegible]                                              XRAY.82
            [illegible]                                              XRAY.83
            [illegible]                                              XRAY.84
            [illegible]                                              XRAY.85
            [illegible]                                              XRAY.86
            [illegible]                                              XRAY.87
            [illegible]                                              XRAY.88
            [illegible]                                              XRAY.89
            [illegible]                                              XRAY.90
            [illegible]                                              XRAY.91
                                                                     XRAY.92
            [illegible]                                              XRAY.93
            [illegible]                                              XRAY.94
            [illegible]                                              XRAY.95
            [illegible](L,YPL,XPL)                                   XRAY.96
                                                                     XRAY.97
            [illegible]                                              XRAY.98
            [illegible]                                              XRAY.99
            [illegible]                                              XRAY.100
            [illegible]                                              XRAY.101
```

```
SUBROUTINE DERIVE    74/74    OPT=1                          FTN 4.6+439/043    28 FEB 77 08.36.54  BKY PAGE     1

      SUBROUTINE DERIVE                                                          XRAY.102
                                                                                 XRAY.103
      COMMON  XS([illegible]),YS(5[illegible]),VX(5020),VY(5020)                 XRAY.104
      COMMON /[illegible]/[illegible],XMAX,YMIN,YMAX,[illegible]                 XRAY.105
      COMMON  /  FIELD  /  X,Y,PX,PY,DX,DY,DPX,DPY                               XRAY.106
      COMMON  /  UNITS  /  N,ICT                                                 XRAY.107
      COMMON  /  [illegible]  /  [illegible]                                     XRAY.108
      COMMON  /  INTER  /  XX,YY,EX,EY                                           XRAY.109
      COMMON  /  WHERE  /  K                                                     XRAY.110
                                                                                 XRAY.111
                                                                                 XRAY.112
      ICUT = -1                                                                  XRAY.113
                                                                                 XRAY.114
      XX = X                                                                     XRAY.115
      YY = Y                                                                     XRAY.116
                                                                                 XRAY.117
      IF(XX .GT. XMAX) RETURN                                                    XRAY.118
      IF(XX .LT. XMIN) RETURN                                                    XRAY.119
      IF(YY .GT. YMAX) RETURN                                                    XRAY.120
      IF(YY .LT. YMIN) RETURN                                                    XRAY.121
                                                                                 XRAY.122
      CALL FIN[illegible](XX,YY,K)                                               XRAY.123
                                                                                 XRAY.124
      EX = VX(K)                                                                 XRAY.125
      EY = VY(K)                                                                 XRAY.126
      TST = EX*EX+EY*EY                                                          XRAY.127
      TST = SQRT(TST)                                                            XRAY.128
      IF(TST .LT. 1.E-8) RETURN                                                  XRAY.129
      ICUT = 1                                                                   XRAY.130
                                                                                 XRAY.131
      DX = [illegible]INV                                                        XRAY.132
      DY = EY[illegible]INV                                                      XRAY.133
      [illegible]                                                                XRAY. 34
      [illegible]                                                                XRAY.135
                                                                                 XRAY.136
      RETURN                                                                     XRAY.137
      END                                                                        XRAY.138
```

```
[illegible]        [illegible] OPT=1                        FTN 4.6+433/040     28 FEB 77  08.36.54$ BKY PAGE     1

      SUBROUTINE FIND(P,Q,K)                                                      XRAY.139
                                                                                  XRAY.140
      COMMON X(5000),Y(5000)                                                      XRAY.141
                                                                                  XRAY.142
      COMMON / NSIZE / KMAX, LMAX, KXL                                            XRAY.143
                                                                                  XRAY.144
      [illegible] KA([illegible]),S[illegible]                                    XRAY.145
      [illegible] A1,A2,B1,B2,C1,C2,D1,D2                                         XRAY.146
      [illegible]                                                                 XRAY.147
      [illegible] / [illegible] 1 /                                               XRAY.148
                                                                                  XRAY.149
      [illegible] = 1                                                             XRAY.150
      [illegible] =                                                               XRAY.151
      [illegible] =                                                               XRAY.152
      [illegible] =                                                               XRAY.153
    2 [illegible]                                                                 XRAY.154
      IF([illegible] .EQ. [illegible]) K=K-1                                      XRAY.155
      [illegible] GO TO 7                                                         XRAY.156
      [illegible]                                                                 XRAY.157
      [illegible]                                                                 XRAY.158
      [illegible] = [illegible] + KMAX                                            XRAY.159
      IF([illegible].KXL) GO TO 70                                                XRAY.160
      [illegible] + KMAX                                                          XRAY.161
                                                                                  XRAY.162
      A1 = [illegible] - DBLE(X(KB)+X(KD))                                        XRAY.163
      [illegible] - DBLE(Y(KA)+Y([illegible]))                                    XRAY.164
      [illegible] - DBLE(X(KA)+X([illegible]))                                    XRAY.165
      [illegible] - DBLE(Y(KA)+Y([illegible]))                                    XRAY.166
      [illegible] - DBLE(X(KA)+X([illegible]))                                    XRAY.167
      [illegible] - DBLE(Y(KA)+Y(KB))                                             XRAY.168
      [illegible]+X(KC)+X(KD)) - DBLE(4.*P)                                       XRAY.169
      [illegible]+Y(KC)+Y(KD)) - DBLE(4.*Q)                                       XRAY.170
                                                                                  XRAY.171
      [illegible] - A1                                                            XRAY.172
      [illegible] - A2                                                            XRAY.173
      [illegible] - C1                                                            XRAY.174
      [illegible] - C2                                                            XRAY.175
      [illegible] + D1                                                            XRAY.176
      [illegible] + D2                                                            XRAY.177
                                                                                  XRAY.178
      D = [illegible] - AB*BA                                                     XRAY.179
      [illegible]((CA*BB - CB*BA)/D)                                              XRAY.180
      [illegible]((AA*CB - AB*CA)/D)                                              XRAY.181
      IF([illegible] .LE. ONE .A. ABS(Q) .LE. ONE) RETURN                         XRAY.182
                                                                                  XRAY.183
      [illegible]                                                                 XRAY.184
      IF([illegible] .GT. 2) IF=IF/2                                              XRAY.185
      JF = Q                                                                      XRAY.186
      IF([illegible] .GT. 2) JF=JF/2                                              XRAY.187
      JF = JF*KMAX                                                                XRAY.188
                                                                                  XRAY.189
      KA = KA + IF + JF                                                           XRAY.190
      IF([illegible] K) RETURN                                                    XRAY.191
      [illegible] + 1                                                             XRAY.192
      [illegible] = NSUM + K                                                      XRAY.193
      IF([illegible]) GO TO 2                                                     XRAY.194
      [illegible] = K                                                             XRAY.195
```

```
[illegible]        [illegible]                    FTN 4.6+439/040     20 FEB 77 08.36.54$ SKY PAGE      2

              [illegible] = [illegible] + [illegible]                    XRAY.196
            2 CONTINUE                                                   XRAY.197
              [illegible] = [illegible]                                  XRAY.198
              IF([illegible] .GT. 2[illegible] GO TO 1                   XRAY.199
              [illegible]                                                XRAY.200
              [illegible]                                                XRAY.201
              [illegible]                                                XRAY.202
              [illegible]                                                XRAY.203
              [illegible] = -1                                           XRAY.204
              IF([illegible] .LT. 2[illegible]) GO TO 1                  XRAY.205
              [illegible] = 1.[illegible]                                XRAY.206
              DO [illegible] J=1,[illegible]                             XRAY.207
              IF(S[illegible](J) .GT. [illegible]) GO TO 66              XRAY.208
              [illegible] = S[illegible](J)                              XRAY.209
              [illegible] = [illegible](J)                               XRAY.210
           66 [illegible]                                                XRAY.211
                                                                         XRAY.212
              [illegible]                                                XRAY.213
                                                                         XRAY.214
           [illegible] [illegible] 76                                    XRAY.215
              [illegible]                                                XRAY.216
              [illegible]                                                XRAY.217
           76 [illegible] TRACKING TERMINATED BY INDEX OUT OF RANGE*)    XRAY.218
              END                                                        XRAY.219
```

```
      SUBROUTINE FILTOR
C-----------------------------------------------
C     [illegible]=(X,Y)  [illegible]
C     [illegible]=(X,Y)  IN [illegible]
C     *
C     *
C     *
C     *
C (Y) *
C     *
C     ***************************
C        L  (X)
C
C     XC(K)= X [illegible] CENTER OF [illegible] ELEMENT K
C     YC(K)= Y [illegible] CENTER OF [illegible] ELEMENT K
C     [illegible]
C     [illegible]
C     [illegible]
C     [illegible]
C     [illegible]
C-----------------------------------------------
      COMMON [illegible]
      COMMON  /  XSIZE  /  [illegible]
      COMMON  /  [illegible]  /  [illegible]
      COMMON  /  [illegible]  /  [illegible]
      [illegible]
      [illegible]
      [illegible]
C**********************************************************
C WARNING [illegible] SPECIFIED [illegible] COMMON BLOCKS TO BE
C BY [illegible] MUST BE DEFINED IN EXACTLY THIS ORDER
      [illegible]
      [illegible]
      [illegible]
      [illegible]
      [illegible]
      [illegible]
      [illegible]
C**********************************************************
      COMMON [illegible]
      EQUIVALENCE (E,[illegible])
      EQUIVALENCE (Q,AQ(455)),(P,AQ(632))
      DIMENSION [illegible](1),P(1),F(5,22))
      LEVEL 2,XB
      [illegible]/XB(1)
C CONVERSION FACTOR, VOLTS TO STATVOLTS.
      DATA [illegible]
C
      REWIND 1
      [illegible]=1
      CALL [illegible]
      BUFFER IN([illegible])([illegible])
      IF(UNIT([illegible]))210,200,210
  200 [illegible]
      CALL EXIT
```

```
  210 CONTINUE                                                  XRAY.277
      LXM2=LXM+LXM                                              XRAY.278
      LXM4=LXM2+LXM2                                            XRAY.279
      CALL SFIELD(LXM4,0,MASK(1))                               XRAY.280
      BUFFER IN(1,1)(XJ(1),XJ(LXM4))                            XRAY.281
      IF(UNIT(1))230,200,230                                    XRAY.282
  230 CONTINUE                                                  XRAY.283
      CALL SKIPFIL(5(TAPE1,1)                                   XRAY.284
      ICT = 0                                                   XRAY.285
      LXM=LJASCN                                                XRAY.286
      KM=LYJASCN                                                XRAY.287
C     ---------------------------------------------------       XRAY.288
      KAX=LXM-KM                                                XRAY.289
      KAY=LXM2-KM                                               XRAY.290
      DO 11 L=1,MMX1                                            XRAY.291
C     TIME(1)-AT(2043)=.43 SEC = 3773 OCTAL                     XRAY.292
      BUFFER IN(1,1)(AB(1),AB(2043))                            XRAY.293
      IF(UNIT(1))310,200,310                                    XRAY.294
  310 CONTINUE                                                  XRAY.295
      KAX=KAX+KM                                                XRAY.296
      KAY=KAY+KM                                                XRAY.297
      IF(III .GT. 0) GO TO 6                                    XRAY.298
      DO 3 K=1,KM                                               XRAY.299
      IF(XJ(K+KAY).GE.YMIN) GO TO 4                             XRAY.300
    3 CONTINUE                                                  XRAY.301
      GO TO 11                                                  XRAY.302
                                                                XRAY.303
    4 CONTINUE                                                  XRAY.304
      DO 5 K=1,KM                                               XRAY.305
      IF(XJ(K+KAX).LE.XMIN) KMIN=K                              XRAY.306
      IF(XMAX.GE.XJ(K+KAX)) KMAX=K                              XRAY.307
    5 CONTINUE                                                  XRAY.308
      KMM = KMIN                                                XRAY.309
      IF(KMIN .NE. 1) KMIN=KMIN-1                               XRAY.310
      KSIZ = KMAX-KMIN+1                                        XRAY.311
      IMIN = L                                                  XRAY.312
      III = 1                                                   XRAY.313
      M = 0                                                     XRAY.314
      GO TO 9                                                   XRAY.315
                                                                XRAY.316
    6 CONTINUE                                                  XRAY.317
      DO 7 K=KMIN,KMAX                                          XRAY.318
      IF(XJ(K+KAY).LT.YMAX) GO TO 9                             XRAY.319
    7 CONTINUE                                                  XRAY.320
      DO 8 I=KMIN,KMAX                                          XRAY.321
      M = M + 1                                                 XRAY.322
      EX(M) = 1.E-9                                             XRAY.323
      EY(M) = 1.E-9                                             XRAY.324
      X(M)=XJ(I+KAX)                                            XRAY.325
      Y(M)=XJ(I+KAY)                                            XRAY.326
    8 CONTINUE                                                  XRAY.327
      GO TO 12                                                  XRAY.328
                                                                XRAY.329
    9 CONTINUE                                                  XRAY.330
      M = M + 1                                                 XRAY.331
      EX(M) = 1.E-9                                             XRAY.332
      EY(M) = 1.E-9                                             XRAY.333
```

```
SUBROUTINE FILLUP     [illegible] OPT=1                  FTN 4.6+439/940    28 FEB 77 06.36.54  BKY PAGE      3

              X(M)=XJ(KMIN+KAX)                                          XRAY.334
              Y(M)=XJ(KMIN+KAY)                                          XRAY.335
              DO 10 I=KMIN,KMAX                                          XRAY.336
              M = M + 1                                                  XRAY.337
              X(M)=XJ(I+KAX)                                             XRAY.338
              Y(M)=XJ(I+KAY)                                             XRAY.339
              IF(L-[illegible](E(1,I)))207,209                           XRAY.340
          207 EX(M)=1.E-9                                                XRAY.341
              EY(M)=1.E-9                                                XRAY.342
              GO TO 10                                                   XRAY.343
          209 EX(M)=-E(1,I)/VTSV                                         XRAY.344
              EY(M)=-E(2,I)/VTSV                                         XRAY.345
           10 CONTINUE                                                   XRAY.346
              EX(M) = 1.E-9                                              XRAY.347
              EY(M) = 1.E-9                                              XRAY.348
           11 CONTINUE                                                   XRAY.349
        C     -----------------------------------------------------------XRAY.350
              M = M - KSIZ                                               XRAY.351
              DO 411 I=KMIN,KMAX                                         XRAY.352
              M = M + 1                                                  XRAY.353
              EX(M) = 1.E-9                                              XRAY.354
              EY(M) = 1.E-9                                              XRAY.355
          411 CONTINUE                                                   XRAY.356
                                                                         XRAY.357
           12 CONTINUE                                                   XRAY.358
              KMAX = KSIZ                                                XRAY.359
              LMAX = L - LMIN + 1                                        XRAY.360
              NPL = KMAX*LMAX                                            XRAY.361
              IF(NPL.LT.SMALL) GO TO 13                                  XRAY.362
              PRINT 553                                                  XRAY.363
              CALL EXIT                                                  XRAY.364
           13 CONTINUE                                                   XRAY.365
              XMIN = 1.E9                                                XRAY.366
              YMIN = 1.E9                                                XRAY.367
              XMAX = -XMIN                                               XRAY.368
              YMAX = -XMIN                                               XRAY.369
              LN = LMAX - 1                                              XRAY.370
              KM = KMAX - 1                                              XRAY.371
              KL = 1                                                     XRAY.372
              KT = KM                                                    XRAY.373
              LM = 1                                                     XRAY.374
              LT =(LM-1)*KMAX + 1                                        XRAY.375
              DO 14 I=1,LM                                               XRAY.376
              IF(X(KL) .LT. XMIN) XMIN=X(KL)                             XRAY.377
              IF(X(KT) .GT. XMAX) XMAX=X(KT)                             XRAY.378
              KT = KT + KMAX                                             XRAY.379
              KL = KL + KMAX                                             XRAY.380
           14 CONTINUE                                                   XRAY.381
              DO 15 I=1,KM                                               XRAY.382
              IF(Y(LM) .LT. YMIN) YMIN=Y(LM)                             XRAY.383
              IF(Y(LT) .GT. YMAX) YMAX=Y(LT)                             XRAY.384
              LM = LM + 1                                                XRAY.385
              LT = LT + 1                                                XRAY.386
           15 CONTINUE                                                   XRAY.387
              DELX = (XMAX-XMIN)/(KMAX-2)                                XRAY.388
              DELY = (YMAX-YMIN)/(LMAX-2)                                XRAY.389
                                                                         XRAY.390
```

```
            XXL = XX(2) - XX(1)                                            XRAY.391
            XXM = XX(4) - XX(3)                                            XRAY.392
            CC(1) = 1.0.                                                   XRAY.393
            CC(2) = CC(1)                                                  XRAY.394
            CC(3) = 1.50.                                                  XRAY.395
            CC(4) = CC(3)                                                  XRAY.396
            IF(XXL.LT.XXM) GO TO 16                                        XRAY.397
            CC(2) = CC(1) + 900.*(XXL/XXM)                                 XRAY.398
            GO TO 16                                                       XRAY.399
         15 CC(4) = CC(3) + 500.*(XXM/XXL)                                 XRAY.400
         16 CONTINUE                                                       XRAY.401
            CALL CFGRID(6HACLPLS)                                          XRAY.402
            NEWPEN 1                                                       XRAY.403
            INC=0                                                          XRAY.404
            DO 20 J=1,NN                                                   XRAY.405
            CALL ...(1,1)(BNDRY,NPT)                                       XRAY.406
            IF(BNDRY(1))21,22,22                                           XRAY.407
         22 CONTINUE                                                       XRAY.408
            CALL CURLST(BNDRY(3),BNDRY(4),NPT)                             XRAY.409
            CALL CURLST(BNDRY(3),BNDRY(4),NPT)                             XRAY.410
         20 CONTINUE                                                       XRAY.411
            INI=1                                                          XRAY.412
         21 RETURN                                                         XRAY.413
        501 FORMAT(//* EOF ENCOUNTERED WHILE READING JASON DUMPFILE*)      XRAY.414
        503 FORMAT(//* TRACKING REGION GREATER THEN 5000 POINTS*)          XRAY.415
            END                                                            XRAY.416
```

```
      SUBROUTINE ZAM(X,SWPR)                                           XRAY.448
                                                                       XRAY.449
      COMMON  /  FIELD  /  Y(4),F(4),T(8,4)                            XRAY.450
      COMMON  /  UNITS  /  KOUT                                        XRAY.451
      COMMON /INIC/ IPMX,AREF,EMAX,SSSR,HFAC,SWAM,SWEX                 XRAY.452
      COMMON /INTP/ HPR,XX,N,EUB,ELB,IP,IT,NPKS,SWIN                   XRAY.453
                                                                       XRAY.454
      LOGICAL SWAM,SWEX,SWIN                                           XRAY.455
      LOGICAL SWPR                                                     XRAY.456
      INTEGER HFAC                                                     XRAY.457
      DOUBLE PRECISION T,HPR,XX                                        XRAY.458
      DOUBLE PRECISION D,H                                             XRAY.459
C                                                                      XRAY.460
   10 CONTINUE                                                         XRAY.461
      SWPR=.FALSE.                                                     XRAY.462
      TEST=0.0                                                         XRAY.463
      H=HPR/DBLE(FLOAT(IP*24))                                         XRAY.464
      IF ((NPKS.LT.3).OR.(.NOT.SWAM)) GO TO 40                         XRAY.465
C                                                                      XRAY.466
C--ADAMS-MOULTON STEP.                                                 XRAY.467
C                                                                      XRAY.468
      DO 20 I=1,N                                                      XRAY.469
      D=DBLE(F(I))                                                     XRAY.470
      T(4,I)=D                                                         XRAY.471
      Y(I)=SNGL(T(5,I)+H*(55.0D0*D-59.0D0*T(3,I)+37.0D0*T(2,I)-9.0D0*T(1XRAY.472
     1,I)))                                                            XRAY.473
   20 CONTINUE                                                         XRAY.474
      X=SNGL(XX+24.0D0*H)                                              XRAY.475
                                                                       XRAY.476
      CALL DERIVE                                                      XRAY.477
      IF(KOUT .LT. 0) RETURN                                           XRAY.478
                                                                       XRAY.479
      DO 30 I=1,N                                                      XRAY.480
      D=DBLE(F(I))                                                     XRAY.481
      D=(T(5,I)+H*(9.0D0*D+19.0D0*T(4,I)-5.0D0*T(3,I)+T(2,I)))         XRAY.482
      T(6,I)=D                                                         XRAY.483
      E=ABS(SNGL(D)-Y(I))/14.0                                         XRAY.484
      TEST=AMAX1(E/AMAX1(AREF,ABS(SNGL(D))),TEST)                      XRAY.485
   30 CONTINUE                                                         XRAY.486
      GO TO 100                                                        XRAY.487
C                                                                      XRAY.488
C--ZONNEVELD STEP.                                                     XRAY.489
C                                                                      XRAY.490
   40 CONTINUE                                                         XRAY.491
      DO 50 I=1,N                                                      XRAY.492
      D=DBLE(F(I))                                                     XRAY.493
      T(4,I)=D                                                         XRAY.494
C -- 1                                                                 XRAY.495
      Y(I)=SNGL(T(5,I)+H*(12.0D0*D))                                   XRAY.496
   50 CONTINUE                                                         XRAY.497
      X=SNGL(XX+12.0D0*H)                                              XRAY.498
                                                                       XRAY.499
      CALL DERIVE                                                      XRAY.500
      IF(KOUT .LT. 0) RETURN                                           XRAY.501
                                                                       XRAY.502
      DO 60 I=1,N                                                      XRAY.503
      D=DBLE(F(I))                                                     XRAY.504
```

```
[illegible]                              FTN 4.6+439/0-0     26 FEB 77 08.36.54S BKY PAGE      1

      SUBROUTINE LSM(IPO,X,HP,Q)                                        XRAY.417
                                                                        XRAY.418
      COMMON  /  [illegible]  /  Y(4),F(4),T(8,4)                       XRAY.419
      COMMON /INTL/ ITMX,AREF,CMAX,SSSR,HFAC,SWAM,SWEX                  XRAY.420
      COMMON /INTP/ [illegible],XX,N,[illegible],IP,IT,NFKS,SWIN        XRAY.421
                                                                        XRAY.422
      LOGICAL SWAM,SWEX,SWIN                                            XRAY.423
      INTEGER HFAC                                                      XRAY.424
      DOUBLE PRECISION [illegible],HPP,XX                               XRAY.425
      DATA ITMX , AREF , CMAX , SSSR , HFAC , SWAM , SWEX   /           XRAY.426
     +      1 24 , 1.0 ,1.0E-5, 100.0,  2   ,.TRUE.,.TRUE.   /          XRAY.427
                                                                        XRAY.428
C                                                                       XRAY.429
      [illegible]                                                       XRAY.430
      [illegible](X)                                                    XRAY.431
      [illegible]                                                       XRAY.432
      [illegible]                                                       XRAY.433
      [illegible]/SSSR                                                  XRAY.434
      IP=1                                                              XRAY.435
      IT=0                                                              XRAY.436
      NFKS=0                                                            XRAY.437
      SWIN=SWEX                                                         XRAY.438
                                                                        XRAY.439
      CALL [illegible]IN                                                XRAY.440
                                                                        XRAY.441
      DO 10 I=1,N                                                       XRAY.442
      T(5,I)=[illegible](Y(I))                                          XRAY.443
   10 CONTINUE                                                          XRAY.444
                                                                        XRAY.445
      RETURN                                                            XRAY.446
      END                                                               XRAY.447
```

```
      SUBROUTINE ZAM(X,SWPR)                                            XRAY.448
                                                                        XRAY.449
      COMMON  /  FIELD  /  Y(4),F(4),T(8,4)                             XRAY.450
      COMMON  /  UNITS  /  KOUT                                         XRAY.451
      COMMON /INTC/ TPMX,AREF,EMAX,SSSR,HFAC,SWAM,SWEX                  XRAY.452
      COMMON /INTP/ HPP,XX,N,ELB,SLB,IP,IT,NPKS,SWIN                    XRAY.453
                                                                        XRAY.454
      LOGICAL  SWAM,SWEX,SWIN                                           XRAY.455
      LOGICAL SWPR                                                      XRAY.456
      INTEGER HFAC                                                      XRAY.457
      DOUBLE PRECISION T,HPP,XX                                         XRAY.458
      DOUBLE PRECISION D,H                                              XRAY.459
C                                                                       XRAY.460
   10 CONTINUE                                                          XRAY.461
      SWPR=.FALSE.                                                      XRAY.462
      TEST=0.                                                           XRAY.463
      H=HPP/DBLE(FLOAT(IP*24))                                          XRAY.464
      IF ((NPKS.LT.2).OR.(.NOT.SWAM)) GO TO 40                          XRAY.465
C                                                                       XRAY.466
C--- ADAMS-MOULTON STEP.                                                XRAY.467
C                                                                       XRAY.468
      DO 20 I=1,N                                                       XRAY.469
      D=DBLE(F(I))                                                      XRAY.470
      T(4,I)=D                                                          XRAY.471
      Y(I)=SNGL(T(5,I)+H*(55.0D0*D-59.0D0*T(3,I)+37.0D0*T(2,I)-9.0D0*T(1XRAY.472
     1,I)))                                                             XRAY.473
   20 CONTINUE                                                          XRAY.474
      X=SNGL(XX+24.D0*H)                                                XRAY.475
                                                                        XRAY.476
      CALL DERIVE                                                       XRAY.477
      IF(KOUT .LT. 0) RETURN                                            XRAY.478
                                                                        XRAY.479
      DO 30 I=1,N                                                       XRAY.480
      D=DBLE(F(I))                                                      XRAY.481
      D=T(5,I)+H*(9.0D0*D+19.0D0*T(4,I)-5.0D0*T(3,I)+T(2,I)))           XRAY.482
      T(6,I)=D                                                          XRAY.483
      E=ABS(SNGL(D)-Y(I))/14.                                           XRAY.484
      TEST=AMAX1(E/AMAX1(AREF,ABS(SNGL(D))),TEST)                       XRAY.485
   30 CONTINUE                                                          XRAY.486
      GO TO 100                                                         XRAY.487
C                                                                       XRAY.488
C--[illegible] STEP.                                                    XRAY.489
C                                                                       XRAY.490
   40 CONTINUE                                                          XRAY.491
      DO 50 I=1,N                                                       XRAY.492
      D=DBLE(F(I))                                                      XRAY.493
      T(4,I)=D                                                          XRAY.494
C -- 1                                                                  XRAY.495
      Y(I)=SNGL(T(5,I)+H*(12.0D0*D))                                    XRAY.496
   50 CONTINUE                                                          XRAY.497
      X=SNGL(XX+12.D0*H)                                                XRAY.498
                                                                        XRAY.499
      CALL DERIVE                                                       XRAY.500
      IF(KOUT .LT. 0) RETURN                                            XRAY.501
                                                                        XRAY.502
      DO 60 I=1,N                                                       XRAY.503
      D=DBLE(F(I))                                                      XRAY.504
```

```
            T(5,I)=D                                                        XRAY.505
      C -- 2                                                                XRAY.506
            Y(I)=SNGL(T(5,I)+H*(12.0D0*D))                                  XRAY.507
         60 CONTINUE                                                        XRAY.508
                                                                            XRAY.509
            CALL DERIVE                                                     XRAY.510
            IF(KOUT .LT. 0) RETURN                                          XRAY.511
                                                                            XRAY.512
            DO 70 I=1,N                                                     XRAY.513
            D=DBLE(F(I))                                                    XRAY.514
            T(7,I)=D                                                        XRAY.515
      C -- 3                                                                XRAY.516
            Y(I)=SNGL(T(5,I)+H*(24.0D0*D))                                  XRAY.517
         70 CONTINUE                                                        XRAY.518
            X=SNGL(XX+24.D0*H)                                              XRAY.519
                                                                            XRAY.520
            CALL DERIVE                                                     XRAY.521
            IF(KOUT .LT. 0) RETURN                                          XRAY.522
                                                                            XRAY.523
            DO 80 I=1,N                                                     XRAY.524
            D=DBLE(F(I))                                                    XRAY.525
            T(8,I)=D                                                        XRAY.526
      C -- 4                                                                XRAY.527
            Y(I)=SNGL(T(5,I)+H*(3.75D0*T(4,I)+5.25D0*T(6,I)-9.75D0*T(7,I)-0.75XRAY.528
           1D0*D))                                                          XRAY.529
         80 CONTINUE                                                        XRAY.530
            X=SNGL(XX+18.D0*H)                                              XRAY.531
                                                                            XRAY.532
            CALL DERIVE                                                     XRAY.533
            IF(KOUT .LT. 0) RETURN                                          XRAY.534
                                                                            XRAY.535
            DO 90 I=1,N                                                     XRAY.536
            D=DBLE(F(I))                                                    XRAY.537
            D=ABS(SNGL(H*(-16.0D0*T(4,I)+48.0D0*T(6,I)+48.0D0*T(7,I)+48.0D0*T(XRAY.538
           18,I)-128.0D0*D)))                                               XRAY.539
      C -- 5                                                                XRAY.540
            D=T(5,I)+H*(4.0D0*T(4,I)+8.0D0*T(6,I)+8.0D0*T(7,I)+4.0D0*T(8,I))XRAY.541
            T(5,I)=D                                                        XRAY.542
            TEST=AMAX1(AMAX1(ABCF,ABS(SNGL(D))),TEST)                       XRAY.543
         90 CONTINUE                                                        XRAY.544
      C                                                                     XRAY.545
      C--BOTH ADAMS-MOULTON AND ZONNEVELD METHODS CONTINUE FROM HERE.       XRAY.546
      C                                                                     XRAY.547
        100 CONTINUE                                                        XRAY.548
            X=SNGL(XX+24.D0*H)                                              XRAY.549
            IF (TEST.LE.SUB) GO TO 120                                      XRAY.550
            IF (IPAWFAC.GT.IPMX) GO TO 120                                  XRAY.551
      C                                                                     XRAY.552
      C--REPEAT STEP WITH SMALLER H.                                        XRAY.553
      C                                                                     XRAY.554
            H=H*S,                                                          XRAY.555
            IP=IP*FAC                                                       XRAY.556
            IT=IT*FAC                                                       XRAY.557
            DO 110 I=1,N                                                    XRAY.558
            Y(I)=SNGL(T(5,I))                                               XRAY.559
            F(I)=SNGL(T(4,I))                                               XRAY.560
        110 CONTINUE                                                        XRAY.561
```

```
SUBROUTINE SKIPFIL   7600*7600 OPT=1                    FTN 4.6+439/040    28 FEB 77 08.36.54$ BKY PAGE      1

                  SUBROUTINE SKIPFIL(JOF,N)                                            XRAY.725
            C                                                                          XRAY.726
                  DO 17 I=1,N                                                          XRAY.727
               11 BUFFER IN(JOF,1)(JUNK,JUNK)                                          XRAY.728
                  IF(UNIT(JOF))11,17,11                                                XRAY.729
               17 CONTINUE                                                             XRAY.730
                  RETURN                                                               XRAY.731
            C                                                                          XRAY.732
                  ENTRY SKIPREC                                                        XRAY.733
                  DO 27 I=1,N                                                          XRAY.734
                  BUFFER IN(JOF,1)(JUNK,JUNK)                                          XRAY.735
                  IF(UNIT(JOF))29,29,27                                                XRAY.736
               27 CONTINUE                                                             XRAY.737
               29 RETURN                                                               XRAY.738
                  END                                                                  XRAY.739


SUBROUTINE ZAM       7600*7600 OPT=1                    FTN 4.6+439/040    28 FEB 77 08.36.54$ BKY PAGE      4

                 RETURN                                                                XRAY.619
           C                                                                           XRAY.620
             170 FORMAT (50H0 CANNOT DECREASE H BECAUSE OF HMIN,,1PE16.8,I20)          XRAY.621
                                                                                       XRAY.622
                 END                                                                   XRAY.623
```

```
      [illegible]                                                       XRAY.624
                                                                        XRAY.625
      [illegible]YZ,YL,RAD,RO,RD                                        XRAY.626
      [illegible]                                                       XRAY.627
      [illegible](I),Y(I)                                               XRAY.628
      [illegible]XMAX,YMIN,YMAX,ICXMIN,ICXMAX,ICYMIN,ICYMAX,INC         XRAY.629
      [illegible](I),RAD,RO,R)                                          XRAY.630
                                                                        XRAY.631
      [illegible]                                                       XRAY.632
      [illegible]                                                       XRAY.633
      [illegible]                                                       XRAY.634
      [illegible]                                                       XRAY.635
      [illegible]                                                       XRAY.636
      [illegible]                                                       XRAY.637
      [illegible]                                                       XRAY.638
      [illegible]                                                       XRAY.639
      [illegible]                                                       XRAY.640
      [illegible]                                                       XRAY.641
      [illegible]                                                       XRAY.642
      [illegible]                                                       XRAY.643
      [illegible]                                                       XRAY.644
      [illegible]                                                       XRAY.645
      [illegible](X(I)-XMAX)                                            XRAY.646
      [illegible]                                                       XRAY.647
      [illegible](Y(I)-YMAX)                                            XRAY.648
      [illegible](YTT.GT.0.0)) GO TO 9                                  XRAY.649
      [illegible].AND.(ABT.RET)) GO TO 30                               XRAY.650
      [illegible]CXMIN                                                  XRAY.651
      [illegible]CYMIN                                                  XRAY.652
      [illegible]                                                       XRAY.653
      [illegible]                                                       XRAY.654
      [illegible]                                                       XRAY.655
      [illegible]                                                       XRAY.656
      [illegible]                                                       XRAY.657
      [illegible]                                                       XRAY.658
      [illegible]                                                       XRAY.659
      [illegible]                                                       XRAY.660
      [illegible]                                                       XRAY.661
      [illegible] GO TO 7                                               XRAY.662
      [illegible]                                                       XRAY.663
      [illegible]                                                       XRAY.664
      GO TO 1                                                           XRAY.665
    7 IF([illegible].NE.(I-INC)) GO TO 9                                XRAY.666
      [illegible]                                                       XRAY.667
      GO TO 1                                                           XRAY.668
    9 [illegible]                                                       XRAY.669
      [illegible]                                                       XRAY.670
      IF((XTL[illegible]0.0).AND.(YTL.LE.0.0)) GO TO 1                  XRAY.671
      IF((XTL[illegible]0.0).AND.(YTL.EQ.0.0)) GO TO 1                  XRAY.672
      [illegible]                                                       XRAY.673
   1  DX=X(LAST+ADD)-X(K)                                               XRAY.674
      DY=Y(LAST+ADD)-Y(K)                                               XRAY.675
      A=ATAN2(DY,DX)                                                    XRAY.676
      XI=XMIN-X(K)                                                      XRAY.677
      YI=YMIN-Y(K)                                                      XRAY.678
      [illegible](1,N1)                                                 XRAY.679
      IF((1-A))4,25,13                                                  XRAY.680
```

```
15 Y[illegible]=[illegible]YMIN                                         XRAY.681
   [illegible]=[illegible]Y/[illegible])*K1                             XRAY.682
   [illegible]                                                          XRAY.683
16 [illegible]=[illegible](K)                                           XRAY.684
   [illegible](Y1,X2)                                                   XRAY.685
   IF([illegible])1[illegible],2[illegible],15                          XRAY.686
1[illegible] [illegible]YMIN                                            XRAY.687
   X[illegible]=[illegible]Y)*K1                                        XRAY.688
   [illegible] 21                                                       XRAY.689
16 Y[illegible]=[illegible]X-Y(K)                                       XRAY.690
   [illegible](YL,X2)                                                   XRAY.691
   IF([illegible])1[illegible],27,17                                    XRAY.692
17 XP=[illegible]XMAX                                                   XRAY.693
   [illegible]=([illegible])*K2                                         XRAY.694
   [illegible]                                                          XRAY.695
1[illegible] [illegible](Y2,Y1)                                         XRAY.696
   [illegible])13,2[illegible],19                                       XRAY.697
1[illegible] YP=[illegible]                                             XRAY.698
   [illegible]([illegible]/[illegible])*Y1                              XRAY.699
1  XP=((XP-X1)/XD)*CCXD+CCXMIN                                          XRAY.700
   [illegible] 2[illegible]                                             XRAY.701
2[illegible] YP=((YP-Y1)/YD)*CCYD+CCYMIN                                XRAY.702
2[illegible] [illegible] LASTB[illegible]=-INC                          XRAY.703
   [illegible] 4                                                        XRAY.704
[illegible]                                                             XRAY.705
[illegible]                                                             XRAY.706
[illegible]                                                             XRAY.707
[illegible]                                                             XRAY.708
[illegible]                                                             XRAY.709
[illegible]                                                             XRAY.710
[illegible]                                                             XRAY.711
[illegible]                                                             XRAY.712
[illegible]                                                             XRAY.713
[illegible]                                                             XRAY.714
[illegible]                                                             XRAY.715
[illegible]                                                             XRAY.716
[illegible]                                                             XRAY.717
   IF([illegible]).[illegible].(YPT.LE.0.0)) GO TO 3                    XRAY.718
   [illegible].[illegible].(YPT.EQ.0.0)) GO TO 3                        XRAY.719
   [illegible]                                                          XRAY.720
   [illegible]                                                          XRAY.721
   [illegible] 10                                                       XRAY.722
   [illegible]                                                          XRAY.723
                                                                        XRAY.724
```